NTNU – Trondheim
Norwegian University of
Science and Technology

Friction Models for Oscillating Flow in a U-tube

Bjørn Olav Thon

Master of Science in Physics and Mathematics
Submission date: Januar 2014
Supervisor: Jon Andreas Støvneng, IFY
Co-supervisor: Ole Jørgen Nydal, Institutt for energi - og prosessteknikk

Norwegian University of Science and Technology
Department of Physics

Acknowledgements

I would like to thank my supervisor at the Department of Energy and Process Engineering, Ole-Jørgen Nydal, for giving me the opportunity to work with this project. His guidance and advice has been of great help during the work on this thesis.

Furthermore, I would also like to thank my supervisor at the Department of Physics, Jon Andreas Støvneng, for his advice and guidance while writing the report.

Summary

The basic theory of friction in pipe flow was reviewed in the first part of this thesis. Using the results from this review, steady friction relations were derived for laminar and turbulent pipe flow.

Steady turbulent friction relations were tested in 1D simulations of oscillating flow in a U-tube with a constant inner diameter. The results show that steady friction relations do not provide sufficient damping compared to experimental data. In order to improve the simulation results, systematic tests of some common unsteady friction relations were conducted.

The concluding solution to the friction issue is a combination of laminar and turbulent friction relations, with an unsteady correction. The new friction relation was tested in 1D simulations of oscillating flow in a U-tube with a constant inner diameter. Results show that there is very good accordance between simulations and experimental data. The computational results were validated by experimental data from flow cases of varying Reynolds numbers and three different liquids.

In the second part of this thesis, experimental work was conducted on a U-tube with an inner diameter change at the bottom of the bend. The damping of the oscillations was observed to be much greater than in the U-tube with a constant inner diameter.

A computer program for image analysis was developed to allow for continuous measurements of the liquid interface level in the U-tube experiments. The program returned satisfying results, both with respect to accuracy and reliability. However, it was concluded that the results from the program could have been better if the U-tube had been made from another material.

Simulations of oscillating flow in the U-tube with an inner diameter change were done in order to further investigate the new unsteady friction relation. Comparisons of simulated and experimental results indicated that the friction loss in the diameter change coupling caused inaccuracies in the simulations.

Sammendrag

I den første delen av denne oppgaven har den grunnleggende teorien for friksjon i rørstrømning blitt gjennomgått. Ut fra dette har tidsuavhengige friksjonsrelasjoner for laminær og turbulent rørstrømning blitt utledet.

Friksjonsrelasjoner for tidsuavhengig turbulens har blitt testet i 1D-simuleringer av væskeoscillasjoner i et U-rør med konstant indre diameter. Resultatene viser at disse friksjonsrelasjonene ikke gir god nok dempning av oscillasjonene. For å forbedre resultatene av simuleringene, har derfor noen av de vanligste tidsavhengige friksjonsrelasjonene blitt systematisk testet.

Den konkluderende løsningen i denne oppgaven er en kombinasjon av laminær og turbulent friksjon, med en tidsavhengig korreksjon. Den nye friksjonsrelasjonen har blitt testet i 1D-simuleringer av væskeoscillasjoner i et U-rør med konstant indre diameter. Resultatene viser at det er veldig god overensstemmelse mellom simuleringer og eksperimentelle data. Experimentelle data fra forsøk med tre forskjellige væsker og varierende Reynolds-nummer har blitt brukt til å validere simuleringsresultatene.

I den andre delen av denne oppgaven har det blitt utført eksperimentelt arbeid på et U-rør med en endring av den indre diameteren. Det ble observert at dempningen av oscillasjonene var mye større enn i U-røret med konstant indre diameter.

Et bildeanalyseringsprogram har blitt utviklet for å kunne utføre kontinuerlige målinger av nivået til væskeoverflaten i U-rør-eksperimenter. Programmet ga tilfredsstillende resultater, både med tanke på nøyaktighet og pålitelighet. Det har imidlertid blitt konkludert med at resultatene kunne vært enda bedre hvis U-røret hadde vært laget av et annet materiale.

Det har også blitt utført simuleringer av væskeoscillasjoner i U-røret med en endring i indre diameter. Dette var for å videre undersøke effekten av den nye friksjonsrelasjonen fra første del av oppgaven. Sammenlikninger av resultater fra simuleringer og eksperimenter indikerer at simuleringene blir unøyaktige på grunn av friksjonstapet i overgangen mellom de to rørdiameterne.

Preface

This report concludes my Master studies of Applied Physics at the Norwegian University of Science and Technology (NTNU). Being a physics student, I have had the opportunity to work with many subjects. I became interested in programming and fluid dynamics early in my studies. This thesis was therefore a good opportunity for combining two of my favorite subjects.

Although I mainly wanted a theoretical and computational thesis, I was delighted when I got the chance to do experimental work in the Multiphase Flow Laboratory in the Department of Energy and Process Engineering at NTNU. This brought first-hand insight to the computational work that I had previously done.

This thesis is not a continuation of my specialization project. It therefore demanded a lot of work in the fall of 2013, but I am pleased with the result. The thought that I was doing something useful was driving me in the most laborious times. I hope that some of the work from this thesis will be of use in U-tube simulations in the future.

I would finally like to thank the people, other than my supervisors, who have helped me with this thesis. The lab technicians at the Multiphase Flow Laboratory did a fantastic job. Furthermore, I am really grateful for the effort that was put into proofreading by my girlfriend and closest friends.

Declaration

I hereby declare that this work has been performed independently and in accordance with the rules and regulations at the Norwegian University of Science and Technology (NTNU).

Trondheim, January 2014

Bjørn Olav Thon

Table of Contents

List of Tables

List of Figures

1 Introduction

Oscillatory flow in U-shaped pipe systems can be found in several areas of the industry. These flow phenomena usually occur in large pipe systems and can potentially cause damage to equipment and installations. Computer simulations can contribute to predict oscillatory flows in various systems so that unwanted scenarios can be avoided. Hence, good computer models are needed for these kinds of flow scenarios. The main part of the work in this thesis has therefore been devoted to the study of friction relations that can make computer simulations more accurate.

One scenario involving oscillatory flow in pipe systems is when an oil pipeline is shut down for maintenance purposes. The liquid will accumulate in the lower bends of the pipeline and oscillate due to force imbalance. Another scenario from the oil and gas industry is oscillations of fluids between the drill string and the annulus in an oil well [1]. Due to pressure fluctuations, the liquid in the system can start to oscillate. This can cause delays in the production and in the worst case cause damage to equipment.

A third scenario can be found in hydroelectric power plants. If the flow of water towards the turbines is to be stopped, one cannot simply close a valve. The immense inertial forces of the moving water will then cause a water hammer incident [2, 3]. Instead, the water is lead into an inclined relief shaft, making a U-tube system with the main shaft.

By the help of accurate computer simulations, the conditions that cause the above scenarios can be identified and avoided. Moreover, it is of interest to the operators of the pipe systems to know when the oscillations will stop, so that they can deploy the necessary tools into the pipelines as fast as possible. Unnecessary ”down time” can thus be minimized.

Commercial flow simulators such as OLGA and LedaFlow could be used to perform the simulations in oil and gas pipe lines. However, these programs are not very well suited for accurate front tracking simulations. Because the pipe is divided into a finite number of grid blocks, the results will be influenced by a certain amount of numerical diffusion. Hence, the results of the simulations will not be as accurate as in a program that is tracking the front of the liquid column.

Earlier studies of flow in a U-tube with a constant inner diameter have indicated that the results from simple 1D front tracking schemes with steady turbulent friction relations do not match experimental results. The discrepancies mainly occurred because the simulated oscillations never came to a complete stop. Simulations of OLGA and LedaFlow will come to rest, but this is due to the numerical diffusion[1].

The friction relation resulting from the present work should therefore be able to make simulations match available experimental data. The simulations should also come to rest at about the same time as observed in experiments. Furthermore, it is desirable that the resulting expression could be implemented into a larger flow simulation program without interfering with established friction relations.

Experimental work was done on a U-tube with an inner diameter change. This is a system that resembles that of a small diameter drill string and a large diameter annulus in an oil well. Accurate simulations of U-tube oscillations in a diameter change system could therefore contribute to increased safety during drilling operations. Whether or not the new friction relation could be a contributing factor in such simulations is therefore a question of interest in the present work.

[1] Information on OLGA and LedaFlow was acquired during discussions with supervisor Ole-Jørgen Nydal.

2 Theory

A brief overview of general pipe friction is given in the beginning of this section. Steady pipe friction relations for both laminar and turbulent flow are then derived. A selection of different pipe friction models are presented and discussed in the light of their relevance to oscillating flow in a U-tube of constant inner diameter. Both steady and unsteady friction relations have been considered. The concluding friction relation from the U-tube friction study is then presented. The equation of motion for flow in a U-tube is derived in the last part of this theory section. The U-tube with a constant inner diameter will be considered first. Then the U-tube with an inner diameter change is discussed. The numerical implementation of the equations of motion will then be described.

2.1 Steady Pipe Friction

Inaccurate wall friction formulations are believed to be the reason for the unsatisfactory simulation results in U-tubes. Understanding the basic concept of wall friction is therefore important when looking for solutions to this problem. The type of friction relation that should be used depends on the flowing regime (laminar or turbulent) and whether the flow is steady (independent of time) or unsteady (time dependent). A general description of what we associate with steady pipe friction will now be given, followed by a derivation of the steady laminar friction coefficient. Then we look at how steady turbulent friction coefficients can be derived from the shear stress and velocity profiles.

Fluid flow is considered steady whenever the flow does not change in time at every inner of the system. The time derivatives of the flow field thus have to be zero [4]. In the case of oscillating flow in a U-tube, the flow changes direction periodically, which means that the flow continuously changes in time. Hence, we have an unsteady, or transient, flow in our U-tube system. For this reason, steady friction relations are strictly speaking not valid.

However, steady friction models have historically often been sufficient to represent wall friction in unsteady flows. Even though the models do not meet all the criteria of the flow in question, certain assumptions have historically been used. For instance, the flow resistance in unsteady flow can be assumed to be equal to the resistance that would exist in steady flow with the same mean velocity [5]. This has proven to be valid in many pipe flow cases, which is why steady friction relations are so widely used. Looking at some of the steady turbulent friction models will therefore be a good place to start this computational investigation of friction relations.

For the present study, only 1D flows will be considered. The assumption that fluid flow in pipes is essentially 1D is very commonly used among those who are modeling transient phenomena. It is an assumption made in almost all commercial steady pipe flow models as well. When assuming a 1D steady flow, friction loss, changes in momentum and energy relations are assumed to be directly related to the mean velocity [6].

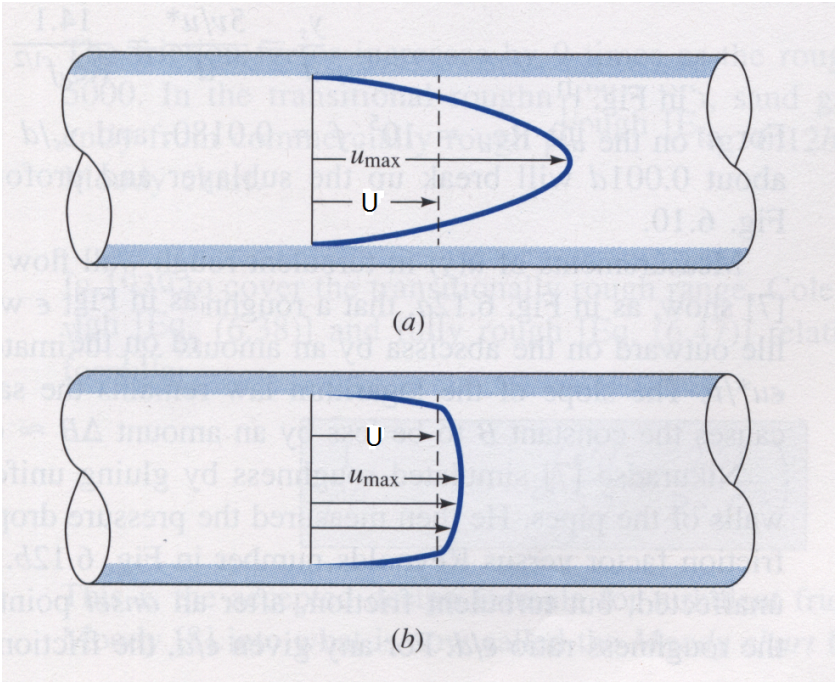

Figure 2.1: A figure showing examples of velocity profiles of a) laminar flow and b) turbulent flow in a pipe. U denotes the mean velocity of the two profiles. u_{max} is the maximum velocity, which occurs at the center of the pipe in both figures. The figure is from [7] and has been slightly modified.

2.1.1 Shear Stress in Laminar and Turbulent Flows

The shear stress is the force that slows down the flow in a pipe, whether it is laminar, turbulent, steady or unsteady. Hence, this is a natural place to start the study of pipe flow friction.

Friction forces in pipe flows are caused by shear stresses. The shear is caused by two different mechanisms; viscosity and turbulent eddy structures. Viscous forces occur between the liquid and the pipe wall, but also internally between liquid molecules. Friction forces due to eddy structures occur in turbulent flows. Because the structure of laminar and turbulent flows is very different, the shear stresses are also different. They are expressed in the following way:

$$\begin{aligned} &\text{Laminar:} && \tau = \mu \frac{\partial U}{\partial y} && 0 < y < R \\ &\text{Turbulent:} && \tau = \mu \frac{\partial U}{\partial y} - \rho \overline{u'v'} && 0 < y < \delta \end{aligned} \tag{2.1}$$

where μ is the dynamic viscosity, U is the mean velocity and ρ is the fluid density. u' and v' denote the fluctuations from the mean values of the velocity components in the x-and y-direction, respectively. It is important to notice the difference in the validity ranges of the two shear stress expressions in equation (2.1). The laminar shear decay holds all the way to the center of the pipe. In turbulent flow, a thin turbulent boundary layer will be formed closest to the wall. The turbulent shear stress is non-zero only within the turbulent boundary layer. δ is thus defined as the distance from the wall where the velocity has essentially reached its free stream value. Though not very accurate, the thickness of the turbulent boundary layer is often given as [8]:

$$\delta(x) \approx \frac{0.37\nu x^{4/5}}{U} \tag{2.2}$$

where x is the downstream distance from the beginning of the turbulent boundary layer. To get an impression of how thin this layer is, we can calculate δ with $x = 1m$ for water flowing in a pipe with $U = 5m/s$. These are typical parameter values in the simulations that will be presented later. The result is $\delta = 7.4 \cdot 10^{-5}mm$, which is vanishingly small.

Starting by considering the laminar shear stress in equation (2.1), we see that it only depends on the transverse gradient of the mean velocity and the kinetic viscosity. It has its largest value at the wall, where we have no-slip. It is exerted directly to the wall and is due to viscous forces. Because of the friction between the liquid molecules, the stress drag propagates from the wall and towards the center of the pipe [7]. This results in a shear stress profile, $\tau(r)$, which has a maximum at the pipe wall and a minimum in the pipe center. The center of the pipe thus becomes the point of the least flow resistance. That explains why we have the greatest velocity at the center of the pipe in laminar flow. The velocity profile is shown in Figure 2.1.

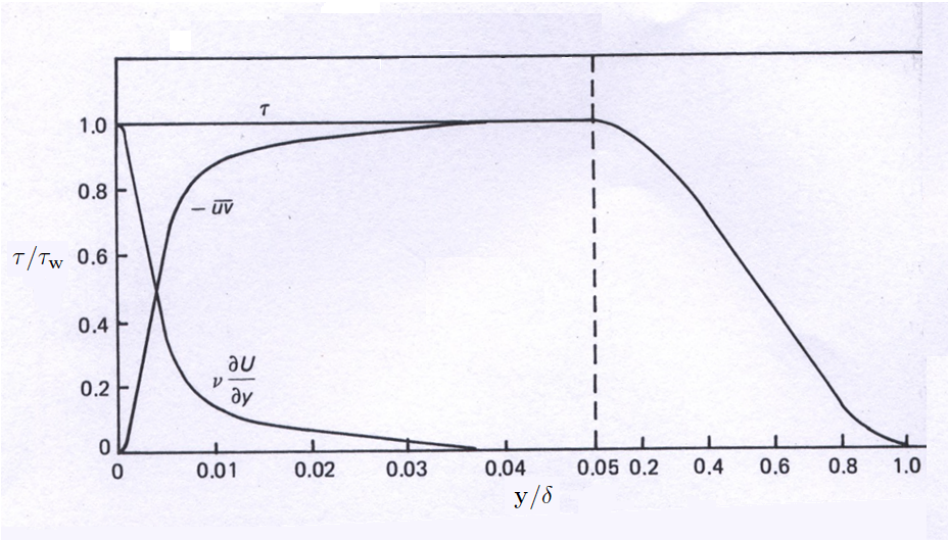

Figure 2.2: A figure illustrating the contributions from viscous stresses and Reynolds stresses to the total turbulent shear stress in equation (2.1). Note that the illustration is valid for uniform free stream flow. δ denotes the thickness of the boundary layer and the turbulent shear stress is in essence zero outside this layer. The figure is from [9] and has been slightly modified.

As for the turbulent shear stress in equation (2.1), we see that there are two contributions. The first term has the same form as for laminar flow. It is there because of the fact that there will always be a thin laminar sub layer in turbulent flows. Hence, there is no such thing as completely turbulent flows [4]. As in laminar flow, the laminar shear term has a maximum at the wall and is small away from the wall.

The other term in the turbulent shear stress is zero at the wall (due to the no-slip condition), but large away from the wall, see Figure 2.2. It is caused by turbulent eddy structures and is often referred to as the Reynolds stress. The Reynolds stress is proportional to the time average of the velocity fluctuations u' and v' [9]. As we understand from the example calculation above, the turbulent boundary layer is very thin. For uniform free stream flow, Figure 2.2 shows that the total turbulent shear stress is zero outside the turbulent boundary layer. This is the reason why the turbulent velocity profile in Figure 2.1 is so much flatter than the laminar velocity profile. For $0 < r < R - \delta$, there is no shear stress affecting the flow.

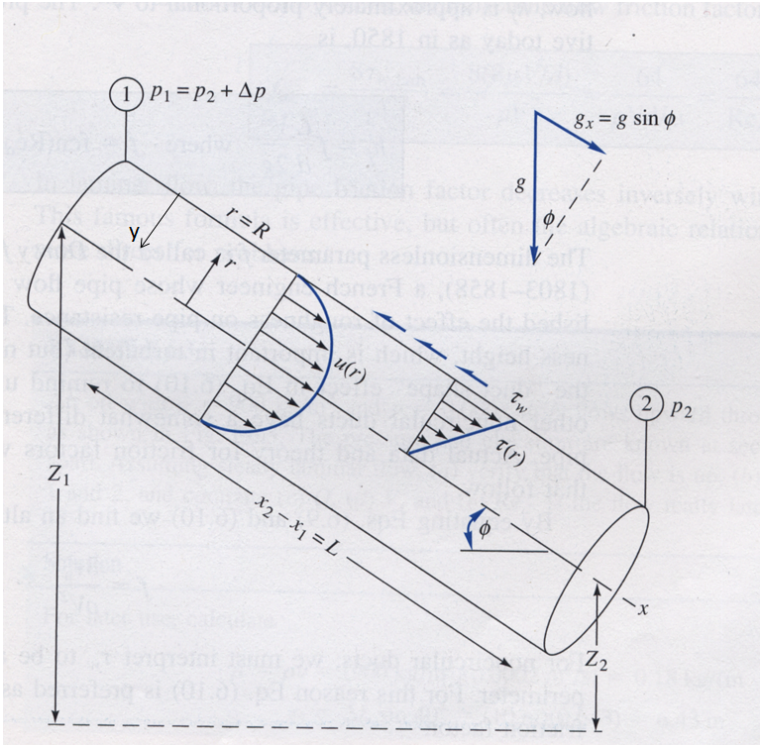

Figure 2.3: A figure illustrating steady laminar flow in a declined pipe. Δp is pressure loss due to friction, while ϕ is the declination angle with the horizontal plane. The laminar shear stress profile from equation (2.1) is denoted by $\tau(r)$. Note that y is defined in the opposite direction of r, as illustrated in the figure. The figure is from [7] and has been slightly modified.

2.1.2 The Darcy-Weisbach Friction Coefficient

In this section we look at how the shear stress can be expressed more qualitatively by the Darcy-Weisbach friction coefficient. This coefficient will prove very convenient in the work to come.

Pressure loss due to friction is often quantified by the head loss, h_f. The head loss in pipes equals the change in the sum of the pressure and gravity head over a certain distance. To show this, we first look at the energy equation at two different cross-sections of steady flow in the declined pipe in Figure 2.3:

$$\left(\frac{p}{\rho g} + \frac{U^2}{2g} + z\right)_1 = \left(\frac{p}{\rho g} + \frac{U^2}{2g} + z\right)_2 + h_f \tag{2.3}$$

where U is the mean velocity and z is the height relative to a reference point.

Because the flow is steady, the velocity does not change between the two cross-sections. The velocity terms cancel, and the head loss becomes:

$$h_f = (z_1 - z_2) + \left(\frac{p_1}{\rho g} - \frac{p_2}{\rho g}\right) = \Delta z + \frac{\Delta p}{\rho g} \tag{2.4}$$

Considering the force balance in the flow direction over the same segment of the pipe, we get:

$$\sum F_x = \Delta p(\pi R^2) + \rho g(\pi R^2)\Delta z - \tau_w(2\pi R)\Delta x = 0 \tag{2.5}$$

where the first term is the pressure force, the second is a gravitational force due to the height difference $\Delta z = (z_1 - z_2)$, and the last term is the friction term. We see that the wall shear stress, which is equation (2.1) evaluated at the wall, enters the force balance. We can now divide equation (2.5) by $\rho g(\pi R^2)$ and solve for the head loss. Hence, the head loss over a segment Δx of the pipe can be expressed through the wall shear stress:

$$\Delta z + \frac{\Delta p}{\rho g} = h_f = \frac{4\tau_w}{\rho g}\frac{\Delta x}{D} \tag{2.6}$$

In the middle of the 19th century, there were several experimentalists who discovered that the head loss over a distance Δx had a direct dependence on the velocity head ($U^2/2g$), while varying inversely with the pipe diameter (D). Among these were Weisbach and Darcy, who proposed an empirical relation for the head loss in a pipe [7]:

$$h_f = \lambda\frac{\Delta x}{D}\frac{U^2}{2g} \tag{2.7}$$

where λ is referred to as the Darcy-Weisbach friction factor and U is the mean velocity. Later, Darcy experimentally established the effect of pipe material roughness (ϵ) for the friction coefficient: $\lambda = f(Re, \epsilon)$ [7].

Multiplying equation (2.7) by ρg, we get an equation for the pressure loss in a pipe due to wall friction over a distance Δx:

$$\Delta p = \lambda\frac{\Delta x \rho U^2}{2D} \tag{2.8}$$

Finally, we can eliminate h_f between equations (2.6) and (2.7) to find a relationship between the wall shear stress and the Darcy-Weisbach friction coefficient:

$$\tau_w = \lambda \frac{\rho U^2}{8} \tag{2.9}$$

Once λ is specified in equation (2.9), the friction caused by the wall is known. Hence, finding an accurate expression for λ is of great importance, and has been the subject of much research. Some of the results of this research will be displayed and discussed in the sections to come. There are many ways of determining the friction coefficient for turbulent flows. In laminar flow, on the other hand, λ can be determined exactly from the Navier-Stokes equation.

2.1.3 The Reynolds Number

At this point, it is convenient to establish the definition of the Reynolds number for pipe flow. The Reynolds number expresses the ratio between inertial forces and viscous forces. In pipe flow it is usually expressed in the following ways [7]:

$$Re = \frac{\rho D|U|}{\mu} \tag{2.10}$$

or:

$$= \frac{D|U|}{\nu} \tag{2.11}$$

where ρ is the density of the liquid, U is the mean velocity of the liquid column, D is the diameter of the pipe, μ is the dynamic viscosity and $\nu \equiv \mu/\rho$ is the kinematic viscosity. Though they vary somewhat with parameters such as flow geometry and surface roughness, there are generally accepted Reynolds number limits for different flow regimes. For pipe flow, these limits are [7]:

$$\begin{aligned} &\text{Laminar:} && Re \leq 2300 \\ &\text{Transition:} && 2300 < Re < 4000 \\ &\text{Turbulent:} && 4000 \leq Re \end{aligned} \tag{2.12}$$

2.1.4 The Laminar Pipe Friction Coefficient

A flow in a pipe is laminar whenever the radial velocity components are zero, i.e. we only have axial flow. A commonly used criterion for laminar flow is that the Reynolds number should be less than 2300, see equation (Re2). The laminar friction coefficient originates from an elegant analytical solution of the Navier-Stokes equation that was first done by J. Hagen and J. L. Poiseuille in 1840 [7]. This coefficient will prove useful in the work to come, so we will now take a look at the derivation.

We start with the momentum equation for flow in the x-direction as shown in Figure 2.3:

$$\frac{\partial u}{\partial t} + (\vec{V} \cdot \nabla)u = -\frac{1}{\rho}\frac{\partial P}{\partial x} + g_x + \nu\nabla^2 u \tag{2.13}$$

where u is the velocity component in the x-direction, ∇ is the spacial differential operator and $\vec{V}$ is the velocity vector.

Assuming steady flow, the first term on the left hand side disappears. Furthermore, we neglect the axial gravity component. Also, we impose the condition that only the axial velocity component is nonzero: $v = w = 0$. The continuity equation in cylindrical coordinates gives us the last condition for the velocity derivatives [7]:

$$\frac{\partial u}{\partial x} = 0 \tag{2.14}$$

Applying the above conditions, the second term on the left hand side of equation (2.13) vanishes. Moreover, the radial component of the momentum equation leaves us with the condition that there is no radial pressure drop, $\partial P/\partial r = 0$. This implies that the pressure gradient is purely axial: $\nabla P = dP/dx$. We can now write the remaining part of equation (2.13) in the following way [7]:

$$\frac{dP}{dx} = \frac{\mu}{r}\frac{d}{dr}\left(r\frac{du}{dr}\right) = const \tag{2.15}$$

By integrating this expression twice, we get the velocity of the fluid as a function of the distance r from the pipe center:

$$u(r) = \frac{dp}{dx}\frac{r^2}{4\mu} + C_1 \ln(r) + C_2 \tag{2.16}$$

The integration constants can be obtained by applying two boundary conditions: No-slip at $r = R$, and $u =$ finite at $r = 0$. The result is the equation for fully developed Hagen-Poiseuille flow:

$$u(r) = \left(-\frac{dp}{dx}\right)\frac{1}{4\mu}(R^2 - r^2) \tag{2.17}$$

In order to find the friction factor for laminar flow, we now find the average velocity by integrating the above expression over the pipe cross-section:

$$U = \frac{1}{\pi R^2} \int_0^R \left(-\frac{dp}{dx}\right) \frac{1}{4\mu}(R^2 - r^2) 2\pi r dr = \left(-\frac{dp}{dx}\right) \frac{R^2}{8\mu} \tag{2.18}$$

Finally, we can now substitute equation (2.8) for the pressure gradient in the above expression, and solve for the laminar friction factor. Note that the pressure drop over a distance Δx is related to the pressure gradient in the following way: $-(dP/dx) = \Delta P/\Delta x$. Furthermore, we consider the pressure drop over the entire liquid column of length L, so that $\Delta x = L$.

$$U = \frac{\Delta P}{L} \frac{R^2}{8\mu} = \lambda \frac{\rho U^2}{2D} \frac{D^2}{32\mu}$$

$$\Rightarrow \lambda = \frac{64\mu}{\rho D U} = \frac{64}{Re} \tag{2.19}$$

2.1.5 Velocity Profiles in Turbulent Flow

Flow in a pipe is turbulent whenever there are radial velocity components present. Even though laminar flow starts to break up at a Reynolds number around 2300, we do not have fully turbulent flow before the Reynolds number has reached 4000, see equation (2.12). We will now look at how a turbulent friction factor can be deduced by integrating the velocity profile.

Unlike the case of laminar flow, there is no exact relation describing the velocity profile in turbulent flow. We therefore have to start by looking at the mathematical connection between the shear stress and the turbulent velocity profile. This section will give a brief overview of the basic principles behind the turbulent velocity profiles in steady, smooth pipe flows. The velocity profile resulting from this section will later be used in the derivation of Prandtl's friction relation.

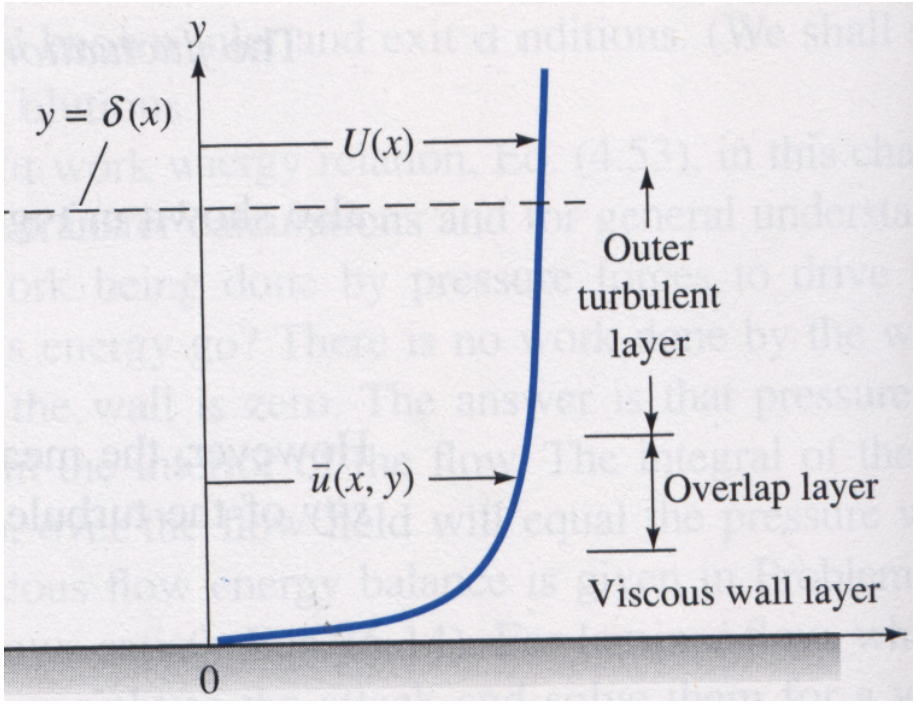

Figure 2.4: A figure showing the three regions of the turbulent boundary layer; the viscous wall layer, the overlap layer and the outer turbulent layer. The outer turbulent layer continues all the way to the center of the pipe. From Figure 2.2 we see that the turbulent shear stress is zero once $y = \delta(x)$. The viscous shear stress component from equation (2.1) dominates the viscous wall layer, while the Reynolds stress dominates the overlap layer. The outer turbulent layer starts when the total turbulent shear starts to decay at about $y/\delta(x) = 0.3$. This depends on the Reynolds number of the flow. The figure is from [7] and has been modified.

Due to different turbulent energy mechanisms being important at different distances from a wall, the turbulent boundary layer is conventionally divided into either two [9] or three [7] regions. In the present work we use the three-region formulation depicted in Figure 2.4. Hence, we need velocity profiles for all three layers. We start with the derivation of the logarithmic law of the wall for the overlap layer [7].

Because there is a local balance between processes that supply and remove turbulent energy in the outer turbulent layer, we can say that the viscous wall layer is independent of the outer flow. For this reason, we want to specify the flow in the outer turbulent layer by a characteristic velocity scale from the viscous wall layer. This is referred to as the friction velocity [9]:

$$u_\tau = \sqrt{\frac{\tau_w}{\rho}} \tag{2.20}$$

Once the above relation is specified, the structure of the overlap layer is known. Experiments confirm that the turbulent intensity distributions scale with the friction velocity [9]. Consequently, three parameters can now be used to specify the conditions in the overlap layer: The friction velocity, the distance from the wall (y), and the kinematic viscosity ($\nu = \mu/\rho$). The mean velocity has to be a function of these three parameters, i.e:

$$u = f(u_\tau, y, \nu) \tag{2.21}$$

where u is time averaged velocity in turbulent flow at a given distance y away from the wall. The above relation was deduced by Prandtl in 1930 and implies that u is independent of the turbulent shear layer thickness [7]. From dimensional considerations we can get the following relation for the dimensionless mean velocity, an expression also known as the law of the wall:

$$u^+ = \frac{u}{u_\tau} = f\left(\frac{y u_\tau}{\nu}\right) \tag{2.22}$$

Because ν is only important very close to the wall, only u_τ and y are important for the mean velocity gradient:

$$\frac{\partial u}{\partial y} = \frac{u_\tau}{K y} \tag{2.23}$$

where K is the von Karman constant for turbulent wall flows, which has been experimentally determined to be 0.41 [7].

While keeping the dependencies in equation (2.22) in mind, we integrate equation (2.23) and get the logarithmic formulation of the law of the wall:

$$u^+ = \frac{1}{K}\left[\ln\left(\frac{yu_\tau}{\nu}\right) + C\right] \tag{2.24}$$

where C is an integration constant. Equation (2.24) is also referred to as the log law. For convenience we define [10]:

$$y^+ = \frac{yu_\tau}{\nu} = \frac{y}{y_\tau} \tag{2.25}$$

Using the above convention, equation (2.24) becomes:

$$\begin{aligned} u^+ &= \frac{1}{K}\ln(y^+) + \frac{C}{K} \\ &= A\ln(y^+) + B \end{aligned} \tag{2.26}$$

where von Karman's constant has been included in the new constants A and B. As we can see in Figure 2.5, equation (2.26) is valid for the approximate range $30 < y+ < 200$ [9]. This is the range at which the Reynolds stresses are very close to the magnitude of τ_w in Figure 2.2. For larger values of y^+, i.e. for the outer turbulent layer, corrections to equation (2.26) are needed. This is because wake formations start to become important. However, the wake turns out to be very small in pipe flow [8]. Equation (2.26) is therefore assumed to be valid all the way across the pipe, i.e. $30 < y^+$.

For values of y^+ lower than 30, we see from Figure 2.5 that the logarithmic law of the wall does not coincide with experimental data. This is because the shear stress is not dominated by the Reynolds stresses any more. Very close to the wall, the shear stress is dominated by the viscous shear stress, as we can see in Figure 2.2. This corresponds to the inner part of the viscous wall layer in Figure 2.4, called the viscous sublayer. By considering the no-slip condition and the continuity equation in this region, it can be shown [9], that the velocity profile takes the following form:

$$\frac{u}{u_\tau} = \frac{yu_\tau}{\nu} = y^+ \tag{2.27}$$

$$\Rightarrow u^+ = y^+ \tag{2.28}$$

which is also referred to as the wall law. From Figure 2.5 we see that the validity range of this expression is approximately $y^+ < 8$. In the range $8 < y^+ < 30$ extensions of equations (2.26) and (2.28) are used to estimate the velocity, as shown in Figure 2.5.

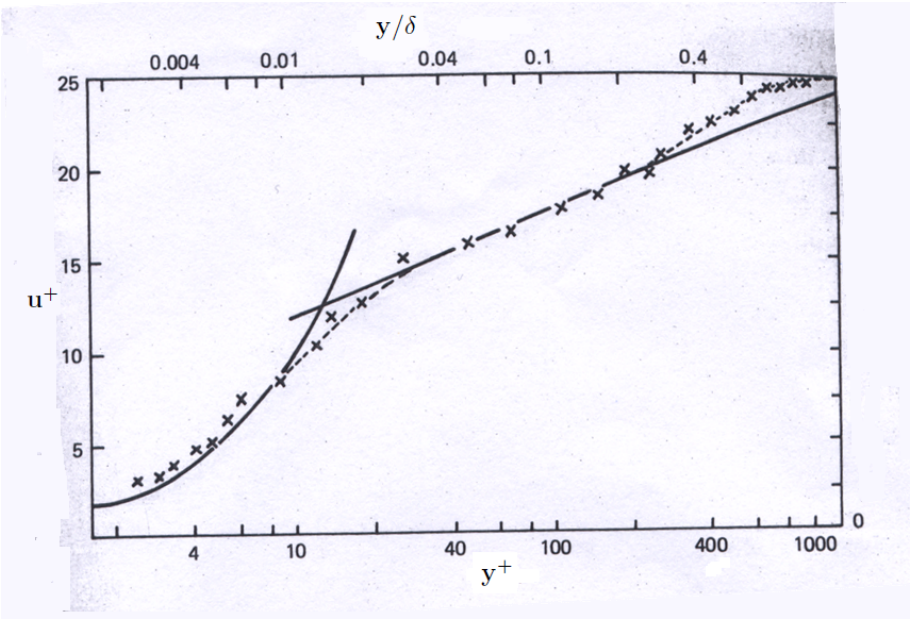

Figure 2.5: A figure showing the profile of u^+ w.r.t. y^+ for the viscous wall layer, overlap layer and a part of the outer turbulent layer. The solid line to the left is the velocity profile from equation (2.28), while the solid line to the right is the logarithmic velocity profile from equation (2.26). Cross points denote experimental data. The point at which the Reynolds stresses start to decay is approximately where the experimental data deviates from the logarithmic law at $y/\delta \approx 0.2$. The figure is from [9] and has been modified.

Summing up the results of this subsection, we now have one logarithmic law and one linear law. Both are limited to incompressible, steady flow in smooth pipes. Also keep in mind that u^+ is a time average because the velocities in turbulent flow constantly change with time. Using approximations, we have two velocity profiles that together cover the entire cross-section of the pipe with reasonable accuracy.

$$\begin{aligned} u^+ &= A\ln(y^+) + B \qquad y^+ > 30 \\ u^+ &= y^+ \qquad\qquad\qquad\quad y^+ < 8 \end{aligned} \tag{2.29}$$

2.1.6 Steady Turbulent Friction Relations

Four steady turbulent friction relations of different complexity will now be presented, starting with the derivation of Prandtl's friction relation.

Prandtl's Friction Relation for Smooth Pipes

Now it is time to use the velocity profiles from the previous subsection and piece them together to a friction relation. By computing the mean velocity from the logarithmic law of the wall, Prandtl derived an expression for the turbulent friction factor in 1935 [7]. This section aims to give a description of how the steady turbulent friction factors can be theoretically derived[1]. This is a useful exercise for realizing the approximations that have to be made. It will also give a good background for later discussion on how to find a suitable addition to traditional friction relations.

The range for which equation (2.28) is valid is so small that it is considered negligible in this context. Hence, we are left with one velocity profile for the entire cross-section of the pipe, with the exception of a thin layer closest to the wall. The next thing we do is to relate equation (2.26) to a characteristic free stream parameter, the velocity at the center of the pipe. By doing this, the unknown constant B can be replaced.

$$\begin{aligned} u^+(y = y_c) = u_c^+ &= A \ln\left(\frac{y_c}{y_\tau}\right) + B \\ &= A\ln(y_c) - A\ln(y_\tau) + B \\ \Rightarrow B &= u_c^+ - A\ln(y_c) + A\ln(y_\tau) \end{aligned} \tag{2.30}$$

where y_c is the value of y at the center of the pipe, which is the same as saying that $y_c = R$. Substituting this back into the original equation, we get:

$$\begin{aligned} u^+ &= A\ln(y) - A\ln(y_\tau) + u_c^+ - A\ln(R) + A\ln(y_\tau) \\ \Rightarrow u^+ &= u_c^+ + A\ln\left(\frac{y}{R}\right) \end{aligned} \tag{2.31}$$

In order to obtain the spatially averaged velocity, equation (2.31) now has to be integrated from a small distance from the wall, $y = \theta$, to the center of the pipe, $y = R$. Instead of displaying all the integrals of the derivation, only the result will be shown here. The full derivation is given in Appendix 6.1. The resulting expression from the spatial averaging of the logarithmic velocity profile is as follows:

$$U^+ = u_c^+ - \frac{3}{2}A \tag{2.32}$$

[1] The following derivations have been done with the help of supervisor Ole-Jrgen Nydal. Similar derivations are also given in [7] and [10].

The next thing we need is an expression for the center velocity, u_c^+. We recall from equation (2.20) that the friction velocity is related to the wall shear stress in the following way: $u_\tau = \sqrt{\tau_w/\rho}$. Using equation (2.30) with $y_c = R$, we can thus write the center velocity as a function of R, ρ, ν and τ_w:

$$\begin{aligned} u_c^+ &= A \ln\left(\frac{R u_\tau}{\nu}\right) + B \\ &= A \ln\left(\frac{R}{\nu}\sqrt{\frac{\tau_w}{\rho}}\right) + B \end{aligned} \tag{2.33}$$

The relation between the wall shear stress and the Darcy-Weicbach friction coefficient is given in equation (2.9). Using this relation and substituting equation (2.33) into equation (2.32), we get:

$$\begin{aligned} U^+ &= A \ln\left(\frac{D}{2\nu}\sqrt{\frac{\lambda \rho U^2}{8\rho}}\right) + B - \frac{3}{2}A \\ &= A \ln\left(\frac{DU}{\nu}\frac{\sqrt{\lambda}}{4\sqrt{2}}\right) + B - \frac{3}{2}A \\ &= A \ln(Re\sqrt{\lambda}) - \ln(4\sqrt{2}) + B - \frac{3}{2}A \end{aligned} \tag{2.34}$$

By expanding U^+ from equation (2.34) we get a relation that links the spatially integrated mean velocity of the pipe, U, to the friction coefficient, λ.

$$\frac{U 2\sqrt{2}}{U\sqrt{\lambda}} = A \ln(Re\sqrt{\lambda}) - \ln(4\sqrt{2}) + B - \frac{3}{2}A \tag{2.35}$$

The mean velocities cancel and the constant terms are joined into new constants, C_1 and C_2. Equation (2.35) thus assumes the following form:

$$\frac{1}{\sqrt{\lambda}} = C_1 \ln(Re\sqrt{\lambda}) + C_2 \tag{2.36}$$

This is Prandtl's universal law of friction for smooth pipes, which he derived in 1935 [10].

Adjusting the constants to experimental data, he formulated his famous friction relation in the following way:

$$\frac{1}{\sqrt{\lambda}} = 2\ln(Re\sqrt{\lambda}) - 0.8 \tag{2.37}$$

From the steps in the derivation of this equation, we understand that this by no means is an exact analytical solution for the steady turbulent friction coefficient. Nearly 80 years later, this still does not exist. Each of the approximations made on the way are not severely crude, but together they explain the discrepancies between theory and experiment. This is important to remember when working with turbulent friction relations.

Colebrook's Friction Relation for Fully Rough Turbulent Flows

The velocity profiles in equations (2.26) and (2.28) are only valid if the pipe walls are smooth. Prandtl's friction relation is thus also only valid for smooth turbulent flow. In 1939 Colebrook therefore combined the smooth wall expression in equation (2.37) and an expression for rough wall friction developed by Nikuradse [7].

In the logarithmic velocity profile for fully rough pipe flows, the average height of the roughness is denoted by k. The fully rough velocity profile has the following form [8]:

$$u^+ = A\ln\left(\frac{y}{k}\right) + C \tag{2.38}$$

This logarithmic formulation has the same validity range as equation (2.26), i.e. $y^+ > 30$. We see that there is no dependence on the viscosity in equation (2.38). This is because the roughness destroys the boundary layer [8]. As we see in Figure 2.6, the wall roughness thus increases the turbulent friction in the pipe.

Colebrook's formula for the steady turbulent friction factor is then given in the following way [7]:

$$\frac{1}{\sqrt{\lambda}} = -2\log\left(\frac{2.51}{Re\sqrt{\lambda}} + \frac{\epsilon}{3.7D}\right) \tag{2.39}$$

where D is the diameter of the pipe and $\epsilon = k/D$ is called the relative roughness.

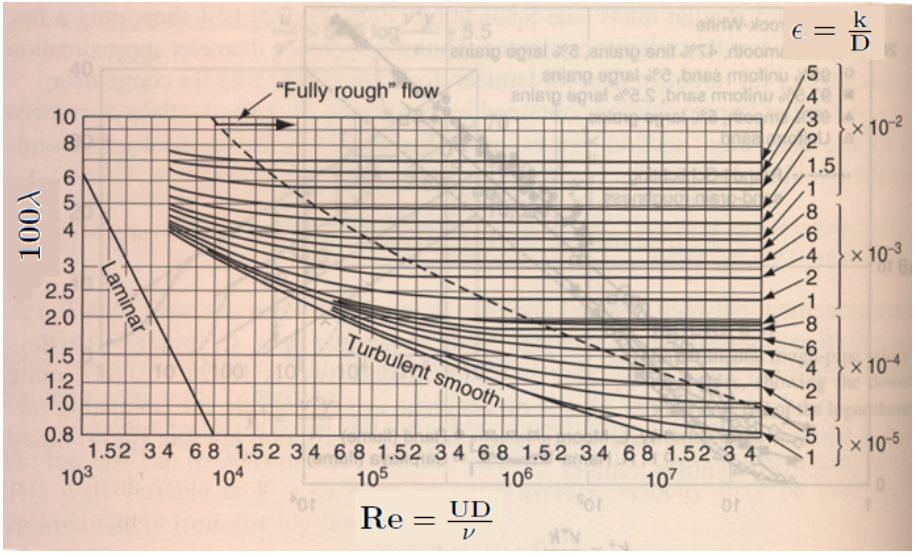

Figure 2.6: A figure showing the effect of relative roughness (ϵ) on the turbulent pipe friction factor. Prandtl's friction relation will be the "turbulent smooth" line. Both axes are logarithmic. The figure is from [8].

Haaland's Friction Relation for Fully Rough Turbulent Flows

Equation (2.39) is an implicit formula and has to be iteratively solved for every time step. To avoid this cumbersome evaluation, Haaland proposed the following approximation in 1983:

$$\frac{1}{\sqrt{\lambda}} \approx -1.8 \log\left(\frac{6.9}{Re} + \left[\frac{\epsilon}{3.7D}\right]^{1.11}\right) \tag{2.40}$$

Equation (2.40) is one of the most widely used approximations of Colebrook's relation and agrees with equation (2.39) to within 1.5% at any given point [7].

Blasius' Empirical Friction Relation

In addition to the expressions that are more or less theoretically derived, it is worth paying attention to the first correlation that was developed for turbulent pipe friction. In 1911, Blasius used experimental data from turbulent pipe flow to create an empirical relation for the friction coefficient λ. He proposed that the friction in steady turbulent pipe flow should scale with the Reynolds number. His expression does not take surface roughness into account, but is nevertheless sometimes used in simulations because of the simplicity of the formulation [7]:

$$\lambda = \frac{0.3164}{Re^{0.25}} \tag{2.41}$$

Relevance to the Present Work

As mentioned initially, steady friction coefficients such as those presented in Sections 2.1.6 - 2.1.6 have already been shown to be insufficient for the case of oscillating flow in a U-tube [11]. Nevertheless, they are often used as "base expressions" in more advanced friction models. In order to determine which of them that should be used in later models, they will be compared in U-tube simulations. The implicit relations will be iteratively solved by use of the Newton-Raphson method. Each coefficient expression has its own limitations and inaccuracies [4], so the most advanced expression is not necessarily the best for this particular case.

2.2 U-tube-Specific Steady Friction Relations

In the previous section we looked at some of the classical steady turbulent friction coefficients. They are used in all kinds of steady turbulent flows because they have been proven to be quite effective in describing turbulent friction. Before considering the more advanced unsteady friction models, we look at a couple of steady friction relations that are more specific to the U-tube. We start by considering the friction contribution from a pipe bend. Then we look at an expression specifically developed for oscillating flow in a U-tube. Last in this section, two preliminary friction models are proposed. These models were made from the experiences and observations that have been done so far, but they are not the final result of the friction study.

It should also be noted that the following work on friction relations was done with the U-tube in Figure 2.7 in mind. The friction relation study in this thesis was first and foremost directed towards the U-tube that had a constant inner diameter, like the one depicted in the figure.

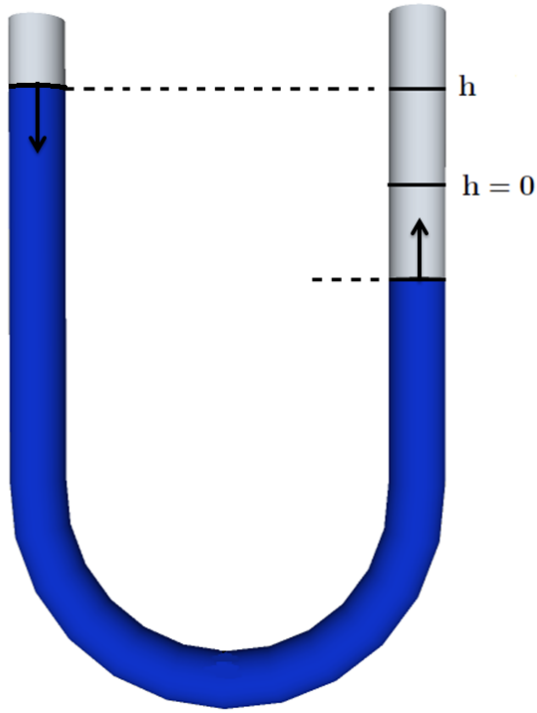

Figure 2.7: A figure illustrating oscillating flow in a U-tube with a constant inner diameter. The liquid has been displaced from its equilibrium position ($h = 0$) and left to oscillate freely. The arrows show the direction of the flow, while h is the amplitude of the oscillations. Gravity will drive the oscillations because of the height difference in the two legs. Friction will cause the oscillation amplitude to decay until the liquid eventually comes to rest. The column of liquid that is oscillating in the U-tube will be referred to as ”the liquid column”.

2.2.1 Flow in a Bend

One of the most self-evident contributors to additional friction in a U-tube is the bend itself. The flow is changing direction, so there has to be losses. Moreover, since we are considering oscillating flow, the liquid column is subjected to the extra friction during every single oscillation. The question that remains to be answered is therefore: Is the extra friction contribution enough to make simulations more accurate? The simulation results from this model are presented in Section 4.3.1.

The Secondary Flow Pattern

When fluid flows through a bend, it is subjected to a pressure force from the pipe wall of the outer part of the bend. It is this force which makes the flow change direction. The magnitude of the friction caused by this force is dependent on the curvature of the bend (R_0) and the bend angle (θ) [7, 13, 4]. As a result of this additional pressure force, the flow pattern in the bend changes. It assumes a helical shape and is often referred to as secondary flow. Because of the secondary flow pattern, depicted in Figure 2.8, the liquid experiences more friction when flowing through a bend.

There is more to the flow pattern than this crude explanation [12], but we are not going into more details on this. The important point is that the flow pattern is altered because of the bend and that this creates additional friction.

Idelchik's Method

In order to quantify the possible friction contribution from flow in a bend, we have to use a bend friction model. Most methods for calculating friction in bends are made for use in turbulent flow. This also goes for the method that will be considered here, namely Idelchik's method. It is widely used, and is among the most general methods for calculating bend friction [4].

On the other hand, Idelchik's method is valid for fully developed turbulent flow, which demands that the bend is located at least 30 diameters from any other disturbance. This does not hold for the case of oscillating flow in a U-tube. However, Idelchik's method is the closest we get to an appropriate method and a proof of concept. The friction coefficient for flow in a bend has the following form [4]:

$$\lambda_I = \frac{k_1 k_2 D}{L} + 0.0175\theta_b \frac{R_0}{L}\lambda \tag{2.42}$$

where λ is the Darcy-Weisbach friction factor and D is the pipe diameter. L is the length of the pipe section in question. k_1 and k_2 are related to the radius of curvature and angle of the bend, and are described in the following expressions:

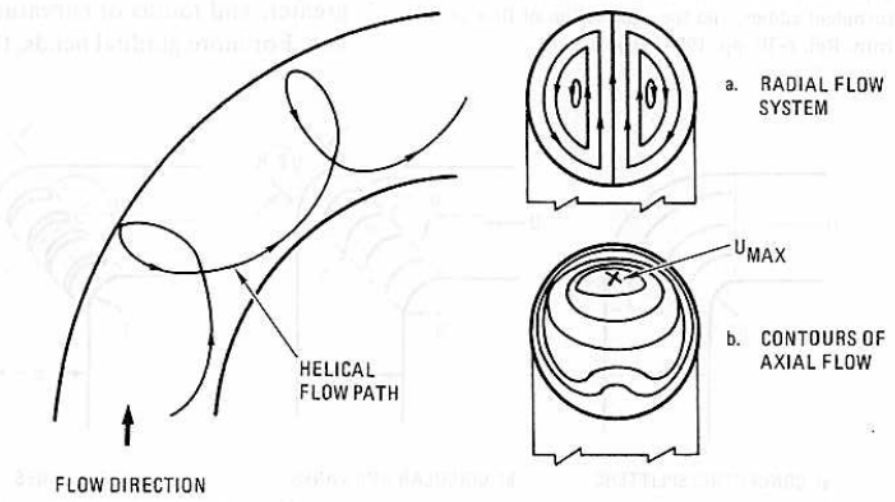

Figure 2.8: A figure from [13], illustrating the secondary flow pattern that occurs during flow through a bend in a circular pipe. The additional pressure from the outer pipe wall forces the liquid to flow radially towards the inner wall of the pipe. This creates two counter-rotating vortices, illustrated in part a). The axial flow then causes the entire system to assume a helical-shaped flow pattern.

$$k_1 = \frac{0.21}{(R_0/D)^{2.5}} \qquad 0,5 \leq \frac{R_0}{D} \leq 1 \tag{2.43}$$

$$k_1 = \frac{0.21}{(R_0/D)^{0.5}} \qquad \frac{R_0}{D} > 1 \tag{2.44}$$

$$k_2 = 1.9244 \cdot 10^{-7}\theta_b^3 - 9.0438 \cdot 10^{-5}\theta_b^2 + 0.017871\theta_b \tag{2.45}$$

Since the friction coefficient in equation (2.42) contains λ, the result is a friction term that combines the Darcy-Weisbach friction factor and the friction contribution from the bend. A steady turbulent friction coefficient such as one of those mentioned in Sections 2.1.6-2.1.6 is usually used for λ.

2.2.2 Ogawa's Method for Oscillating Flow in a U-tube

The challenges of simulating oscillating flow in a U-tube system were investigated in the thesis work presented in [3]. This work was specifically aimed at the damping of liquid oscillations in hydroelectric power plants. The damping model which was tested in this thesis was that of Ogawa et al.[14], which is a friction relation specifically designed for oscillating flow in a U-tube. Their paper is thus one of the few publications on this particular subject. Similar work has also been published in [15] and [16]. However, these are very general and do not offer a concrete solution. Another thesis on the subject, [11], will be discussed later. In the following section we will look closer at Ogawa's particular damping model in order to see if it is suited for the general case of U-tube oscillations. The simulation results from this model are presented in Section 4.3.2.

In their paper, Ogawa et al. proposed a damping factor that is comprised of empirical constants that rely on the pipe diameter, initial amplitude, liquid column length, and viscosity. The resulting friction coefficient is given as follows:

$$\lambda_O = \frac{400\nu}{U}\left(1 + \frac{4.5 \cdot 10^{-9}}{D^4}\right)\frac{Re_i}{8.75 + 0.0233Re_i} \tag{2.46}$$
$$Re_i = \sqrt{\frac{2g}{L}}\frac{h_0 D}{\nu}$$

where Re_i is called the imaginary Reynolds number and h_0 is the initial amplitude of the oscillations. An interesting observation is that we see the same velocity dependence in equation (2.46) as in the laminar friction factor from Section 2.1.4. This made it possible for Ogawa et al. to obtain an analytical equation of motion for a liquid oscillating in a U-tube. In [14], the analytical solution was compared to experiments with different liquids. The analytical and experimental results were in good agreement.

However, the case for which the expression in equation (2.46) was tested is not entirely similar to our setup. From the schematics in the paper, it seems like the U-tube was made up by two vertical pipes and one horizontal pipe that were connected by 90 degree bends. Moreover, the initial amplitudes were small; 5cm and 10cm. The resulting flow had a maximum Reynolds number of 6600, which is an order of magnitude lower than in the experiments of [11]. It will therefore be interesting to see if the model proposed in [14] holds for larger amplitudes and higher Reynolds numbers.

2.2.3 Two Preliminary Proposed Friction Models for Oscillating Flow in a U-tube

Two new U-tube-specific friction models have been developed, based on the results from the friction coefficient models that were presented in Sections 2.1.6 - 2.2.2. These results are displayed in Sections 4.1 - 4.3.2. This section will therefore serve as a summary of the steady friction coefficient sections, where the best ideas are combined. It will also serve as a transition to Section 2.3, because it has been observed that the acceleration can be a useful parameter to include in a friction relation. The simulation results from the two new friction relations are presented in Section 4.3.3.

In the models we have seen so far, the friction relations follow the experimental results to a very large extent as long as the Reynolds number is sufficiently high. However, problems arise when the amplitude of the oscillations becomes small. In order to find a suitable damping relation we should therefore focus on some of the special characteristics of the oscillating flow in a U-tube.

What is special about oscillating flow in a U-tube is that we have periodic acceleration and deceleration of the flow until it eventually comes to rest. We thus have a moment when the liquid is turning at every half period. The liquid at the center of the pipe is moving faster than that closer to wall because it is less affected by the wall friction. Hence, it is reasonable to assume that it will take a longer time before it eventually turns. During the acceleration on the way back, the center liquid will experience less drag and therefore move faster than the wall liquid again. During this turning process, the velocity undergoes big changes, where the velocity gradients can be enormous [4]. This could cause more internal friction in the liquid column and thus slow down the flow. This could be one reason why the traditional friction relations are not sufficient for the U-tube simulations.

A New U-tube-Specific Steady Friction Relation
In Section 4.3.2 it becomes clear that the expression of Ogawa et al. is more effective than the other steady friction relations when it comes to damping the oscillations in the U-tube. However, their expression does not yield satisfying results for our type of U-tube. It is therefore tempting to make a steady U-tube-specific friction relation that might be more effective. In the spirit of what Ogawa et al. presented in [14], we use the laminar friction factor as a starting point, and multiply by a constant:

$$\lambda_{laminar} = C\frac{64}{Re} \tag{2.47}$$

where the constant, C, was determined by trial and error. A manual best-fit procedure was done by visually comparing plots to all available data from [11], followed by trial and error in a spread sheet.

The resulting constant is inspired by the Reynolds number and is dependent on the liquid density, the liquid viscosity, the liquid column length and the diameter of the pipe:

$$C = \frac{D\rho}{75L^{0.3}\mu^{0.4}} \tag{2.48}$$

where L is the length of the liquid column. Another improvement to the method of Ogawa is that the turbulent friction coefficient is also going to be used in this new friction model. The combination of the two is shown in equation (2.52).

A New U-tube-Specific Acceleration Based Friction Relation
When trying to address the extra friction related to turning, the logical thing to do is to use a parameter that is prominent during this process. The acceleration is such a parameter. It has its local maximum whenever the liquid column i turning. Furthermore, it will be zero in steady flow, giving us the opportunity of adding an extra friction term. Once using the acceleration in a friction relation, it becomes an unsteady friction relation. Another option would be to divide by the velocity, like Ogawa et al. did in their friction expression. Results have shown that this gives good damping, because the velocity is small whenever the liquid is turning.

Since the liquid is moving slowly at the time of turning, it is reasonable to assume that the flow is mostly in the laminar regime. For this reason, the acceleration will be related to the laminar friction factor in the new friction relation. Moreover, because the velocity appears in the denominator of the laminar friction factor, it should provide more damping when the velocity is low. When the acceleration is zero, we do not want any additional friction. It is therefore desirable to use a friction relation on the following form:

$$\lambda_{laminar} = \left(1 + \left|\frac{\partial U}{\partial t}\right|\right)\frac{64}{Re} \tag{2.49}$$

where U is the mean velocity. The weakness of this formulation is that we do not know if the acceleration term is of the right order of magnitude compared to the rest of the expression. We therefore multiply the acceleration by a scaling constant, C_a:

$$\lambda_{laminar} = \left(1 + C_a\left|\frac{\partial U}{\partial t}\right|\right)\frac{64}{Re} \tag{2.50}$$

In addition to having a maximum whenever the velocity is small, this expression also increases linearly with the acceleration. Hopefully, this will give a well-timed addition to the friction. C_a has to be determined by trial and error with experimental data and a spread sheet in the same manner as C from equation (2.48).

The resulting coefficient is similar to that in equation (2.48), but the length dependence has been omitted:

$$C_a = \frac{D\rho}{100\sqrt{\mu}} \tag{2.51}$$

Like the laminar expression from equation (2.47), the expression in equation (2.50) will also be combined with a turbulent friction coefficient. The difference is that we have now entered into the unsteady domain by using the acceleration in the friction relation.

Combining the Laminar and Turbulent Friction Coefficients
In order to have an expression that is valid in both the turbulent and laminar regimes, we also use the steady friction relation of Blasius as the turbulent component. The best way to combine these two expressions without creating discontinuities is to use a maximum-function:

$$\lambda = max\{\lambda_{laminar}, \lambda_{turbulent}\} \tag{2.52}$$

This friction term will provide a smooth transition between turbulent and laminar friction. It will also guarantee the maximum possible friction in both flow regimes. The increase of the laminar friction factor makes it larger for small Reynolds numbers, which is where the turning occurs. It also makes the laminar friction dominate the transitional region.

2.3 Unsteady Friction Relations

Most of the work on unsteady friction models that exist for pipe flow, is related to studies of sudden increases or decreases in the flow rate in long pipes (for instance: [2, 6, 17, 18]). These types of flow cases are often connected to the study of the water hammer phenomenon. This is not something that will be of relevance to the U-tube flowing case, because the flow is never forced to a sudden stop.

On the other hand, the sudden stops in the flow create liquid oscillations in the pipes. Hence, there may be some expressions that could be very useful in the U-tube case as well. Moreover, a lot of the research that has been done in connection with water hammer models has gone into finding better friction relations. Since the water hammer flow case involves unsteady, oscillating flow, these friction relations could be directly applicable to the U-tube case.

The existing 1D models for unsteady contributions to shear stress in pipe flow can be divided into three groups [5]. The first group of models is based on instantaneous acceleration, the second group is using past velocities or accelerations, and the third group is based on irreversible thermodynamics. The first two groups are the most widely used, so one model from each group will be further investigated in the following sections.

It should also be noted that 2D methods for unsteady friction have also been developed. The advantage of 2D models is that they can provide much more details about the flow and velocity profiles than the 1D models. They continuously give an actual velocity profile and the corresponding energy losses during the transient processes [2]. However, the disadvantage is that they are much more computer heavy for extensive pipe networks. Hence, the 2D models can be used to validate 1D results for certain areas, but they are normally not used for larger systems.

2.3.1 Frequency-Dependent Friction Models

The group of methods that rely on past velocities or accelerations is based on Zielke's analytically derived model for unsteady laminar flows [19]. He modified the method of characteristics to include a frequency dependence of the wall shear stress. This was to accommodate for his statement that the wall shear stress is not in phase with the mean velocity, but rather the pressure gradient. He justified this by the observation that the boundary layer and the inner region of the pipe react differently to pressure gradients.

In the boundary layer, the viscous forces are large compared to the inertial forces. Therefore, the velocity near the wall is in phase with the pressure gradient. The inertial forces are dominating in the inner region of the pipe, which makes the pressure gradient be in phase with the acceleration of the fluid. Because of this, a sudden change in the pressure gradient will first affect the boundary layer. The shear stress at the wall will therefore change before the mean velocity is changed.

In order to account for this phase difference, Zielke used a weighting function to give the flow a memory of past acceleration values [6, 2]. His method was a convolution integral over the past fluid accelerations and a step response multiplied by the weighting function. The convolution makes the method very computer heavy compared to other models. However, the method is based on a 2D equation of motion and allows to account for possible changes in time of the velocity field across the cross-section of the pipe [20].

Zielke's original expression for the head loss friction in unsteady laminar flow is given as follows [19]:

$$h_f = \frac{32\nu}{gD^2} + \frac{16\nu}{gD^2} \int_0^t \frac{\partial U}{\partial t}(u) W(t-u) du \tag{2.53}$$

where ν is the kinematic viscosity and W is the weighting function. We recognize the first term as the head loss for steady laminar flow. The second term is the term that takes the unsteady effects into account.

It has been shown that Zielke's method yields good results for laminar transient friction cases [19]. Moreover, other frequency-dependent friction models have proven to be good for laminar U-tube oscillations [15]. However, Zielke's method did not yield satisfactory results when it was tested in a turbulent U-tube simulation and compared to experimental data [16]. What this tells us is that the frequency-dependent methods might be good for the U-tube case; we only need one that is adapted to turbulent flow.

Through the past decades, Zielke's original model has been the subject of numerous efforts to improve efficiency and extend the validity range. Empirical studies of the distribution of the turbulent viscosity coefficients led Vardy and Brown to develop a two-layer model, with an outer annulus and an inner core [21, 5]. Making use of velocity profile analyses for unsteady turbulent flow, they were able to conclude that Zielke's model is applicable to unsteady turbulent flows as well. They found that the weighting function had to be related to the Reynolds number [22]. A weighting function for transient turbulent friction in both smooth and rough pipes was therefore developed [5, 23].

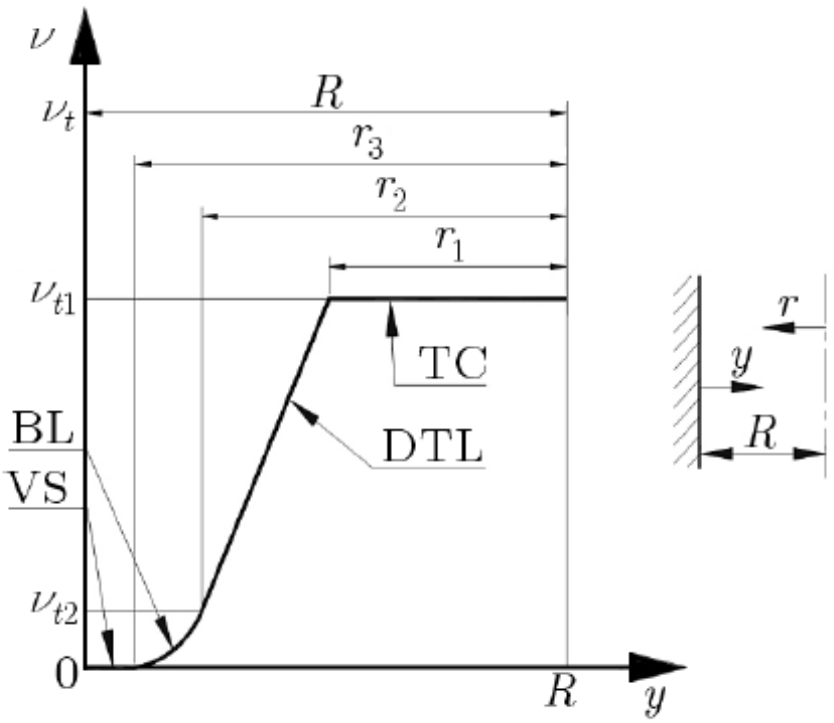

Figure 2.9: A figure from [20] that illustrates the division of the kinetic turbulent viscosity coefficient, ν_t, into four regions. ν_t: Turbulent viscosity coefficient, VS: Viscous Sublayer, BL: Buffer Layer, DTL: Developed Turbulent Layer, TC: Turbulent Core. Note that this could be interpreted as a refined version of Figure 2.4.

Multi-layer models for the viscosity distribution have culminated in the four-layer model of Zarzycki, see Figure 2.9. Distinguishing between the different layers in turbulent pipe flow was done as early as 1975. But it was Zarzycki that made use of this separation of layers in the weighting function he proposed in [24]. Later, this weighting function has been refined and made more efficient [20]. It is this model that will be implemented in the present work to represent the frequency-dependent models. The simulation results are displayed in Section 4.4.1.

The total shear stress in Zarzycki's friction model is given in the same manner as the head loss in equation (2.53):

$$\tau_w(t) = \tau_s + \frac{2\mu}{R}\int_0^t \frac{\partial U}{\partial t}(u)w(t-u)du \tag{2.54}$$

where τ_s now is the shear stress in steady turbulent flow instead of steady laminar flow. Using the relation between shear stress and the Darcy-Weisbach friction coefficient, we get:

$$\lambda = \lambda_s + \frac{32\nu}{DU|U|}\int_0^t \frac{\partial U}{\partial t}(u)w(t-u)du \tag{2.55}$$

Note that the unsteady term is divided by the square of the velocity. This implies even more damping for low velocities than in Ogawa's method. The weighting function is given as follows:

$$w_N(\hat{t}) = (c_1 Re^{|c_2|} + c_3)\sum_{i=1}^{N} A_i e^{-|b_i|\hat{t}} \tag{2.56}$$

where $i = 1, 2, ..., N = 8$. $\hat{t} = \nu t/R^2$ is dimensionless time, c_1, c_2, c_3 are coefficients and A_i and b_i are coefficient arrays of length N. All of the coefficients were determined by statistical analysis and optimization. They are given by [20]:

$$\begin{aligned} c1 &= -13.27813 \\ c2 &= 0.000391 \\ c3 &= 14.27658 \\ A &= \{0.224, 1.644, 2.934, 5.794, 11.28, 19.909, 34.869, 63.668\} \\ b1 &= \{0.10634, 8.44, 88.02, 480.5, 2162, 8425, 29250, 96940\} \end{aligned} \tag{2.57}$$

A more efficient way of calculating the convolution integral in equation (2.54) is presented in [20]. The time of the calculation is drastically reduced from an exponential increase with number of time steps to a more linear relation between the two.

2.3.2 Instantaneous Acceleration Based Models (IAB)

This group of models is very popular for practical simulations of transient flows. As the name suggests, these models have a term based on the instantaneous local acceleration of the flow. They have a long track record, from all the way back to 1956. Since then, researches have made changes and introduced new models. However, the basic idea of using the instantaneous acceleration in the unsteady friction term is still used in the most common model today, which is Brunone's friction model [5]. The simulation results for this section are displayed in Section 4.4.2.

The IAB methods originated from the work of Daily et al. in 1956 [25]. To address discrepancies between measured and calculated transients in pipe flow connected to pumps, they came up with an expression for the "unsteady flow coefficient of total drop in potential":

$$K_a = K_s + K_t + c_1 \frac{2V}{U^2 A} \frac{\partial U}{\partial t} \tag{2.58}$$

where K_s is the 1D steady-state friction coefficient and K_t is a correction coefficient for transient effects due to boundary resistance and momentum flux. Note that the unsteady term is divided by the square of the velocity, which will provide a lot of damping for low velocities. c_1 is an inertial coefficient, V is the liquid volume within the control surface, U is the mean velocity and A is the inner area.

Among those who have made changes to the friction relation in equation (2.58) were Safwat et al. [16]. Having tested Zielke's method for oscillating flow in a U-tube with unsatisfying results, they suggested the following relation as a basis for modeling the wall shear stress:

$$\tau_w = \alpha U + \beta \frac{\partial U}{\partial t} \tag{2.59}$$

where α and β are constants that were found to be dependent on the frequency of the oscillations of the liquid in the U-tube. The relation in equation (2.59) was proposed to address the inertia effects on the flow that they observed in their experiments.

In 1990, Brunone, Greco and Golia observed from experiments that there was a strong connection between pipeline inertance and the acceleration of the flow. By assuming a uniform velocity, errors are made when calculating inertial forces and wall shear stresses [22]. Hence, they developed their own model with inspiration from the early IAB models.

The first complete formulation of Brunone's friction model was presented in 1991, [26, 27]. It was comprised of a convective and a temporal acceleration term. A flow dependent coefficient was also introduced, which is referred to as Brunone's friction coefficient. The resulting expression for the head loss was:

$$h_f = h_{f_s} + \frac{k}{g}\left(\frac{\partial U}{\partial t} - c\frac{\partial U}{\partial x}\right) \tag{2.60}$$

where h_{f_s} is the head loss from steady friction, U is the average velocity and k is Brunone's friction coefficient. c is the speed at which the pressure wave propagates through the liquid in a water hammer incident [2]. The Darcy-Weisbach friction coefficient for use in equation (2.79) is thus:

$$\lambda_B = \lambda_s + k\frac{2D}{U|U|}\left(\frac{\partial U}{\partial t} - c\frac{\partial U}{\partial x}\right) \tag{2.61}$$

where λ_s is a steady turbulent friction relation. The term containing the acceleration works as an unsteady correction of the turbulent friction coefficient, which only kicks in when the flow is unsteady.

Later, Vitkovsky modified Brunone's expression, so that the convective term got the correct sign for all possible flow movements [2]:

$$\lambda_B = k\frac{2D}{U|U|}\left(\frac{\partial U}{\partial t} + c \cdot \text{sign}(U)\left|\frac{\partial U}{\partial x}\right|\right) \tag{2.62}$$

The Brunone friction coefficient then had to be determined empirically for each flowing case. Through regression analysis of empirical data, Vardy and Brown came up with a shear decay coefficient C^* [21]. It can be related to the Brunone coefficient in the following way:

$$k = \frac{\sqrt{C^*}}{2} \tag{2.63}$$

The shear decay coefficient takes the following form for laminar and turbulent flow:

$$\text{Laminar flow:} \qquad C^* = 0.00476 \tag{2.64}$$

$$\text{Turbulent flow:} \qquad C^* = \frac{7.41}{\text{Re}^{\log(14.3/Re^{0.05})}} \tag{2.65}$$

Vardy and Brown revised their work in 2002 and came up with an improved shear decay coefficient for turbulent flow [5]. In their previous model, they assumed a uniform behavior of the core region. Now, they instead assumed a uniform turbulent viscosity. In their new model, they also related the wall shear stress to the mean velocity instead of the maximum velocity. The resulting shear decay coefficient has the same form as in equation (2.65), but the magnitude is generally larger than for the previous coefficient.

$$\text{Turbulent flow:} \qquad C^* = \frac{12.86}{\text{Re}^{\log(15.29/Re^{0.0567})}} \tag{2.66}$$

Whether the update to C^* improves the results of the U-tube simulations compared to the older coefficient is not necessarily an easy question to answer. Even though the newer version is more theoretically correct, the old version might still provide us with the best results. In the simulations, both the old and the new version of Brunone's constant were therefore tested.

The convective term in equation (2.62) has no application in the present work on liquid oscillations in a U-tube. There is no pressure wave propagating in the pipe as under water hammer-like conditions. In the derivation of the equation of motion (2.79), we neglect small velocity changes along the length of the liquid column. Hence, the entire liquid column is assumed to have the same velocity, so that $\frac{\partial U}{\partial x} = 0$. The convective term can therefore be discarded. The resulting expression for the friction coefficient is then:

$$\lambda_B = k\frac{2D}{U|U|}\left(\frac{\partial U}{\partial t}\right) \tag{2.67}$$

where the sign(U)-factor has been added to ensure that the friction coefficient has the correct sign.

$$\lambda_B = k\frac{2D}{U|U|}\left|\frac{\partial U}{\partial t}\right| \cdot \text{sign}(U) \tag{2.68}$$

The final friction expression can then be written as follows:

$$\lambda = \lambda_{Blasius} + k\frac{2D}{U|U|}\left|\frac{\partial U}{\partial t}\right| \cdot \text{sign}(U) \tag{2.69}$$

Brunone's model has proven to be both accurate and computationally efficient when it applied to water hammer simulations [2, 18]. However, more recent investigations involving both simulations and experiments have shown that models which use past accelerations or velocities, such as Zarzycki's model, are more accurate [22]. The test case was, as many times before, a long pipe with a fast-closing valve. We know that this is far from analogous to the U-tube, so it remains to see if the same conclusions can be made for the modified version in equation (2.68).

We see from equation (2.68) that λ_B is added as an unsteady correction to the steady turbulent friction factor. It will only provide damping when the flow is accelerating, which is the same concept as in Daily's friction relation in equation (2.58).

2.4 Concluding Solution to U-tube Friction

This section sums up and concludes the work on friction relations for oscillating flow in a U-tube with a constant inner diameter. The goal is to use the results from all the previous sections and come up with the best possible friction relation. The simulation results from this new unsteady model are displayed in Section 4.5.

From Ogawa's method it became clear that a friction factor that has the form of the laminar friction coefficient gives a lot of damping. This is because the term containing the friction in the equation of motion will be less dependent on the velocity. It was then demonstrated that very good results can be obtained by using a formulation on the form $max\{C\lambda_{lam}, \lambda_{turb}\}$, where C is a flow dependent coefficient. Hence, the laminar and turbulent friction factors can be used in their respective flow regimes. However, this formulation changes the laminar friction factor permanently. This is not acceptable if the friction relation is to be used in a flow simulation program.

The above problem arises the need for an acceleration based friction relation. This implies that the friction factors can change whenever the flow is unsteady and then go back to their original if the acceleration of the flow is zero. As a bonus, the acceleration is at its maximum whenever the flow is turning. The process of turning could be adding extra damping to the oscillations, so it is therefore desirable to address this matter.

The friction model of Brunone has the two properties mentioned above. It is an acceleration based method and it also contains a $1/U^2$-term. The latter property addresses the turning issue because the velocity is small whenever the liquid is turning. In addition, the Brunone model contains a flow dependent coefficient called Vardy's shear decay coefficient. This assures that the friction is properly adjusted according to the Reynolds number of the flow. Using Vardy's coefficient and the principles of the Brunone model, the unsteady correction term in equation (2.68) was obtained. When combined with the regular steady turbulent friction coefficient of Blasius, this relation yielded very good results even though it did not contain a laminar component.

Vardy's shear decay coefficient, C^*, was originally only developed for turbulent flows. The derivation of the coefficient is not based on first principles, but is rather the result of regression analysis of empirical data. This allows us to use the coefficient as we see fit. Hence, the expression in equation (2.68) can be used as an unsteady correction in three different ways.

The three different options are then:

Friction coefficient with laminar correction:

$$\lambda = max\left\{\left(\frac{64}{Re} + \frac{\sqrt{C^*}}{2}\frac{2D}{U|U|}\left|\frac{\partial U}{\partial t}\right| \cdot \text{sign}(U)\right), \frac{0.3164}{Re^{0.25}}\right\} \tag{2.70}$$

Friction coefficient with turbulent correction:

$$\lambda = max\left\{\frac{64}{Re}, \left(\frac{0.3164}{Re^{0.25}} + \frac{\sqrt{C^*}}{2}\frac{2D}{U|U|}\left|\frac{\partial U}{\partial t}\right| \cdot \text{sign}(U)\right)\right\} \tag{2.71}$$

Friction coefficient with correction of the maximum:

$$\lambda = max\left\{\frac{64}{Re}, \frac{0.3164}{Re^{0.25}}\right\} + \frac{\sqrt{C^*}}{2}\frac{2D}{U|U|}\left|\frac{\partial U}{\partial t}\right| \cdot \text{sign}(U) \tag{2.72}$$

where C^* is the most recent shear decay coefficient of Vardy and Brown [5].

All of the above expression will be tested in the result section. However, the concluding expression to the present work can already be chosen. Test runs show that all of the expressions in equations (2.70 - 2.72) yield good results. The choice can therefore be made on the basis of other factors than just the performance.

After considering pros and cons of the above choices, the laminar correction in equation (2.70) was chosen. We are thus choosing a model that is very similar to the one proposed in equations (2.50), (2.51) and (2.52). The laminar correction relation will address the turning issue discussed earlier, since the turning happens in the laminar regime. Moreover, we have seen in earlier sections that the steady turbulent friction expressions do quite well for high Reynolds numbers. The crucial advantage is on the other hand that the friction model can be implemented into flow simulation programs without interfering with the established turbulence relations. Having an unsteady correction in the turbulent term can yield unwanted results in some cases. This is unlikely to happen in the laminar regime[1].

[1] This conclusion was reached after discussing with supervisor O. J. Nygaard

2.5 The Equation of Motion for the Oscillation of a Liquid Column in a U-tube

The equation of motion will be derived for two cases of oscillating flow in a U-tube. First, the case of a constant inner diameter will be considered. Next, the equation of motion for a U-tube with a change in the inner diameter will be derived. The purpose of this is to give an overview of the equations that have been computationally solved in this thesis, and moreover to gain insight to the basic force mechanisms in the flow. In both of the U-tube cases, the liquid is assumed to have been pulled out of its equilibrium position and then released to oscillate freely.

2.5.1 U-tube With a Constant Inner Diameter

Now we look at the forces acting on the liquid column in Figure 2.10 in order to derive its equation of motion. The result will be the basis of the simulations later in the present work.

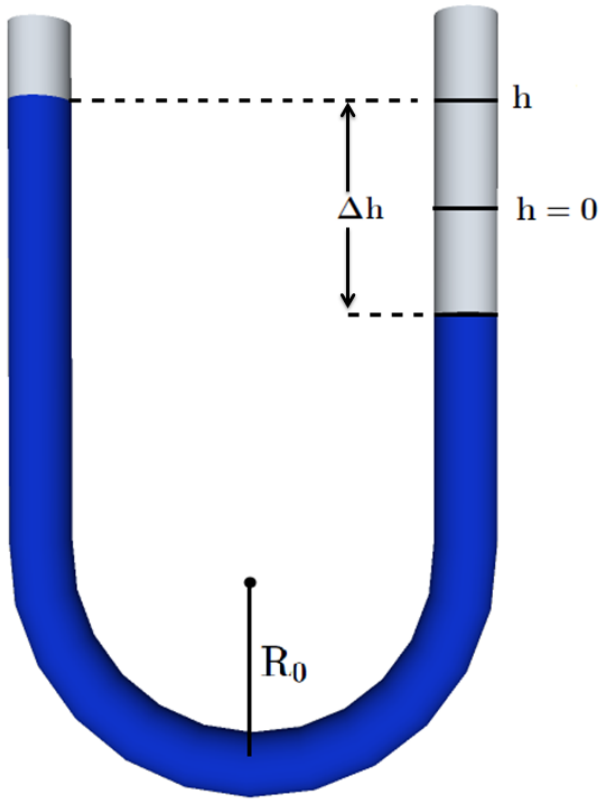

Figure 2.10: A sketch of the U-tube with a constant inner diameter. R_0 denotes the radius of the bend, $h = 0$ shows the equilibrium level of the liquid, while h is the amplitude of the liquid displacement. Δh denotes the difference between the positive and negative displacement.

The forces acting on a single point in a liquid flowing in a pipe can be written as follows:

$$\frac{\partial(A\rho U)}{\partial t} + \frac{\partial(A\rho U^2)}{\partial x} = -A\frac{\partial p}{\partial x} - S\tau_w - A\rho g\sin(\phi) \tag{2.73}$$

where A is the inner area of the pipe, ρ is the density of the liquid, and U is the mean velocity of the liquid column.
From the left to the right, the terms in this equation represent:

- Time rate of change of linear momentum, also called the accumulation term
- Convection/ transport of momentum
- Force due to pressure gradient
- Wall friction, where S is the length of the wetted perimeter of the pipe wall and τ_w is the wall shear stress.
- Force due to gravity. ϕ is the angle between the horizontal plane and the flowing direction.

In order to obtain the one-dimensional force balance for the entire liquid column, we now integrate equation (2.73) over the column length along the flowing direction, x.
For an incompressible liquid the integral over the first term becomes:

$$\int_0^L \rho A\frac{\partial U}{\partial t}dx = L\rho A\frac{\partial U}{\partial t} \tag{2.74}$$

The integral over the convective term becomes zero as we do not have any momentum flux in or out of the liquid column. Furthermore, the pipe is open in both ends. The pressure at the endpoints of the column is thus the same, so that the pressure drop over the entire column is zero.
As the liquid completely fills the pipe, the wetted perimeter is the same as the circumference of the pipe, $S = \pi D$. Because the inner area of the pipe is convenient to work with, we rewrite this expression so that $S = \pi D = 4\pi R^2/D = 4A/D$. We remember from equation (2.9) in Section 2.1.2 that the wall shear stress can be expressed as $\tau_w = (\lambda\rho U^2)/8$. Integrating the wall friction term from the force balance, we can write:

$$\int_0^L S\tau_w dx = \lambda\frac{\rho LAU^2}{2D} \tag{2.75}$$

where λ is the dimensionless Darcy-Weisbach friction coefficient.

If the liquid in Figure 2.10 is at rest, the integration over the last term in equation (2.73) cancels out all the contributions from gravity. However, if there is a height difference between the left and right leg of the tube, $dx\sin(\phi)$ will give us a vertical contribution. The integral over the gravity term thus gives us the force contribution from the total height difference:

$$\int_0^L A\rho g\sin(\phi)dx = \Delta h\rho gA = 2h\rho gA \tag{2.76}$$

where h is the displacement of the liquid column from the equilibrium level, as shown in Figure 2.10.

Collecting the results from equations (2.74), (2.75) and (2.76) we get the force balance for the liquid column:

$$\rho LA\frac{\partial U}{\partial t} = -2h\rho gA - \lambda\frac{\rho LAU^2}{2D} \tag{2.77}$$

Note that no assumptions or approximations have been applied up to this point. The only uncertainty related to equation (2.77) is coming from the unspecified friction coefficient, λ. The rate of change of the height in one of the legs of the U-tube is the mean velocity in the flowing direction, U. We can therefore convert the above force balance into a second order differential equation in h:

$$\rho LA\frac{d^2h}{dt^2} = -2h\rho gA - \lambda\frac{\rho LA}{2D}\frac{dh}{dt}\left|\frac{dh}{dt}\right| \tag{2.78}$$

The squared velocity has been split up and we use the absolute value of one of the terms. This makes the friction force always work in the opposite direction of the flow.

Dividing equation (2.78) by ρLA, we finally arrive at the equation of motion for the liquid column:

$$\frac{d^2h}{dt^2} + \frac{\lambda}{2D}\frac{dh}{dt}\left|\frac{dh}{dt}\right| + \frac{2gh}{L} = 0 \tag{2.79}$$

Oscillation Period

Now let us look at the theoretical period of the oscillations of the liquid column if friction is neglected. This can be a useful supplement when it comes to comparing computational and experimental results. By using the constant theoretical period for comparison, we can see if either the computational or the experimental results have increasing or decreasing periods.

Equation (2.79) resembles that of a damped harmonic oscillator. What makes it different is that the damping term is not linear, and it can assume different orders according to what is chosen as the friction coefficient λ. By setting the damping term to zero, we get a harmonic oscillator which we can use to find the natural period of equation (2.79).

$$\frac{d^2h}{dt^2} + \frac{2hg}{L} = 0 \tag{2.80}$$

The general solution of equation (2.80) is as follows:

$$h(t) = A\cos\left(\sqrt{\frac{2g}{L}}t\right) + B\sin\left(\sqrt{\frac{2g}{L}}t\right) \tag{2.81}$$

where $\sqrt{\frac{2g}{L}}$ is called the natural frequency of the system, which is often denoted by ω. The relationship between the period and the natural frequency of the system is $T = 2\pi/\omega$, so that the natural period of the oscillations becomes:

$$T = \frac{2\pi}{\omega} = \pi\sqrt{\frac{2L}{g}} \tag{2.82}$$

We see from equation (2.82) that the only parameter that influences the natural period is the length of the liquid column. Later we will see from the experimental data how much the frequency is affected by the damping term.

2.5.2 U-tube With an Inner Diameter Change

We now look at the flow in a U-tube that has an inner diameter change at the bottom of the bend. We start out with the equation of motion and mass balance for the liquid, with the origin at the bottom of the bend (Figure 2.11) [1].

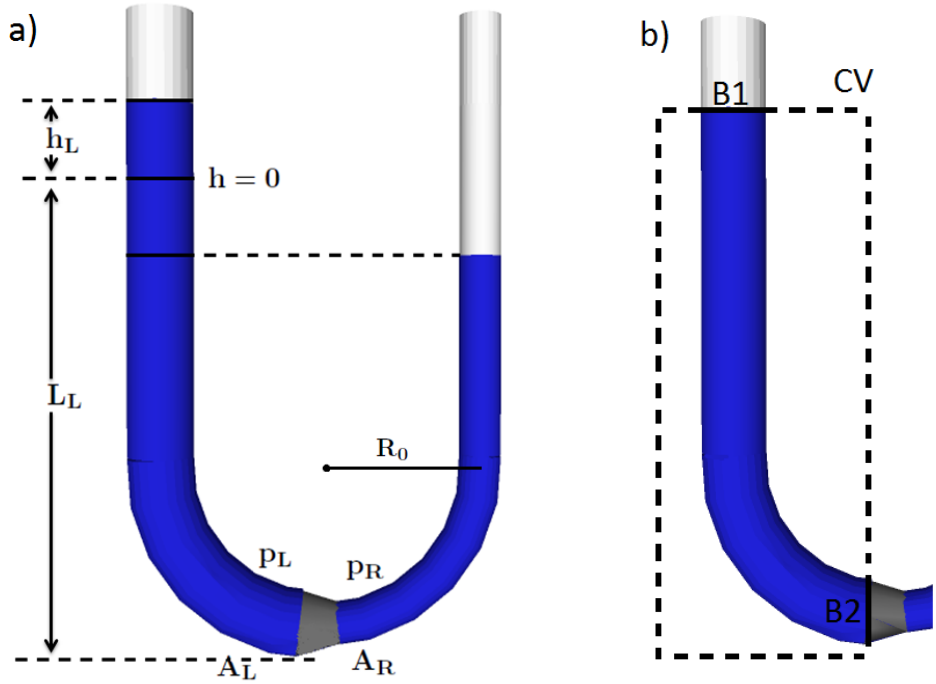

Figure 2.11: a) A sketch of the U-tube with an inner diameter change at the bottom of the bend. R_0 denotes the radius of curvature of the bend and $h = 0$ shows the equilibrium level of the liquid. h_L is the height displacement of the interface from the equilibrium in the left leg, while L_L is the length of the liquid column in the left leg of the tube. p_L, p_R, A_L and A_R are the pressures and inner areas on the left and right hand side of the cone-shaped coupling between the tubes.
b) An illustration of the control volume used in the integration of the force balance in the left leg of the U-tube. The boundaries of the control volume (B1 and B2) are drawn at the liquid interface and to the left of the cone-shaped coupling.

[1] The derivations in this section have been done with assistance from supervisor Ole-Jrgen Nydal

We start by looking at each leg of the U-tube in Figure 2.11 separately, as shown in part b) of Figure 2.11. Defining the positive flowing direction from the left to the right, we integrate the force balance from equation (2.73) over the control volume of the left leg. The result is:

$$L_L \partial_t \left(\rho A_L U_L\right) + \rho A_L \left[(U_L - U_{B2})^2 - (U_L - U_{B1})^2\right] = -\Delta p A_L - F_L + \rho h_L A_L g \tag{2.83}$$

where L_L and h_L are the liquid column length and the height of the interface in the left leg of the tube, respectively. F_L denotes the integrated wall friction force, which we are familiar with from the previous section: $F_L = \lambda_L \rho A_L L_L U_L^2/(2D_L)$. ∂_t is the short-hand notation for the time rate of change. $(U_L - U_{B2})$ and $(U_L - U_{B1})$ accommodate for the deformation of the control volume, where U_{B2} and U_{B1} are the velocities of the two boundaries of the left leg control volume. Δp is the pressure difference between the two boundaries of the control volume, $\Delta p = p_{B2} - p_{B1}$.

The mass balance for the left leg of the tube can be integrated in a similar manner as the force balance. The result is:

$$L_L \partial_t \left(\rho A_L\right) + \rho A_L \left[(U_L - U_{B2}) - (U_L - U_{B1})\right] = 0 \tag{2.84}$$

We now consider the convection terms of equations (2.83) and (2.84). The velocity of the interface boundary, U_{B1}, is the same as the mean velocity in the left leg of the tube. Therefore, $U_L - U_{B1} = 0$. The other boundary of the control volume, B2, is stationary. Hence, $U_{B2} = 0$. Once the convection terms have been sorted out, the momentum and mass balances take the following forms:

$$\text{Momentum:} \quad L_L \partial_t \left(\rho A_L U_L\right) + \rho A_L U_L^2 - 0 = -\Delta p A_L - F_L + \rho h_L A_L g \tag{2.85}$$

$$\text{Mass:} \quad L_L \partial_t \left(\rho A_L\right) + \rho A_L U_L - 0 = 0 \tag{2.86}$$

Now we expand the time derivative of the momentum equation, which then becomes:

$$L_L \partial_t (\rho A_L U_L) = L_L U_L \partial_t (\rho A_L) + L_L \rho A_L \partial_t U_L \tag{2.87}$$

The time derivate from the mass balance in equation (2.86) can now be substituted into the second term of the expansion in equation (2.87). The resulting momentum balance is then:

$$\begin{aligned} L_L\rho A_L\partial_t U_L + U_L(-\rho A_L U_L) + \rho A_L U_L^2 &= -\Delta p A_L - F_L + \rho h_L A_L g \\ L_L\rho A_L\partial_t U_L &= -\Delta p A_L - F_L + \rho h_L A_L g \\ L_L\partial_t U_L &= -\frac{p_L - p_0}{\rho} - \frac{F_L}{\rho A_L} + h_L g \end{aligned} \tag{2.88}$$

where we recall that $\Delta p = p_{B2} - p_{B1}$. p_{B1} is the atmospheric pressure, p_0, because the U-tube is open in both ends. $p_{B2} = p_L$, which is the pressure at the left hand side of the cone-shaped coupling in Figure 2.11.

The momentum equation for the right hand side leg of the U-tube can then be written on the exact same form as in equation (2.88), only with an opposite definition of direction for h_R:

$$L_R\partial_t U_R = -\frac{p_0 - p_R}{\rho} - \frac{F_R}{\rho A_R} - h_R g \tag{2.89}$$

Adding the momentum equations in (2.88) and (2.89), we get the momentum equation for the liquid in the entire U-tube:

$$(L_L\partial_t U_L + L_R\partial_t U_R) = -\frac{p_L - p_R}{\rho} - \left(\frac{F_L}{\rho A_L} + \frac{F_R}{\rho A_R}\right) + (h_L + h_R)g \tag{2.90}$$

where p_0 has been eliminated between the two equations. For incompressible flow, we need to have volumetric flow conservation. This implies that the time rate of change of the volumes is the same on the left hand side and the right hand side of the bend:

$$\begin{aligned} A_L\partial_t U_L &= A_R\partial_t U_R \\ \Rightarrow \partial_t U_R &= \frac{A_L}{A_R}\partial_t U_L \end{aligned} \tag{2.91}$$

Using the above relation to eliminate U_R, we can now write:

$$\begin{aligned} (L_L\partial_t U_L + L_R\frac{A_L}{A_R}\partial U_L) &= -\frac{p_L - p_R}{\rho} - \frac{1}{\rho}\left(\frac{F_L}{A_L} + \frac{F_R}{A_R}\right) + g(h_R - h_L) \\ \partial_t U_L &= -\frac{p_L - p_R}{\rho\left(L_L + L_R\frac{A_L}{A_R}\right)} - \frac{\left(\frac{F_L}{A_L} + \frac{F_R}{A_R}\right)}{\rho\left(L_L + L_R\frac{A_L}{A_R}\right)} + \frac{g(h_R - h_L)}{\left(L_L + L_R\frac{A_L}{A_R}\right)} \end{aligned} \tag{2.92}$$

The second term on the right hand side of equation (2.92) represents the losses due to wall friction. The last term gives the gravitational acceleration according to the height difference in the two legs of the U-tube. This is the same as for the U-tube with a constant inner diameter that was discussed in the previous section. However, the first term on the right hand side is new. In order to find an expression for the unknown pressure change across the coupling, we look at the energy balance:

$$\begin{aligned} \frac{p_L}{\rho} + \frac{1}{2}U_L^2 &= \frac{p_R}{\rho} + \frac{1}{2}U_R^2 + C_{coup} \\ \frac{p_L - p_R}{\rho} &= \frac{1}{2}(U_R^2 - U_L^2) + C_{coup} \end{aligned} \tag{2.93}$$

where C_{coup} is a coefficient denoting the friction losses in the cone-shaped coupling between large and small diameter tubes. This friction coefficient normally depends on the velocity, the diameter of the two tubes, and the angle of the cone. Equation (2.93) can be substituted into equation (2.92), eliminating the unknown pressure difference. In addition, we use the relation $U_L = \partial_t h_L$, and get the final expression for the equation of motion for the liquid interface in the left hand side tube:

$$\partial_t^2 h_L = -\frac{\frac{1}{2}(U_R^2 - U_L^2) + C_{coup}}{\left(L_L + L_R\frac{A_L}{A_R}\right)} - \frac{\left(\frac{F_L}{A_L} + \frac{F_R}{A_R}\right)}{\rho\left(L_L + L_R\frac{A_L}{A_R}\right)} + \frac{g(h_R - h_L)}{\left(L_L + L_R\frac{A_L}{A_R}\right)} \tag{2.94}$$

The only term that is still unknown in equation (2.94) is the coupling loss coefficient C_{coup}. It represents the losses due to the drag from turbulent eddies. These eddies arise from the sudden contraction or expansion of the flowing area. The importance of the eddies varies with the angle of the cone-shaped coupling between the two tubes in Figure 2.11. If the angle between the centerline of the pipe and the edge of the cone is larger than $22.5°$, the coupling can be considered to be abrupt [7]. This means that the friction is the same as if there was no cone, only an abrupt change of diameters.

In the experiment that was done in conjunction with the present work, the angle of the cone exceeded $22.5°$. We therefore use the formula for an abrupt diameter change, so that the simulation will be as similar to the experiment as possible. The friction relations for abrupt changes in pipe diameter are well established by experiments [7]. However, the magnitude of the friction coefficient depends on the direction at which the flow enters the coupling in Figure 2.11. If the liquid is moving from the left to the right, the coupling becomes a reducer. The friction coefficient will therefore be:

$$K_{LR} = \left(1 - \frac{A_R^2}{A_L^2}\right)^2 \tag{2.95}$$

where A_L and A_R are the inner areas in Figure 2.11. If the liquid is moving from the right to the left, the coupling becomes an expander. The friction coefficient is then approximated to be:

$$K_{RL} \approx 0.42 \left(1 - \frac{A_R^2}{A_L^2}\right) \tag{2.96}$$

The two dimensionless friction coefficients in equations (2.95) and (2.96) are related to the coupling friction coefficient in equation (2.94) through the average pipe velocity [7]:

$$\begin{aligned} C_{coup} &= K_{LR} \frac{U_R^2}{2} \\ C_{coup} &= K_{RL} \frac{U_R^2}{2} \end{aligned} \tag{2.97}$$

U_R is used in both terms because the friction coefficients in equations (2.95) and (2.96) are defined from the velocity in the smallest pipe.

2.6 Numerical Solution of the Equations of Motion

There are a lot of numerical schemes that can be used for marching ODEs like the ones in equation (2.79) and (2.94). Some are simpler than others, some are slower than others, and some are more accurate. Choosing an integration scheme is all about getting a satisfying accuracy within a reasonable computational time [28]. What is a satisfying accuracy? As will be shown later, the position of the gas/liquid interface is not changing very rapidly. Hence, there is no point in overdoing the numerical integration. That being said, the case of diameter change is more complex than that of constant diameter. The approaches to the numerical solution will therefore be a little different.

2.6.1 U-tube with a Constant Inner Diameter: Explicit Euler

Equation (2.79) can be solved quite easily by using the velocity and position of the previous time step to solve for the acceleration in each time step. The acceleration is then used to obtain the velocity, which in turn is used to calculate the position. This is an informal way of converting the second order differential equation to a set of first order differential equations. In practice, the routine can be summarized as below:

- Use equation (2.79) to update the acceleration based on the position and velocity at the previous time step
- Update the velocity based on the new acceleration
- Update the position based on the new velocity

This is done for each time step until the maximum time is reached. The simplest and most intuitive way of integrating the above scheme is by using Explicit Euler. It can be derived from a single Taylor expansion:

$$x_{i+1} = x_i + \Delta t \frac{\partial x}{\partial t}\bigg|_{i+1} + \Delta t^2 \frac{\partial^2 x}{\partial t^2}\bigg|_{i+1} + (O^3) \tag{2.98}$$

By neglecting the terms that are of second order and higher, we are left with an equation for the velocity at the next step:

$$v_{i+1} = v_i + \Delta t \frac{\partial v}{\partial t}\bigg|_{i+1} \tag{2.99}$$

where $\frac{\partial v}{\partial t}\big|_{i+1}$ has been calculated by feeding the previous position and velocity into equation (2.79). The new velocity is then used to update the position:

$$x_{i+1} = x_i + \Delta t \frac{\partial x}{\partial t}\bigg|_{i+1} \tag{2.100}$$

Explicit Euler is locally second order accurate but first order globally accurate [28]. The accuracy of this method is, per say, quite bad. However, as long as the time step is not chosen to be too large, Explicit Euler will yield good results for the problem at hand.

Keeping the error at a minimum when stepping equation (2.79) is especially important in the present work. The reason for this is that we want to investigate the influence of friction factors on the damping of the oscillations of the liquid column. If we have momentum leakages due to inaccurate time stepping, it will contribute to the damping. A simple way of making sure that this is not happening is to use the above stepping scheme on equation (2.80) and verify that the amplitude is not decaying with time. This equation is just the equation of motion without any friction. There are thus no damping mechanisms at play, so the amplitude should be constant. This has been done in Figure 2.12. With an initial amplitude $h = h_0$, equation (2.80) is reduced to:

$$h(t) = h_0 \cos\left(\sqrt{\frac{2g}{L}}t\right) \tag{2.101}$$

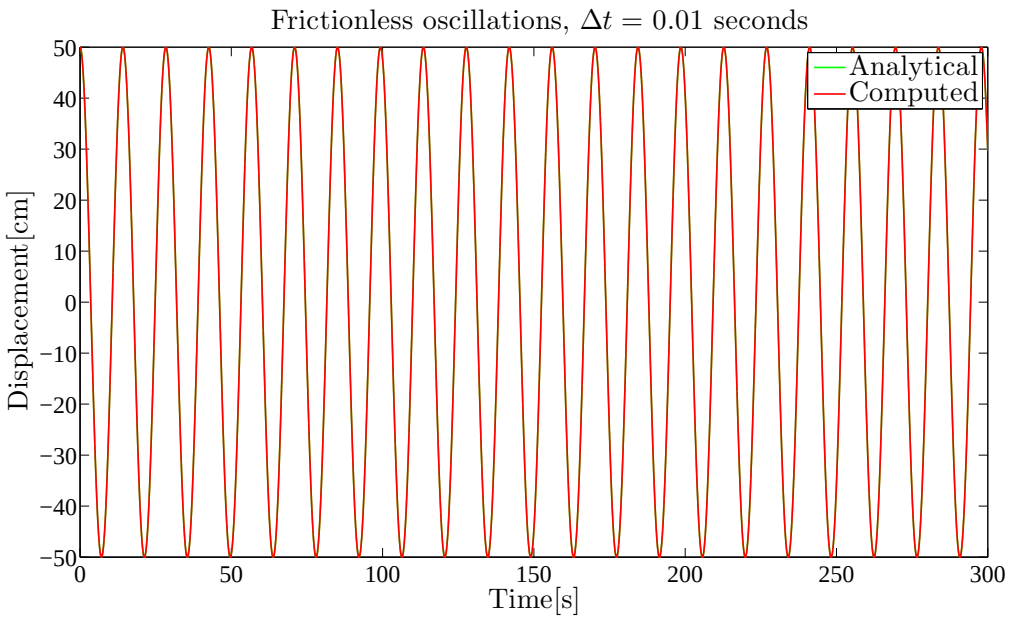

Figure 2.12: A comparison of computatinal and analytical solutions to the equation of motion for a frictionless U-tube with a constant inner diameter. The initial amplitude $h_0 = 50cm$. 300s is much longer than any of the simulations in the coming sections will last. The column length has been chosen to be $L = 100m$, so that we avoid too rapid oscillations. The computed solution coincides with the analytical solution.

We see from Figure 2.12 that there is no visible loss when Explicit Euler is used to step equation (2.101). This means that a time step of 0.01 seconds is sufficient to avoid momentum leakage during the simulations.

2.6.2 U-tube with an Inner Diameter Change: Non-Iterative Error Feedback

Equation (2.94) can be solved numerically in the same manner as outlined in the previous section. The velocity in the new time step, (n+1), is obtained explicitly by using the acceleration and velocity of the previous time step, (n):

$$U_L^{n+1} = U_L^n - \frac{\frac{1}{2}(U_R^n U_R^n - U_L^n U_L^n) + C_{coup}^n - \left(\frac{F_L^n}{\rho A_L} + \frac{F_R^n}{\rho A_R}\right) + g(h_R^n - h_L^n)}{\left(L_L^n + L_R^n \frac{A_L}{A_R}\right)} \Delta t \tag{2.102}$$

To connect the left and right hand side velocities, we equate the volume flow on either side of the coupling. Moreover, since the coupling is located at the bottom of the U-tube, we assume that the difference in liquid length on either side of the tube is equal to the height difference of the interfaces, i.e. $(h_R - h_L)$. The rest of the unknowns can therefore be found through the following computational sequence:

$$\begin{aligned}
1) \quad & U_R^{n+1} = U_R^n + \frac{A_L}{A_R} U_L^{n+1} \\
2) \quad & h_L^{n+1} = h_L^n - U_L^{n+1} \Delta t \\
& h_R^{n+1} = h_R + U_R^{n+1} \Delta t \\
3) \quad & L_L^{n+1} = L_L - h_L^{n+1} \\
& L_R^{n+1} = L_R + h_R^{n+1}
\end{aligned}$$

As equation (2.102) is marched in time, we will have momentum leakages because of the linearization of the non-linear terms in the energy balance. The oscillations will therefore be damped by the numerical error. This is obviously not something that we want when working to find accurate friction relations. To minimize the momentum leakage, one can iterate over the computational steps above within each time step until the momentum error is acceptable.

As an alternative to the iterative approach, equation (2.102) can be solved non-iteratively by feeding a velocity error term from one time step into the next time step. The error term, called ΔU_L, is added to compensate for the fact that we should have used $(U_L^{n+1} = U_L + \Delta U_L)$ in the discretized equation of motion.

We know from the previous section that the error in the linear terms is negligible if the time step is appropriate. We are therefore only interested in the influence of the updated energy term:

$$\begin{aligned}\Delta U_L^{n+1} &= U_L^{n+1}\left(Energy(n+1), Friction(n), Gravity(n)\right) \\ &\quad - U_L^{n+1}\left(Energy(n), Friction(n), Gravity(n)\right)\end{aligned} \tag{2.103}$$

The error obtained in equation (2.103) can now be used as a source term in the calculation of the next velocity, as a compensation for not solving equation (2.102) implicitly in the first place. The velocity in the next iteration is then:

$$U_L^{n+2} = \tag{2.104}$$

$$U_L^{n+1} - \frac{\frac{1}{2}(U_R^{n+1}U_R^{n+1} - U_L^{n+1}U_L^{n+1}) + C_{junc}^{n+1} - \left(\frac{F_L^{n+1}}{\rho A_L} + \frac{F_R^{n+1}}{\rho A_R}\right) + g(h_R^{n+1} - h_L^{n+1})}{\left(L_L^{n+1} + L_R^{n+1}\frac{A_L}{A_R}\right)}\Delta t - \Delta U_L^{n+1} \tag{2.105}$$

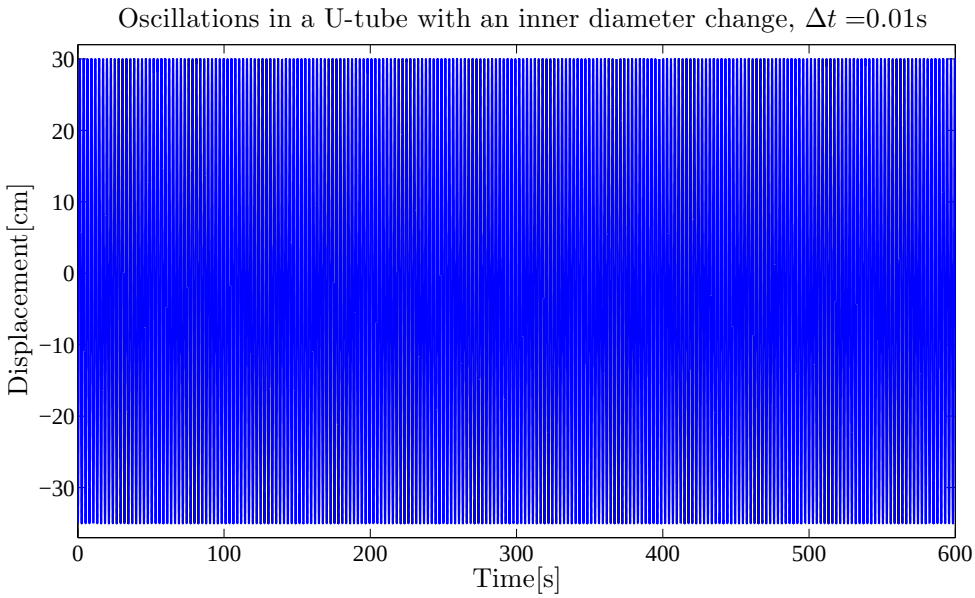

Figure 2.13: The figure shows a 200 seconds simulation of only the gravity term of equation (2.102). The time step is so small that the amplitude does not decay with time.

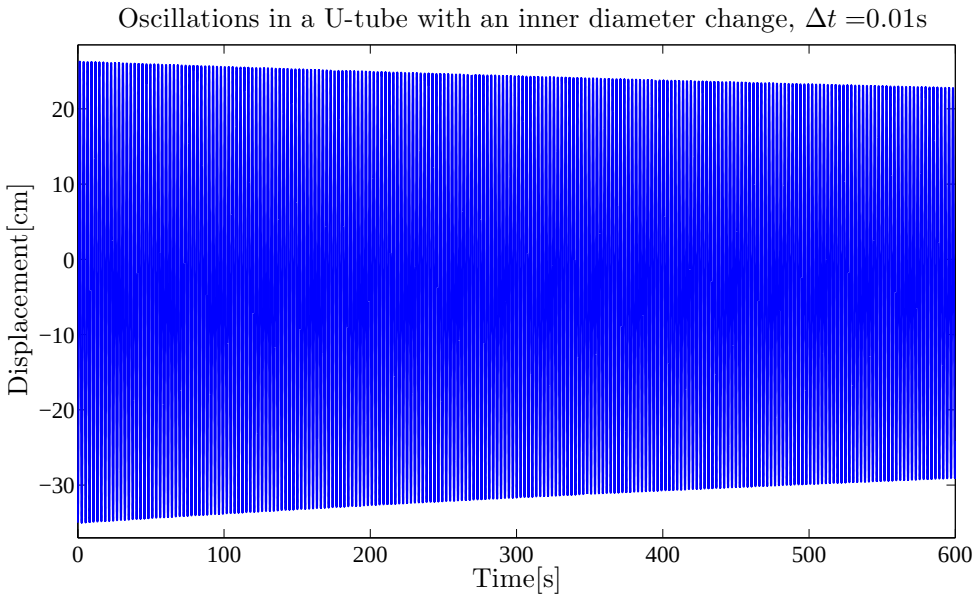

Figure 2.14: The figure shows a 200 seconds simulation of the gravity and energy terms of equation (2.102). The time step is the same as in Figure 2.13, but the momentum leakage from the nonlinear energy term makes the amplitude decay slightly with time.

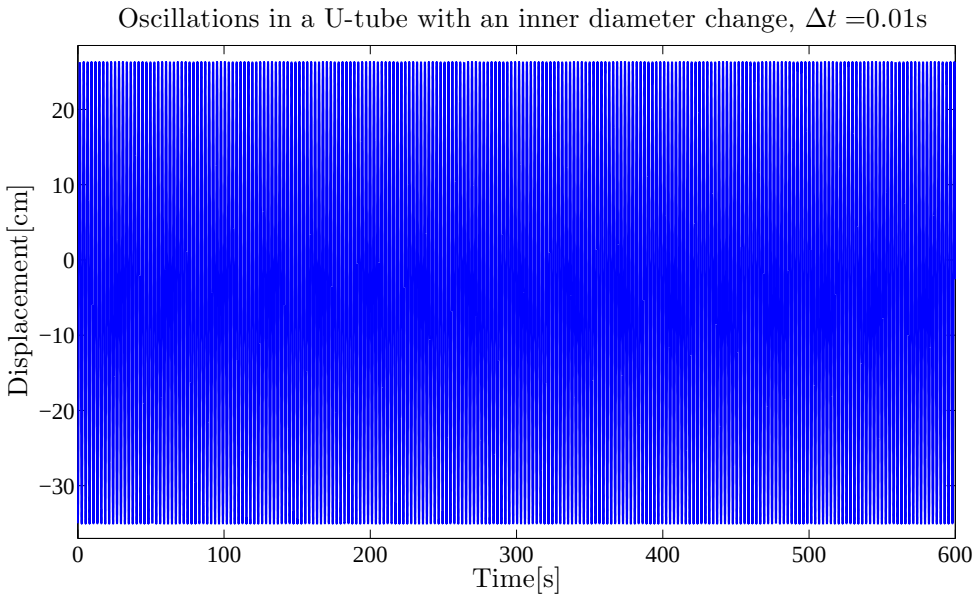

Figure 2.15: The figure shows the exact same simulation as in Figure 2.14, only this time with the feedback of the velocity error from equation (2.103). As a result, the amplitude is kept at a constant level throughout the entire time of simulation.

The effect of the error feedback is shown in Figures 2.13 - 2.15. No friction terms are included in these figures, which means that the amplitude decay in Figure 2.14 is due to momentum leakage from the energy term alone. Figure 2.15 then shows that the momentum leakage has been fixed by using the error feedback technique shown in equation (2.105).

3 Experimental Work

In this section we first look at the experimental work that has previously been done on a U-tube setup. These experiments form the experimental foundation for the computational work in this thesis. After reviewing the previous experimental methods and results we look at the experimental work that has been done in connection with the present work.

3.1 Previous Experimental Work: U-tube with a Constant Inner Diameter

The experimental data that is going to be used to validate the computational results from the friction study in this project is from the work of Simone Knoop [11]. She conducted the experiments in the Multiphase Flow Laboratory at the Norwegian University of Science and Technology. Numerical simulations were also done in connection with the experimental work, in which two steady turbulent friction relations were used.

The experimental setup was comprised of two vertical pipes and a flexible U-shaped pipe section. Two different diameters, two different liquid column lengths, and three initial amplitudes were used in the experiments. Further details of the experimental setup can be found in Table 3.1. The liquids that were used in the experiment were fresh water, Exxcol oil and Marcol oil, their fluid properties can be found in Table 3.2.

To start the experiment, a vacuum pump mounted to one of the vertical pipes was used to pull the liquid column out of the equilibrium position. The initial amplitudes were measured relative to the equilibrium level, see Figure 2.10.

A camera was used to record the movement of the liquid column. The max and min values were then registered by studying the video on a computer. The fact that the experimental measurements have been obtained by studying the results post experiment, suggests that the measurements should be very accurate. The camera had a frame rate of 20fps, which gives a good resolution of the relatively slow liquid movements. Knoop states in her report that the maximum error in time measurement is $\pm$ 0.16 seconds, and that the amplitude measurements are accurate to within $\pm$ 1millimeter.

Later, another group of students repeated parts of the experiments of Knoop in the same laboratory, only with a stiff bend. From now on they will be referred to as Student Group 1, since their report did not have names on it. Their experimental results were very similar to those of Knoop, so they concluded that there is not much difference in using a flexible or stiff bend in the setup. They only used water in their experiments.

Knoop used a very convenient naming system for the different experiments that she conducted [11]. The name of an experiment was comprised of four terms, each describing the conditions under which the experiment had been done. For instance, the name D5-W-S-50 means:

- The pipe diameter was 5cm
- The liquid was water (can also be E or M for Exxsol or Marcol, respectively)
- The short liquid column was used (can also be L, for long)
- The initial amplitude was 50cm

This naming system has been adopted in the present work, and is used to identify all figures in the friction study result section. The constants that have been used in the computational work have been chosen so that they resemble the conditions of the experiments of [11].

Table 3.1: Constants that were used in the U-tube experiments with a constant inner diameter [11].

Parameter	Magnitude
Approximate roughness of pipe [13]	10^{-5}mm
Small pipe diameter	3cm
Large pipe diameter	5cm
Short liquid column length	271cm
Long liquid column length	371cm
Large initial amplitude	100cm
Medium initial amplitude	50cm
Small initial amplitude	10cm
Inner radius of bend	50cm

Table 3.2: Properties of the fluids used in the U-tube experiments with a constant inner diameter [11].

Liquid	Density $\left(\frac{\text{kg}}{\text{m}^3}\right)$	Dynamic Viscosity $\left(\frac{\text{kg}}{\text{ms}}\right)$
Water	997	10^{-3}
Exxcol D80	800	$1.79 \cdot 10^{-3}$
Marcol 52	829-840	$1.1 \cdot 10^{-3}$

3.1.1 Example of Previous Experimental Results

Some of the experimental results of Knoop and Student Group 1 are displayed in the following section in order to give an impression of the time development of the oscillations in the U-tube experiment. Note that only max and min points are given.

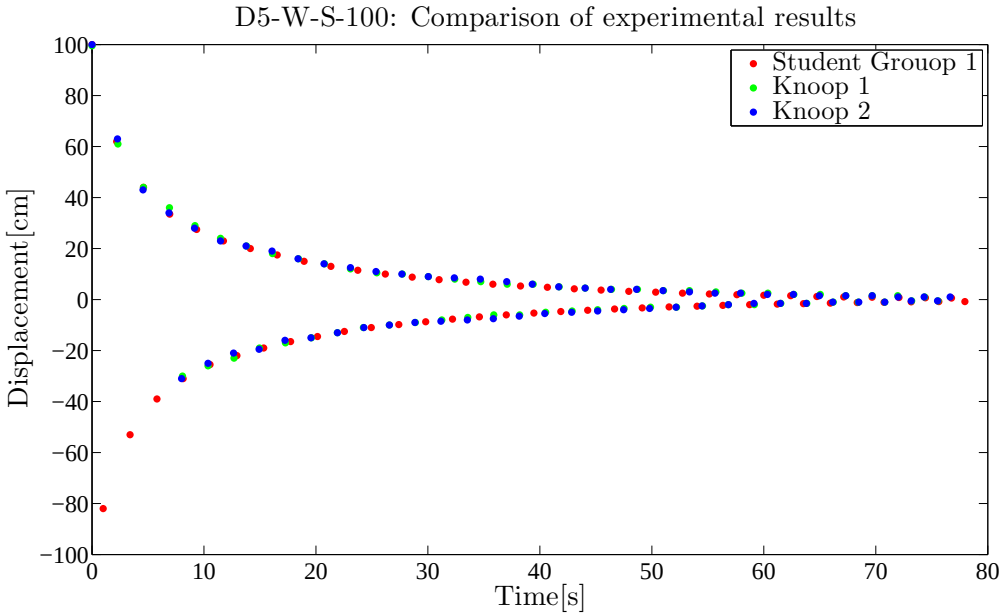

Figure 3.1: A comparison of the experimental measurements that have been done by Knoop and Student Group 1 for a U-tube with a constant inner diameter. Knoop reported that the oscillations stopped completely after about 146 seconds. The observed amplitudes of the different experiments are very similar. The small differences in time measurements could be due to measurement errors.

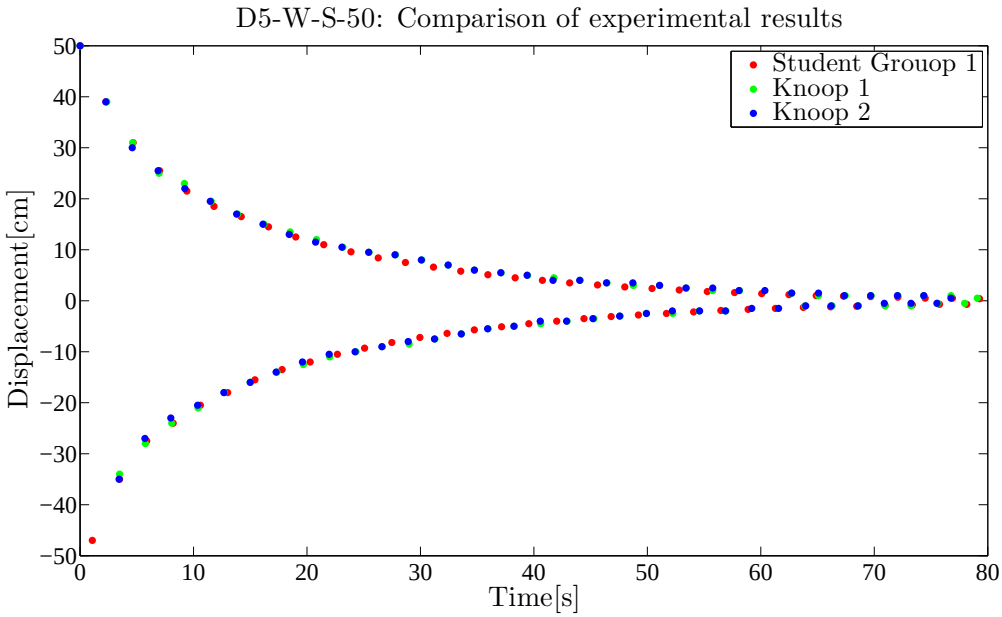

Figure 3.2: A comparison of the experimental measurements that have been done by Knoop and Student Group 1. Knoop reported that the oscillations came to a stop at about 146 seconds, which is the same as for $x_0 = 100cm$. The observed amplitudes of the different experiments are very similar. The small differences in time measurements could be due to measurement errors.

In Figures 3.1 and 3.2 we see that the amplitude measurements of Knoop and Student Group 1 are very similar. The fact that three data series can be so similar indicates that each of the experimental data sets are very accurate. This means that only one experimental series is needed in the following sections whenever a computational result is compared to an experiment. The results of Student Group 1 are therefore not used further in this work. However, they do give more credibility to the results presented in [11].

3.2 Present Experimental Work: U-tube with an Inner Diameter Change

The experimental work on a U-tube with a diameter change will be presented in this section. This kind of setup has an analogy to the industrial case of liquid oscillations between a drill string (small diameter) and an annulus (large diameter) in an oil well [1, 29]. The measurements were done using video recording so that the position of the interface could be continuously tracked by a program made in Matlab. The interface tracking method is inspired by a Master's thesis recently written on the subject of liquid oscillations in an oil well [29].

3.2.1 Description of the Experiment

The experimental work has been done in collaboration with Christian Roeper in the Multiphase Flow Laboratory at the Norwegian University of Science and Technology. The U-tube was comprised of two flexible tubes with inner diameters of 4cm and 6cm. They were joined at the bottom of the bend by a short aluminum cone. The entire rig was mounted on a wall, see Figure 3.3. Both of the tubes had steel wire embedded in them so that they stayed circular.

Water was used in all of the experiments, the volume was held constant at 6.7 liters. In order to make the detection of the interface easier, a green fluorescent powder was added to the water. The left leg of the U-tube had the largest diameter and was permanently mounted to the wall. The right leg could be freely lowered and lifted because it was made from flexible tubing. To change the position of the liquid interface in the left leg, one could therefore just lower the right leg of the tube. To perform an experiment the right leg was thus first lowered until the interface in the left leg was at the desired level. The top of the right leg was then sealed with a rubber glove, lifted to the top position and attached to a beam for stability. The rubber glove was then removed, allowing the liquid to oscillate freely. The size of the rig limited the range of possible initial amplitudes, and the maximum amplitude of the experiments was therefore 50cm.

The measurements were done by filming the movement of the liquid in the left leg of the U-tube. All of the recordings were done with a Canon EOS 70D photo camera. The frame rate of the camera is 25 frames per second, which allows for a very good time resolution of the relatively slow liquid oscillations.

Figure 3.3: The experimental setup for the U-tube with an inner diameter change. The tubes are joined at the bottom; the diameter of the left leg is 6cm while the diameter of the right leg is 4cm. The reinforcing steel wire in the tubes can be seen as the horizontal lines in each of the tubes. The water is colored by a green fluorescent powder. The black cloth was set up behind the left leg to remove any additional light reflections from the wall. The ruler is set up to have a measuring reference for the interface tracking algorithm. The total volume of the water in the pipe was 6.7 liters.

Different light settings were used in the experiments in order to investigate the influence on the tracking program. This was done by switching on and off the lights in the ceiling directly above the rig. In addition, a flash light was tied to a string and dropped into the left leg of the U-tube. This resulted in a very bright light directly on to the liquid interface. A list of all of the initial amplitudes for each of the light settings is given in Table 3.3.

Table 3.3: The initial amplitudes for different light configurations. The abbreviations C and F are used to indicate the light configuration. C = 1, F = 0 means that that the light in the ceiling is on and the flash light is off. Note that the initial amplitudes are not all the same for each experiment.

C=1,F=1 (cm)	C=0,F=1 (cm)	C=1,F=0 (cm)	C=0,F=0 (cm)
11	9	10	11
21	18	20	23
31	30	30	35
40	38	40	45
48	45	53	51
	53		

3.2.2 The Interface Tracking Program

To perform the actual measurement, an interface-tracking algorithm was developed using Matlab. The reason why Matlab was chosen for this task is that it's image processing toolkit contains all the necessary functions for the analysis of the movies. Using these functions, the videos could be split up into individual frames, which then could be treated as three dimensional matrices.

An image is basically a two dimensional matrix of pixels. Each of the pixels have three color components, which Matlab reads individually. These color components are red, green and blue, and they can assume values from 0 to 255. We thus have a three dimensional matrix of color components when working with the images in the program. Exploiting the difference between the color components was the key to tracking the water interface. This task was made easier by the fact that the water had been colored green. When searching for the interface, we are thus looking for pixels that have a green component that dominates the two other components. To avoid random errors, an average over multiple pixels had to be used.

The light setting had a great influence on the intensity of the color components. Because the difference between these components was used to identify the interface, it was necessary to tune the search criteria for each new light configuration. One single image was therefore extracted before the analysis, so that the general intensity of the color components could be registered and put into the program. Moreover, the tube did not cover the entire width of the frames. For that reason, the pixel column that ran down the center of the pipe was also put into the program. This allowed for increased speed when the program searched an image for the liquid interface.

There is a large ruler in Figure 3.3. It was used as an aid when performing the experiment, but it had another important function as well; it could be used to determine the pixel-to-centimeter ratio. The experiments were performed over multiple days, so that the position of the camera would never be the same. Therefore, it was essential for the final results to know the pixel equivalent of one centimeter. The ruler was also used to note the level of the equilibrium before the experiment was started.

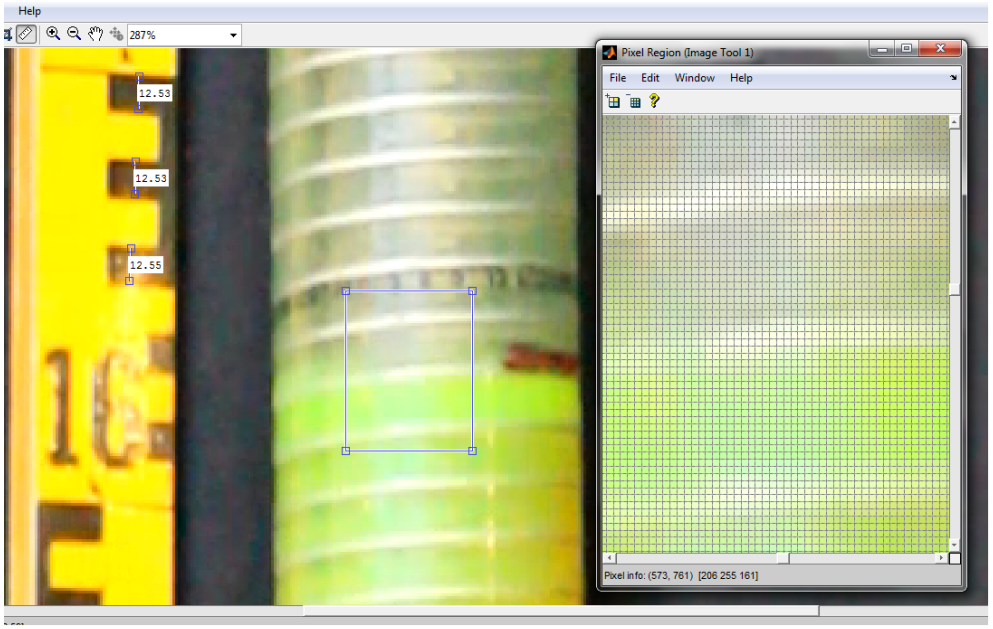

Figure 3.4: The figure shows a snapshot of step one in the image analysis procedure. The Matlab Image Tool was used to find the position of the interface at equilibrium and the column number of the center of the pipe. In addition, the Pixel Region to right was used to analyze the general interface intensities for the present light setting. This was used to set the thresholds in the interface tracking algorithm. The white horizontal stripes in the Pixel Region show the reflected light from the steel wires. The white text boxes to the left show the number of pixels that is needed to cover one centimeter on the ruler.

After the data had been put into the program, the analysis was started. A short pseudo-code of the interface-tracking program is given below and illustrations are made in Figure 3.4.

1. Open one image, note pixel intensities of interface, pipe center pixel column number, pixels/centimeter, equilibrium level
2. Extract an image from the movie and import it as a matrix
3. Iterate over pixel rows, from the top to the bottom (see Figure 3.4)
4. For each row: Iterate over a certain amount of pixels on either side of the pipe center column
5. Calculate the total average intensity of the pixels and the average intensity of the green component
6. If (Average intensity of green) - (Average intensity of white) $>$ Threshold value: $\Rightarrow$ Interface has been located $\rightarrow$ store the row number and break out of loop
7. Repeat steps 2-6 for the entire movie
8. Use pixels/centimeter ratio to convert the stored row values to vertical displacement in centimeters from the equilibrium
9. Plot displacement values

4

Results and Discussion

The results from both computational and experimental work are now going to be presented and discussed. The results from the friction relation study of the constant inner diameter U-tube are presented first. All of the results from this friction study are presented in the same manner. There will be 5 figures with comparisons between computational and experimental data. 8 figures will be displayed for the concluding friction relation in Section 4.5. There will be a short discussion for each model.

After the presentation of the general steady turbulent friction models, there will be a short discussion of some of the flow properties of the U-tube. This is to become more familiar with what the flow in the U-tube looks like.

Next, we look at the experimental results from the U-tube with an inner diameter change. The most promising experimental results will be displayed and discussed. Finally, the results from the simulations of the U-tube with an inner diameter change are presented.

Table 4.1: The set of constant diameter U-tube flow cases which were used for each friction model. The naming system was adopted from the work of Knoop, and each figure will be marked with one of the codes from the column to the left.

Abbreviation	Pipe Diameter [cm]	Liquid	Column Length short/long	Initial Amplitude [cm]
D5-W-S-100	5	Water	Short	100
D5-W-S-50	5	Water	Short	50
D3-W-S-50	3	Water	Short	50
D5-W-L-50	5	Water	Long	50
D5-M-S-50	5	Marcol	Short	50

The quite extensive experimental work done by Simone Knoop [11] leaves the opportunity to verify the computational results for a lot of different parameters in the constant diameter U-tube. However, displaying comparisons of computational and experimental results for all the available variations would just be chaotic and confusing. A selection of the experimental data has therefore been chosen as a test basis for all the friction models in Sections 2.1.6 - 2.4. They have been chosen so that the testing will involve variations in initial amplitude, viscosity, density, pipe diameter and liquid column length. The experimental test set is presented in Table 4.1. Even though only these results are displayed, other scenarios have been tested as well.

4.1 Steady Turbulent Friction Relations

The results of four of the traditional expressions for steady turbulence are presented and discussed in this section. A brief theoretical description can be found in Section 2.1.6. As it is known that these expressions do not provide a sufficient amount of damping, the purpose of this section is rather to decide which of the expressions that is best suited for the U-tube flowing case. Also, potential problem areas can be identified so that they can be addressed in later models.

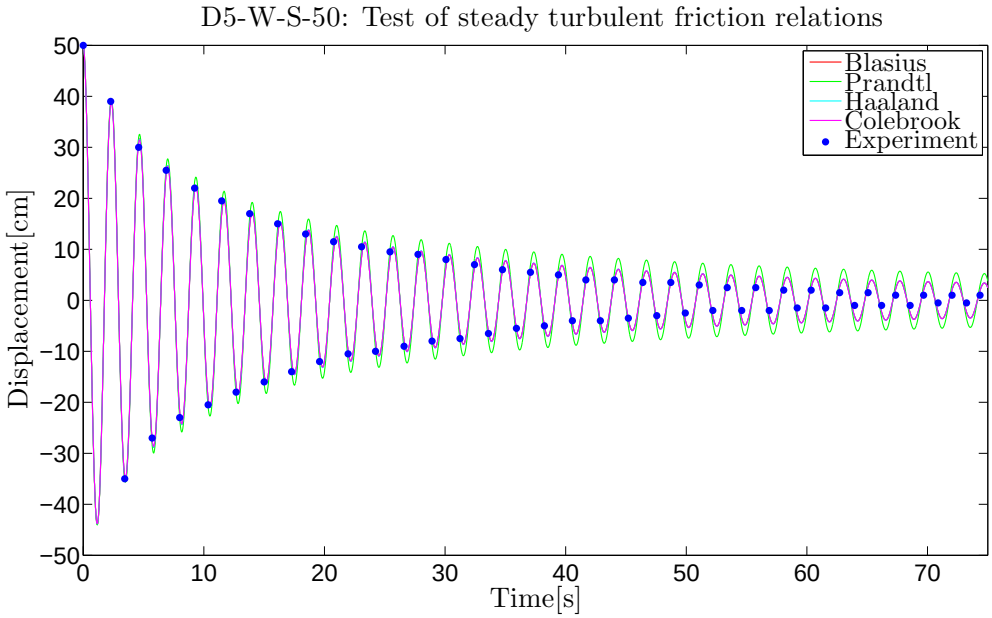

Figure 4.1: The figure shows a comparison of the performance of the steady turbulent friction relations in equations (2.37) - (2.41). The curves of Blasius, Haaland and Colebrook coincide, while the curve of Prandtl has the largest fluctuations. The experimental data points are from [11].

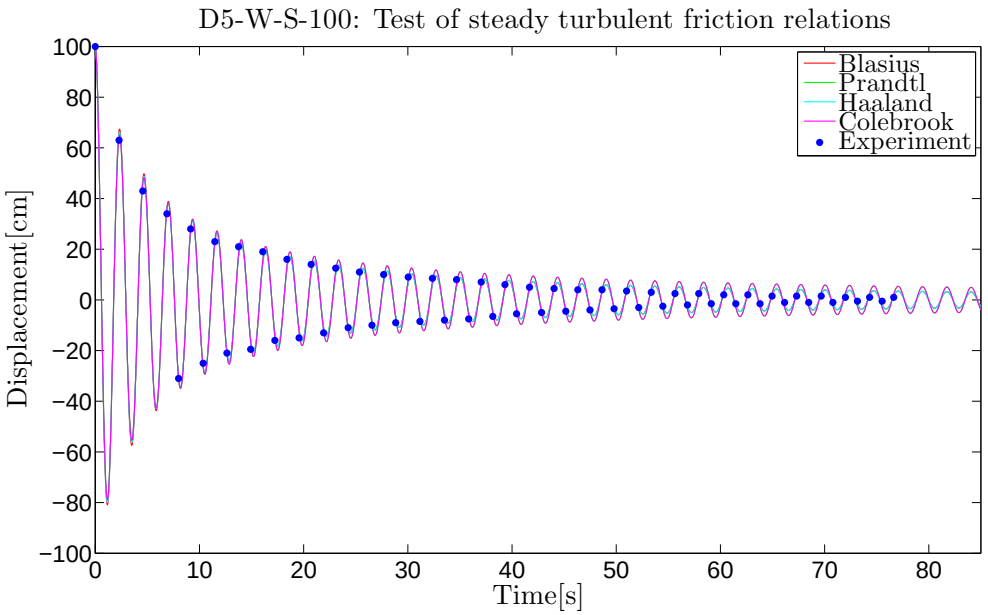

Figure 4.2: The figure shows the same models as in Figure 4.1, with a larger initial amplitude. The curves of Blasius, Prandtl and Haaland overlap most of the time, while the curve of Colebrook has larger fluctuations.

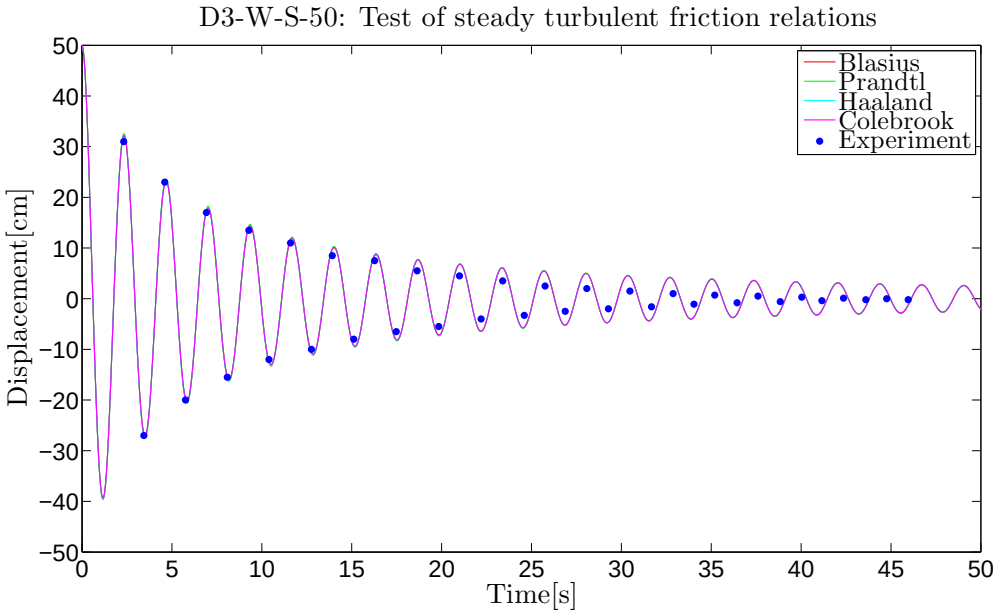

Figure 4.3: The figure shows the same models as in Figure 4.1, with a reduced pipe diameter. The curves overlap for small amplitudes, Prandtl has slightly larger fluctuations in the beginning.

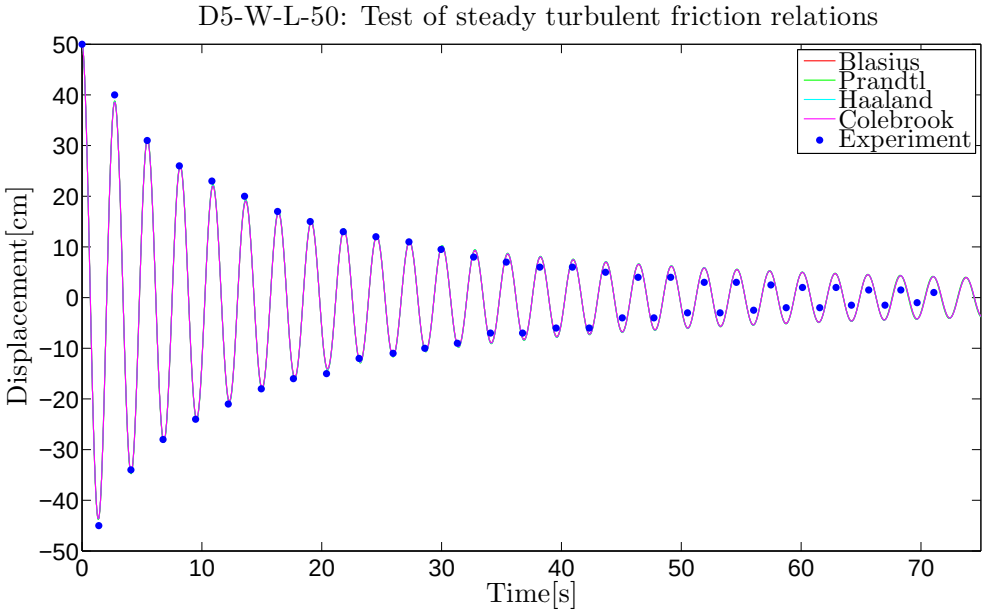

Figure 4.4: The figure shows the same models as in Figure 4.1, with a longer liquid column. All of the curves coincide.

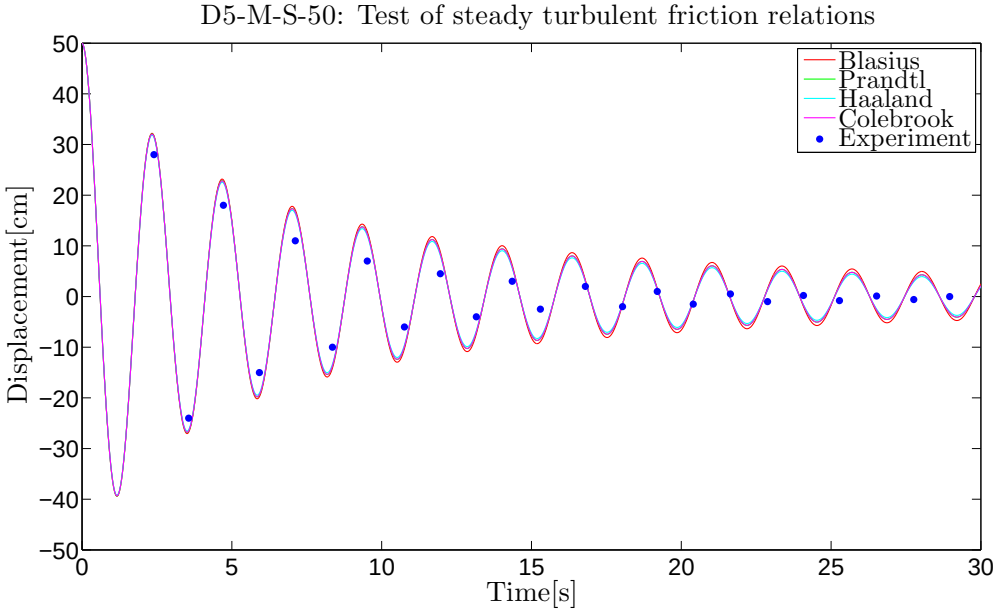

Figure 4.5: The figure shows the same models as in Figure 4.1, with a more viscous liquid. Blasius has the largest fluctuations, and Haaland has the smallest. Colebrook and Prandtl overlap, and their fluctuations lie between those of Haaland and Blasius. The predicted period does not comply very well with that of the experiments.

In Figure 4.2, all of the friction relations except for Prandtl yield the same results. Figure 4.1 shows that the Colebrook relation may be sensitive to large initial amplitudes. All of the other models yield the same results. The pipe diameter does not seem to make any difference for any of the friction relations in Figure 4.3, and neither does the column length in Figure 4.4. In Figure 4.5 we see that none of the relations stand out significantly. Blasius is the one that is farthest away from the experiments, while Haaland is marginally better than Prandtl and Colebrook.

From these observations, we see that the implicit expressions are no better than the explicit expressions, at least with an iterative solution for λ. On the contrary, both Colebrook and Prandtl have one quite large discrepancy each. Hence, there is no reason for going through the extra work of using one of the implicit expressions in the rest of the present work. Haaland gives slightly better results than Blasius in the case of high viscosity. However, the Haaland expression implies division by zero whenever the velocity goes to zero. It is therefore a lot less stable than Blasius, which does not imply any division by the velocity. Blasius will therefore be used to represent steady turbulent friction in the rest of the present work.

Looking at the computational results as a whole, there are some important observations to point out. In Figures 4.1 - 4.4 we see that the computational and experimental results are very consistent during the first 20 seconds. The reason for this is that the steady turbulent friction relations are best suited for high Reynolds number flows. This is because the friction term in the equation of motion (2.79) is velocity dependent. The fact that we have a much more effective damping for large velocities can also be seen by comparing Figures 4.1 and 4.2. It does not take long before their amplitudes are approximately the same magnitude.

Another important observation is that the steady friction relations clearly suffer from the strong velocity dependence once the flow slows down. When the oscillations become small, the velocity also becomes small. Hence, the velocity dependent damping term of equation (2.79) nearly vanishes. We are thus left with a simulation that is almost like the undamped harmonic oscillator, while the amplitude of the liquid column in the experiments continues towards zero. This is the key problem with using the steady friction relations in U-tube simulations. Solving this problem will therefore be the main focus in the following sections.

4.2 Investigation of the Flow Properties in the U-tube

Having seen the results of the steady turbulent friction relations, we have an idea of what the oscillating flow in the U-tube looks like. Now is therefore a good opportunity to have a closer look at some of the general properties of the flow. We first look at the Reynolds number as a function of time for a couple of typical flow situations. After that, we take a closer look at how the velocity and acceleration behave during the course of a simulation. The oscillation period is then investigated, before we finally take a look at the turning of the liquid column. The results of this section can hopefully help in the analysis and understanding of the rest of the friction model results.

4.2.1 The Reynolds Number and Flow Regimes

Even though the computational results from Section 4.1 were not sufficiently accurate, they can still provide us with an overview of the range of Reynolds numbers that we are dealing with. This can be useful on later occasions, as the Reynolds number is used to define the limits for laminar and turbulent flow.

Two simulations were done, for two different flow cases. One case had higher velocities and lower viscosity than the other. The Reynolds number was calculated for each time step using the computed velocity. Figures 4.6 and 4.7 show the resulting plots of the Reynolds number as a function of time.

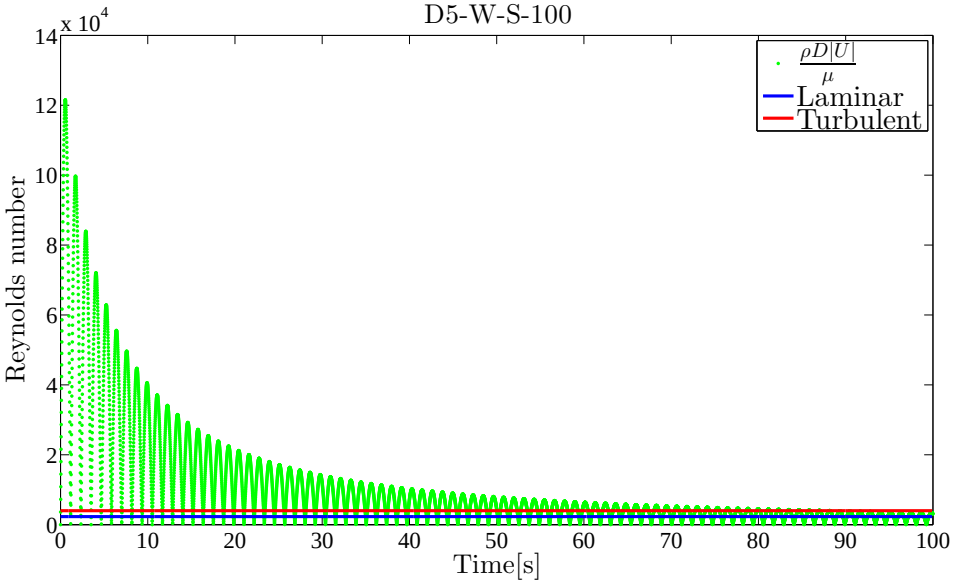

Figure 4.6: The figure shows the Reynolds number resulting from a simulation of the U-tube with a constant inner diameter. Blasius was used as the friction relation. This simulation illustrates one of the flow cases with the highest Reynolds number, because the liquid has a low viscosity and the initial amplitude is large. One green dot is plotted for each time step. The horizontal lines denote the laminar and turbulent Reynolds number limits given in equation (2.12).

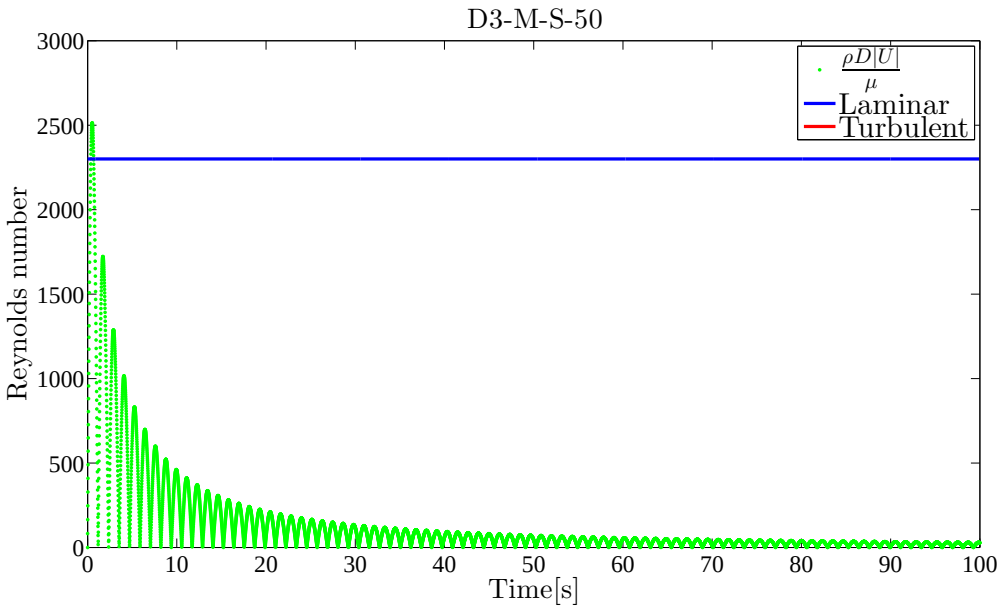

Figure 4.7: The same as in Figure 4.6, only for a liquid with a higher viscosity. This simulation illustrates one of the flow cases with the lowest Reynolds number, because the liquid has a high viscosity and the initial amplitude is medium high. One green dot is plotted for each time step. The horizontal lines denote the laminar and turbulent Reynolds number limits given in equation (2.12).

We can see from Figures 4.1 and 4.2 that the simulations are accurate for the largest amplitudes. Therefore, we know that the prediction of the maximum Reynolds number in each figure is quite accurate. After some time has passed, we know that the simulations predict a velocity that is too high, which results in a Reynolds number that is too large.

In the upper plot of Figure 4.6 we see that the maximum Reynolds number is about $1.2{\cdot}10^5$, while the maximum of the lower plot is about 2500. This means that the flow of Marcol in the smallest pipe for a medium initial amplitude is almost exclusively in the laminar region. The flow of water in the largest pipe with the largest initial amplitude is on the other hand turbulent for the majority of the time.

Even though the flow of Marcol is mainly laminar, the flow is still not steady. Because the flow changes directions with every oscillation, the liquid column is constantly accelerating or decelerating. The flow is thus unsteady and laminar. Likewise, the flow of water with large diameter and initial amplitude is also unsteady. Even though we have time steps in the laminar regime, the flow is probably still turbulent. This is because the dissipation of the turbulent eddies takes time [10]. By the time most of the turbulence has been broken down, the flow has turned and entered into the turbulent regime yet again. On the other hand, when the amplitude becomes small, the flow will mainly stay in the laminar region.

4.2.2 Velocity and Acceleration

In this subsection we look at the development of the position, velocity and acceleration during a simulation of a typical mid-range Reynolds number flow case. By doing this, we can see how they behave relative to each other and learn more about the movement of the liquid column. We also look at the two different components of the acceleration to see the size relation between them.

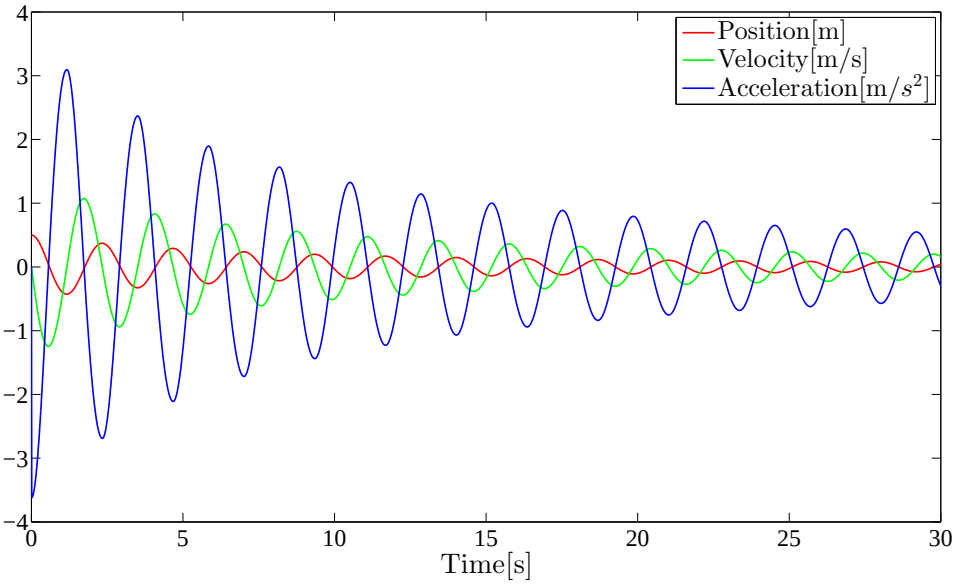

Figure 4.8: The position, velocity and acceleration of the liquid column for the following simulation case: D5-E-S-50. The acceleration has a positive maximum whenever the position has a negative maximum. The velocity has a maximum when the position is zero.

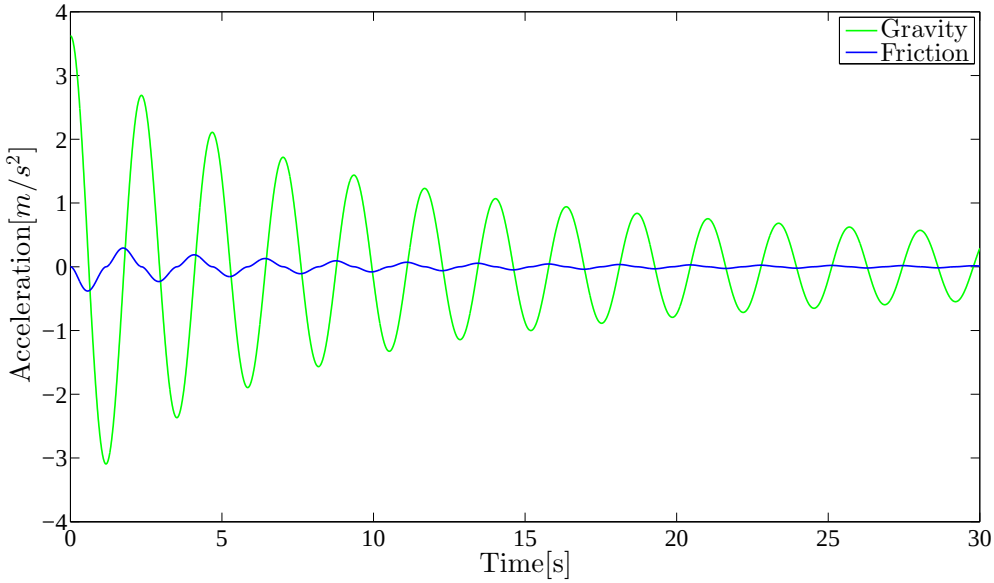

Figure 4.9: The figure shows the two components of the acceleration when Blasius is used as the friction relation. From equation (2.79) we know that the gravity component scales with the position of the liquid column, and the friction component scales with the velocity.

In Figure 4.8 we see that the zeros of the position and acceleration will always coincide. The opposite signs can be explained by looking at their relation in equation (2.79). In Figure 4.9 we see that the total acceleration is comprised of two components; gravity and friction component. The gravity component has the same period as the total acceleration while the friction has the same period as the velocity. Gravity dominates the friction from start to finish. After about 20 seconds the friction component of the acceleration is almost zero. This explains the earlier observations of the poor compliance between experiment and simulation after 20 seconds in Figures 4.1 - 4.4. This is one of the problems that has to be addressed in future friction models.

We see from Figure 4.8 that friction relations that are dependent on the acceleration will have a maximum whenever the liquid is turning. If the process of turning indeed involves extra friction, we see from the figure that an acceleration based friction model could yield very good results.

4.2.3 Oscillation Period

The oscillation period of the experiments and the simulations are further investigated in this section. There are two reasons for this. First, we can see if the damping term in equation (2.79) has any effect on the period. In theory it has an effect, but is it even visible? Secondly, we compare the oscillation period of the experiments to the analytically derived period of equation (2.81). This will show whether or not the real life data follow the theoretical frictionless period.

In Figure 4.10 the periods have been plotted for four of the cases from the section on steady friction models. These four cases have the same column length, so that the theoretical frictionless period is the same for all of them.

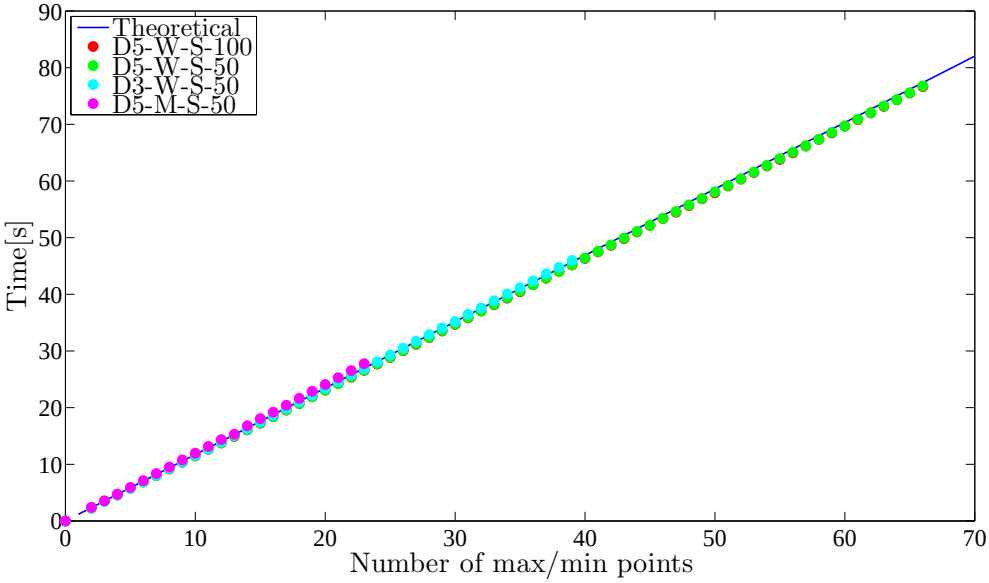

Figure 4.10: The dots show the time at which the experimentally measured amplitude of the liquid column has a maximum or a minimum. The figure thus displays the half period as a function of time. The blue line shows the theoretical frictionless half period as a function of time, $T/2(t) = \frac{\pi}{2}\sqrt{\frac{2L}{g}} * t$, where L = 2.71m and g = 9.81. The red and green dots completely overlap, and they are a little below the theoretical line towards the end. The cyan dots are following the theoretical line, while the magenta dots end up a little above the theoretical line.

Because the data series used in Figure 4.10 have been manually measured, the observed deviations could be due to measurement errors. However, if this was the case, we would expect to see a zig-zag pattern in the points. Instead, all the plots exhibit very consistent trends as the velocity decreases.

The period increases a little for the viscous Marcol oil, while it decreases for the water with a diameter of 5cm. It remains constant for the water experiment with a diameter of 3cm. This indicates that the speed of the liquid indeed has an influence on the oscillation period of the experiments. Put more precisely: The very viscous Marcol oil has a longer oscillation period because it prevents the liquid column from accelerating as fast as a column of water does.

Moreover, all of the lines are almost perfectly linear. This means that there is no significant increase in the oscillation period when the amplitude becomes small. The reason why there are visible discrepancies towards the end of each series is because the small time errors accumulate. Hence, there is no evidence of significant changes in the last part, compared to the first part of the series.

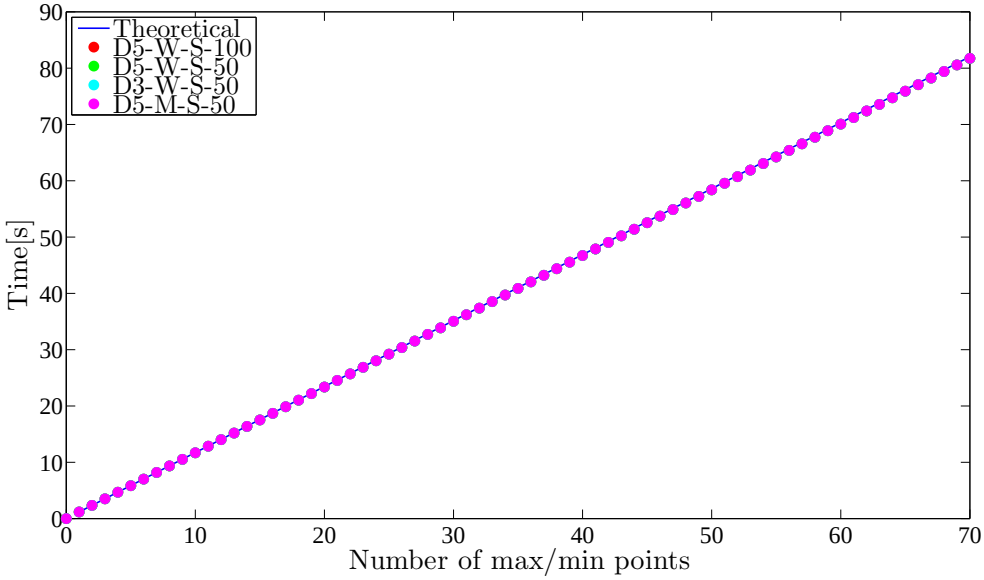

Figure 4.11: The figure shows the same half period plots as in Figure 4.10, only this time for simulations with Blasius' friction factor. All of the dots overlap and they are marginally below the theoretical half period line at the end of the plot.

In Figure 4.11 we see that there is no period difference between the simulation cases. This means that the simulations with steady friction relations do not catch the small deviations in oscillation periods that we have seen in Figure 4.10. In fact, this is quite obvious when we look at Figures 4.1 - 4.5, and see that the period of the simulations do not match those of the experiments. In Figure 4.10, Marcol displays the largest period deviation, which is also confirmed by Figure 4.5. The period of Marcol in Figure 4.11 does not differ from any of the other simulations.

The reason why the simulation results are all a little below the theoretical line in Figure 4.11 is that the velocity does have a small influence on the oscillation period. However, the difference is negligibly small.

4.2.4 Turning

The process of turning could involve extra friction for the oscillating flow in the U-tube. To further investigate if this was the case, the curve shape of the position was plotted at the time of turning in Figure 4.12.

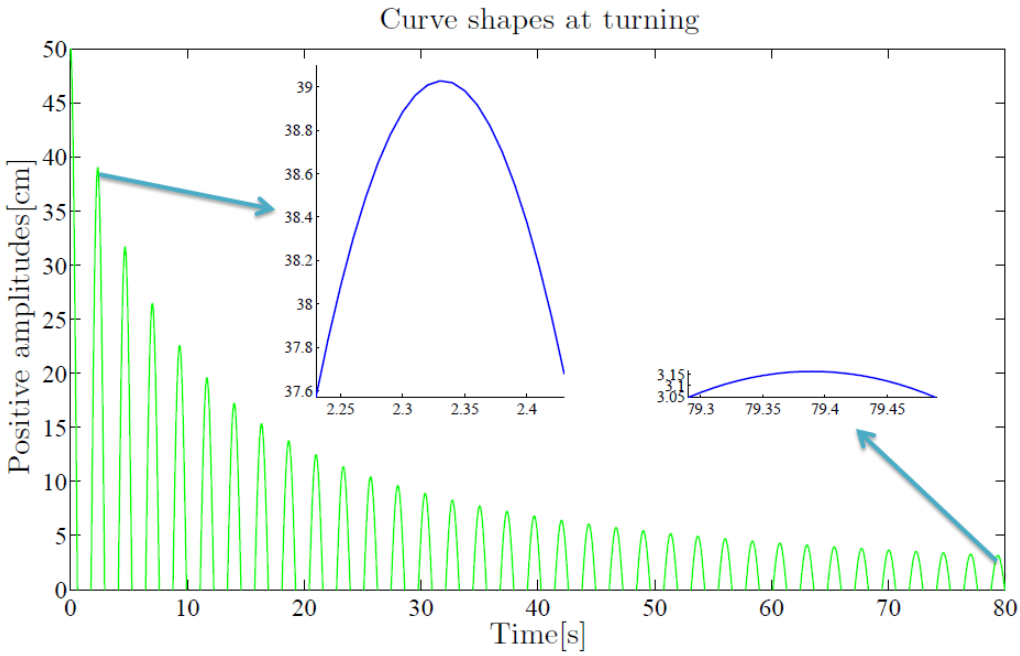

Figure 4.12: A figure illustrating the change in the position of the liquid column at two different maxima, t = 2.33s and t = 79.39s. The arrows indicate which maxima that have been enhanced. A time interval of 0.2 seconds has been used in both of the small plots and the scale of the axes is true to the amplitude difference. The simulation was done with the Blasius friction coefficient.

The difference between the two close-up maxima in Figure 4.12 illustrates an important point in the discussion of the effect of turning. Because the period is close to constant, the position changes more slowly when the amplitude is small. This implies that more of the time is spent on the process of turning. If the turning involves extra friction, it is thus more important at small amplitudes than at large amplitudes. This could be an additional reason why the steady friction models do not match the experiments after some time has passed. During the time of turning, the velocity is very low, which implies that the steady friction relations die off. If turning indeed implies more damping than in regular flow, a friction relation with a different velocity dependence is needed. An acceleration dependent friction term, such as suggested in equation (2.50), may be the way to go.

4.3 U-tube-Specific Steady Friction Relations

The results from two models that are especially designed for oscillating flow in the U-tube are presented and discussed in this section. In addition, the friction from flow in a bend is investigated.

4.3.1 Flow in a Bend

In order to investigate if the bend of the U-tube can contribute significantly to the damping of the U-tube-oscillations, the results from Idelchik's friction model in Section 2.2.1 are presented and discussed below.

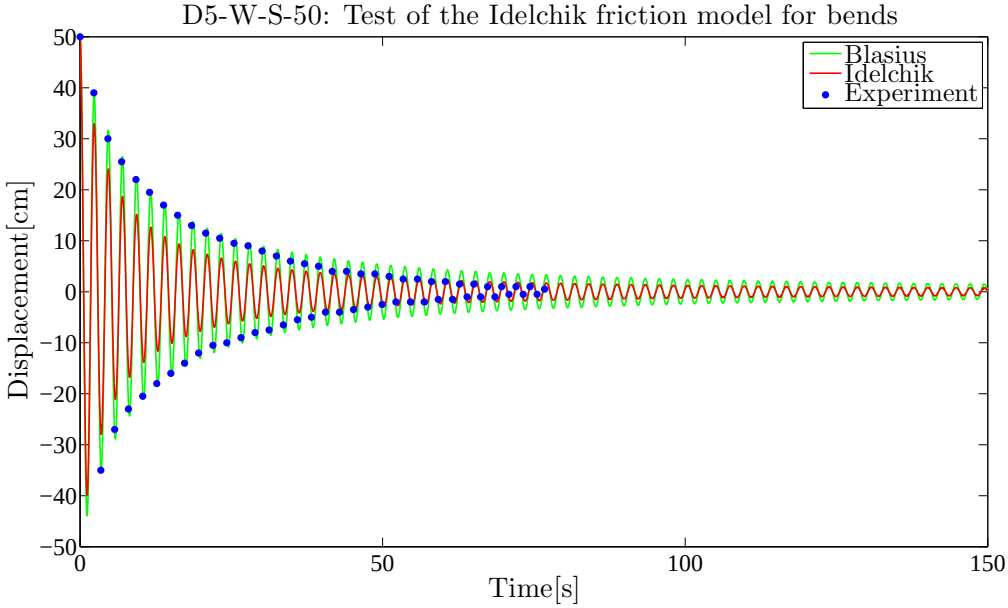

Figure 4.13: The figure shows a comparison of Idelchik's friction model from equation (2.42) and Blasius's turbulent friction relation. It is clear that Idelchik's model provides much more damping than the friction from Blasius. A long time period has been used to show that the liquid does not come to rest. The experimental data are from [11].

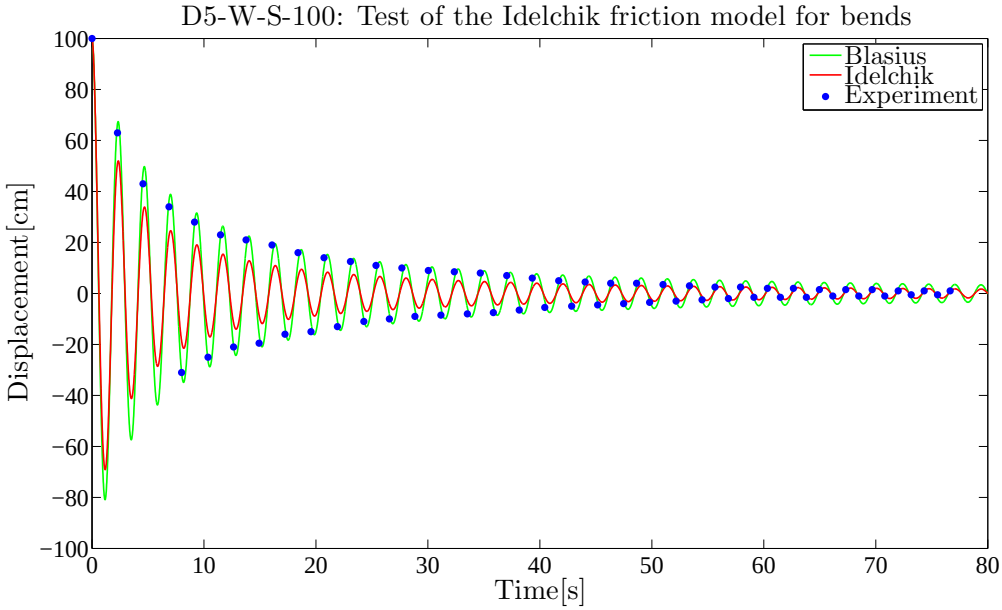

Figure 4.14: The figure shows the same models as in Figure 4.13, with a larger initial amplitude. Idelchik's model provides more damping than Blasius at all times of the simulation.

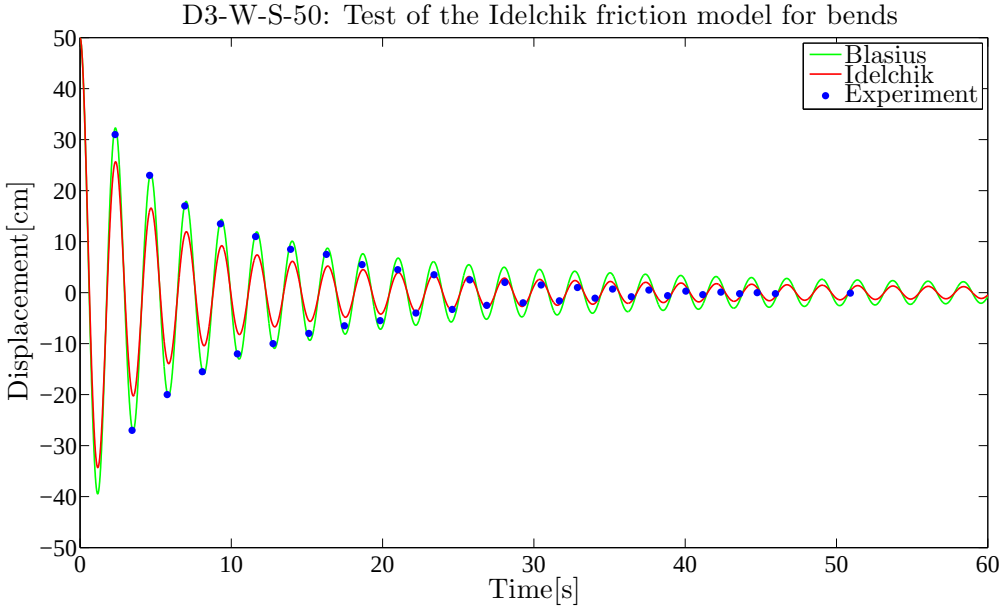

Figure 4.15: The figure shows the same models as in Figure 4.13, with a smaller pipe diameter. Idelchik's model provides more damping than Blasius at all times of the simulation.

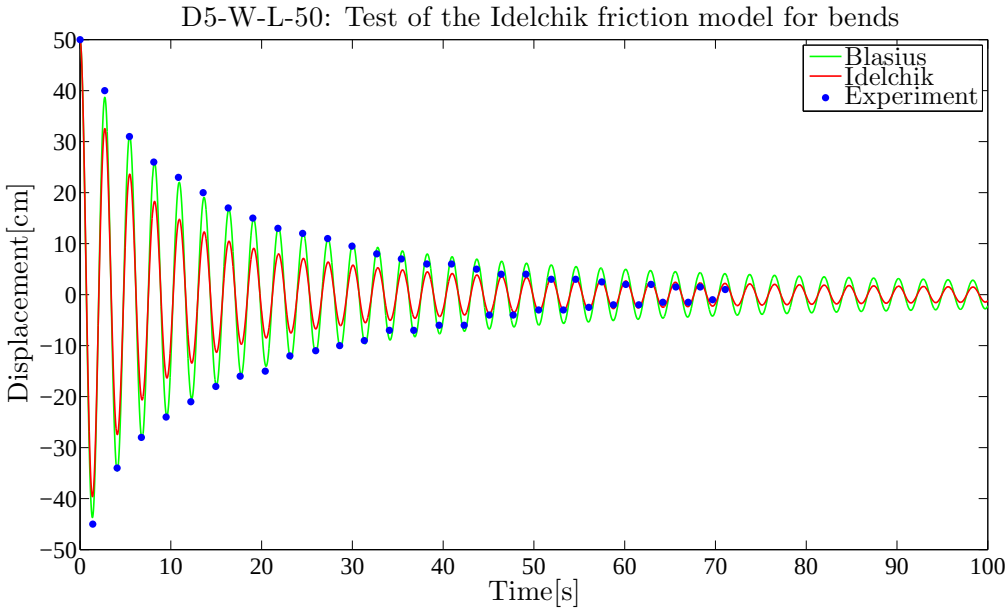

Figure 4.16: The figure shows the same models as in Figure 4.13, with a longer liquid column. This causes the frequency of the oscillations to increase. Idelchik's model provides more damping than Blasius at all times of the simulation.

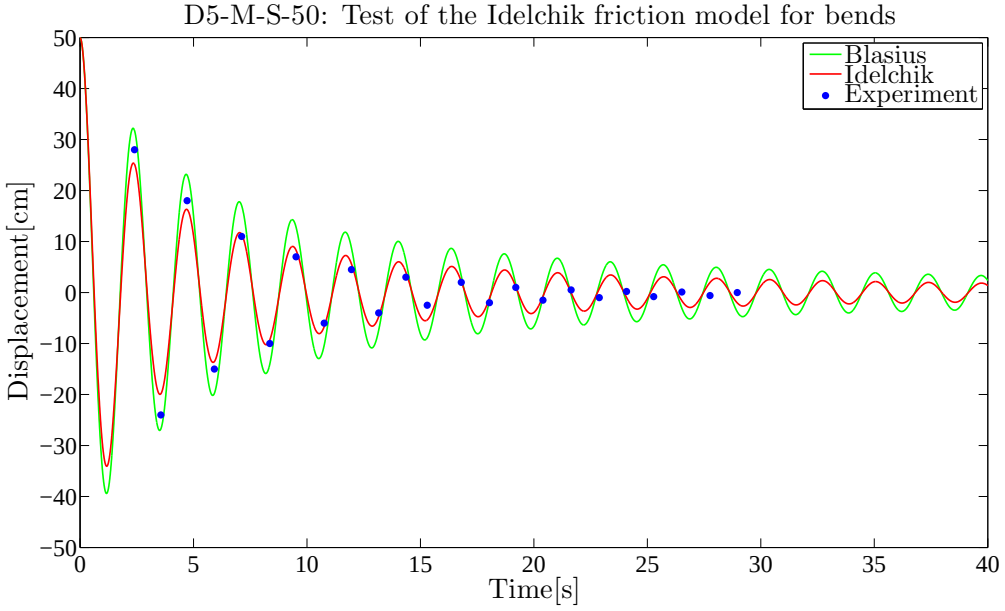

Figure 4.17: The figure shows the same models as in Figure 4.13, with a higher viscosity. Idelchik's model provides more damping than Blasius at all times of the simulation. Even though it is closer to the experimental data this time, Idelchik's model does not bring the liquid to rest. Also, the predicted period does not comply very well with that of the experiments.

In Figure 4.14 we see that the additional friction from the bend in Idelchik's method indeed reduces the amplitude of the oscillations. This is generally the case in all of the simulations. However, the damping is too strong in the beginning of the simulations. After a while, the damping is not sufficient anymore, and the amplitude predicted by the simulations is too large.

It is clear that Idelchik's method suffers from the same problems that we see in the steady friction relations. Because it is multiplied with the velocity, the friction contribution dies off as the velocity becomes small. As we can see in Figure 4.13, the amplitude barely decreases after 100 seconds. This is because the damping term has almost completely disappeared.

We already know that oscillating flow in a U-tube does not meet all the requirements for Idelchik's method with respect to fully developed turbulence. However, the indications that we have from Figures 4.13 - 4.17 are enough to conclude that a bend friction relation is not what we are looking for. The oscillations do not come to a stop, and the damping is too strong during the first seconds.

4.3.2 Ogawa's Method for Oscillating Flow in a U-tube

The results from using Ogawa's friction model in Section 2.2.2 are displayed and discussed in this section. This friction relation has already been used in a Master's thesis on oscillating flow in hydroelectric power plants [3].

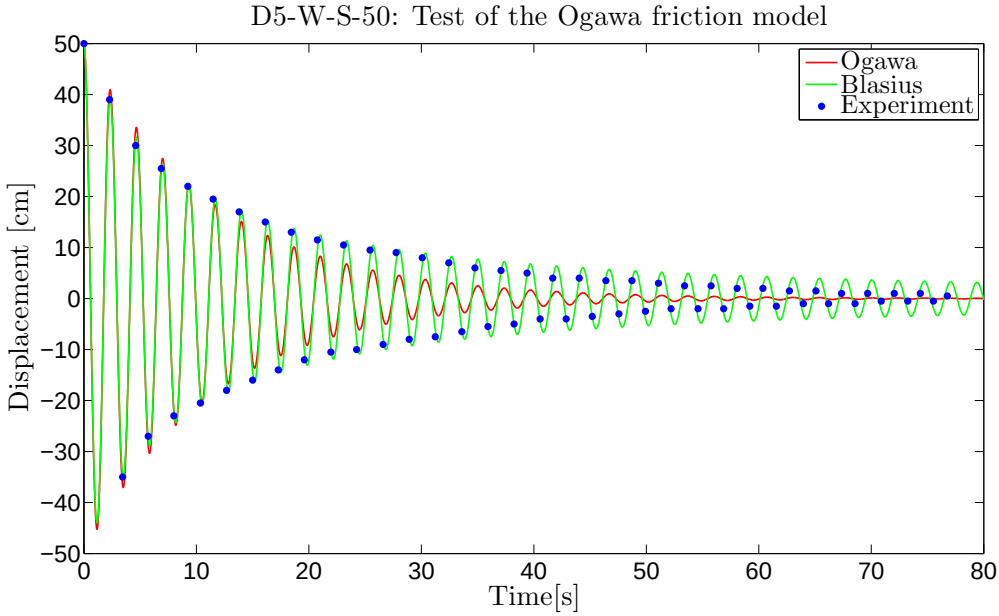

Figure 4.18: The figure shows the results of Ogawa's friction model from equation (2.46). It is compared to Blasius's friction relation and experimental results from [11]. The new model results in too much damping compared to the experiments. It brings the liquid to rest after about 80 seconds.

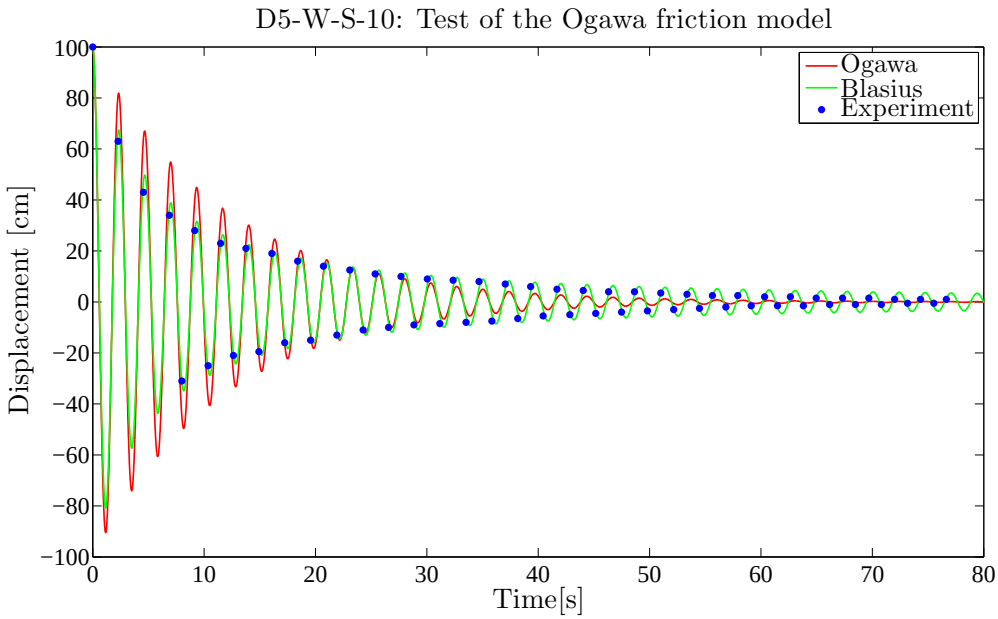

Figure 4.19: The figure shows the same models as in Figure 4.18, with a larger initial amplitude. The large amplitude makes the friction model of Ogawa overestimate the amplitude during the first 20 seconds. After that, it underestimates the amplitude.

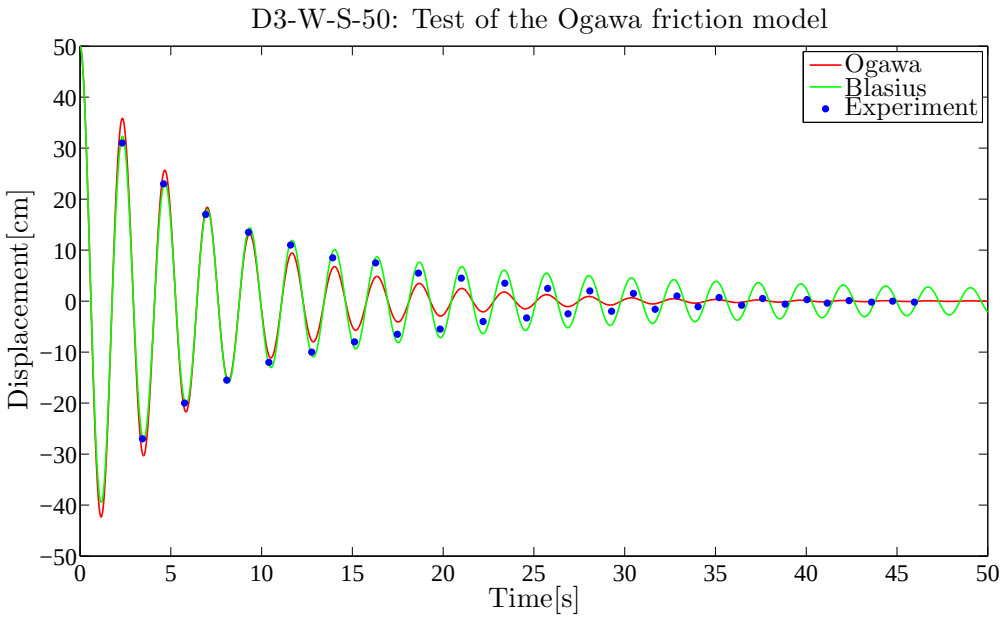

Figure 4.20: The figure shows the same models as in Figure 4.18, with a smaller pipe diameter. The reduced velocity of the liquid makes Ogawa's model yield better results than in Figures 4.18 and 4.19.

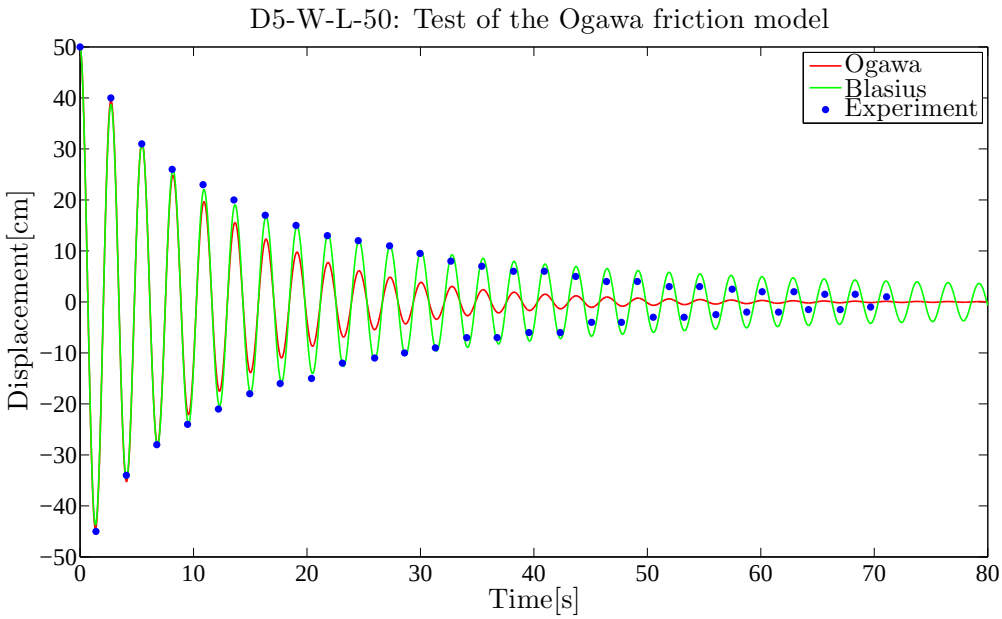

Figure 4.21: The figure shows the same models as in Figure 4.18, with a longer liquid column. The performance of Ogawa's model is worse than that of the simple steady turbulent friction of Blasius as it quickly underestimates the oscillation amplitude.

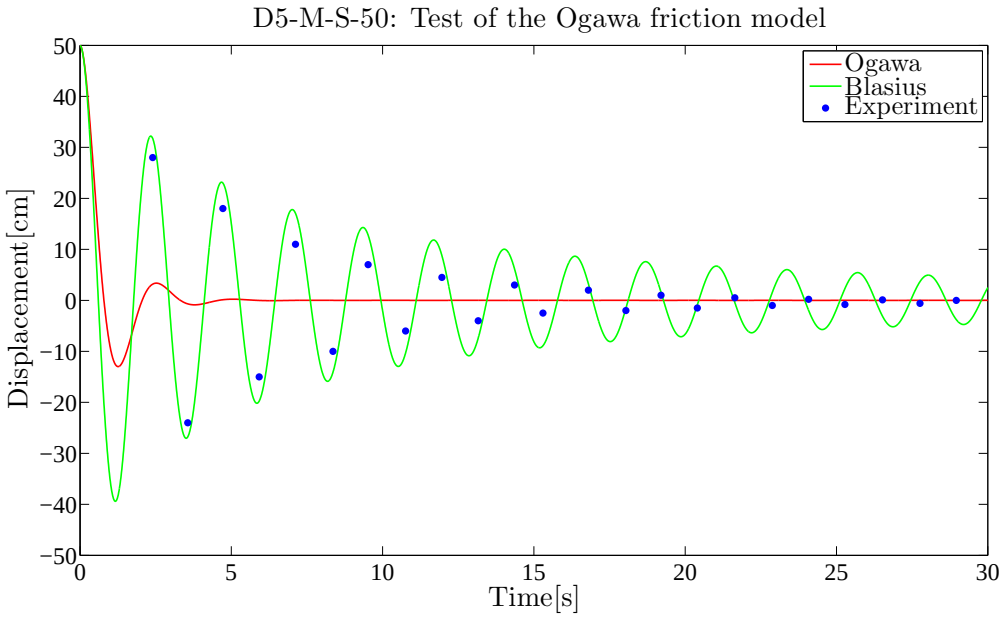

Figure 4.22: The figure shows the same models as in Figure 4.18, with a more viscous liquid. The computed friction of Ogawa's model is too high.

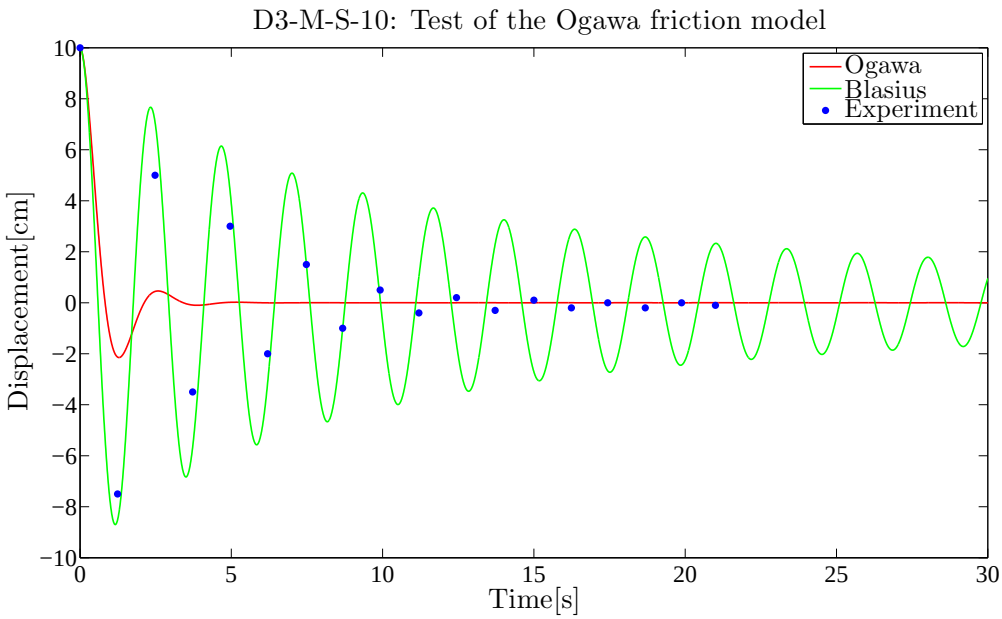

Figure 4.23: The figure shows the same models as in Figure 4.18, with a smaller initial amplitude. This extra figure has been added to look at the performance of Ogawa's model for low Reynolds numbers. The result is still too much damping. The predicted period does not comply very well with that of the experiments.

As was reported in [3], the Ogawa friction relation has a tendency of yielding too little damping during the first seconds and then yield too much damping for the rest of the time. When comparing Figure 4.19 to Figure 4.18, it seems like the Ogawa relation is not so well suited for larger initial amplitudes. This is probably because the model was made with small Reynolds numbers in mind. As pointed out earlier, the friction model has the same velocity dependence as the laminar friction factor. This makes it highly effective for low Reynolds numbers, but not as effective for high Reynolds numbers. In Figure 4.20, we see that the results are quite good when the pipe diameter is smaller. This further suggests that the Ogawa relation is better suited for small Reynolds numbers, with small pipe diameters and small initial amplitudes.

When the column length is increased in Figure 4.21, the damping is of appropriate magnitude during the first seconds. This is because the friction term is dependent on the liquid column length. After a while, we see the tendency of too much damping, as with the other test cases.

Figure 4.22 shows that the relation does not perform well for high viscosity liquids either. The damping is way too large compared to the experimental results. This is a little strange, since the model was created with low Reynolds numbers in mind. It is even stranger to see the bad result in Figure 4.23, where the smallest possible Reynolds number from the experimental data has been used.

In general, it seems like the Ogawa U-tube friction model does not apply to a wider range of U-tube flow cases with higher Reynolds numbers. The U-tube used by Knoop had a smooth bend, while Ogawa's U-tube had two relatively sharp bends. This, along with the small Reynolds number range, is the reason why the damping model of Ogawa agreed with his experiments but not with Knoop's experiments.

Nevertheless, Ogawa's model displays a property that we have not seen in other friction models so far. It brings the oscillations to a complete stop. It is obvious that having the velocity in denominator is beneficial when the velocity is low. As a result, the friction does not die off in the same way as the Blasius friction factor does.

The damping term suggested by Ogawa et al. is actually more similar to the laminar friction term than the turbulent ones. In practice, it could be characterized as a laminar friction term that is dependent on the initial amplitude and the liquid column length. Even though the results are not too convincing at the moment, some of the ideas behind this model might be useful later.

4.3.3 Two Preliminary Proposed Friction Models for Oscillating Flow in a U-tube

In this section we look at the simulation results of the friction model proposed in Section 2.2.3. Both an acceleration based friction relation and a relation without acceleration are presented. This is because it was discovered that the results were much better without the acceleration term.

A New U-tube-Specific Steady Friction Relation

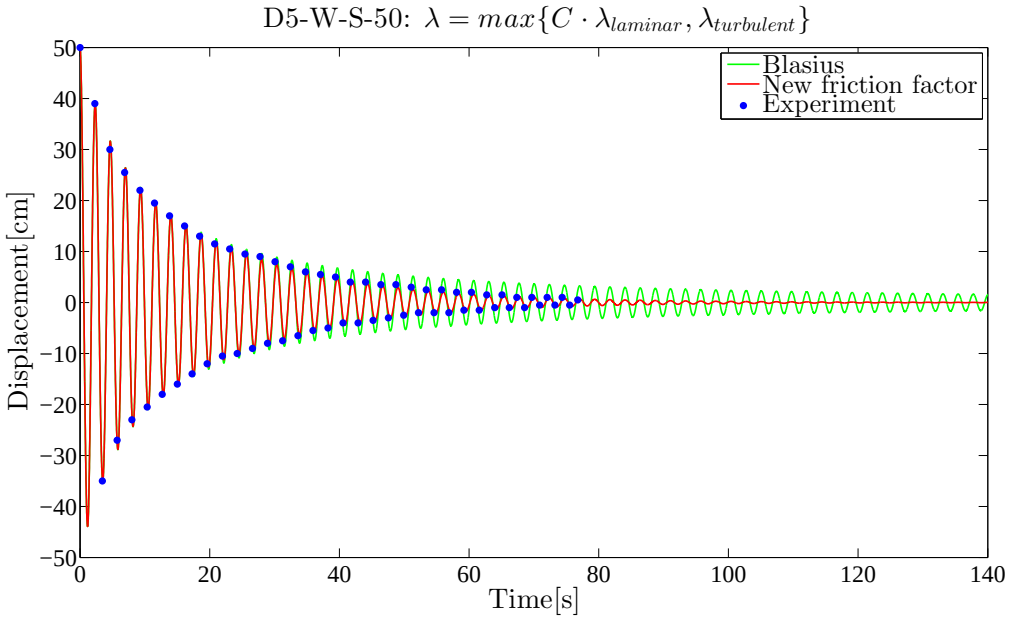

Figure 4.24: The figure shows results from the steady friction model from Section 2.2.3. The experimental results are from [11]. The proposed friction model gives the same amplitude for the oscillations as Blasius during the first 20 seconds. After that, it follows the experimental results very closely. The oscillations of the new model come to rest at about 140 seconds, which is in agreement with the experiment.

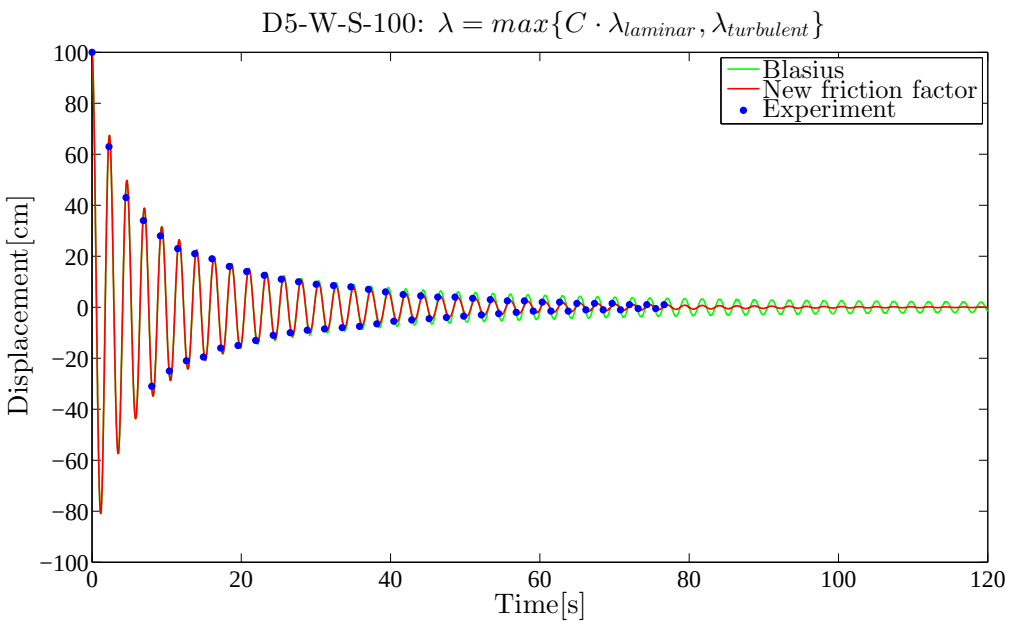

Figure 4.25: The figure shows the same friction models as in Figure 4.24, only with a larger initial amplitude. The same good agreement between the new friction model and the experiments can be observed throughout the entire time period.

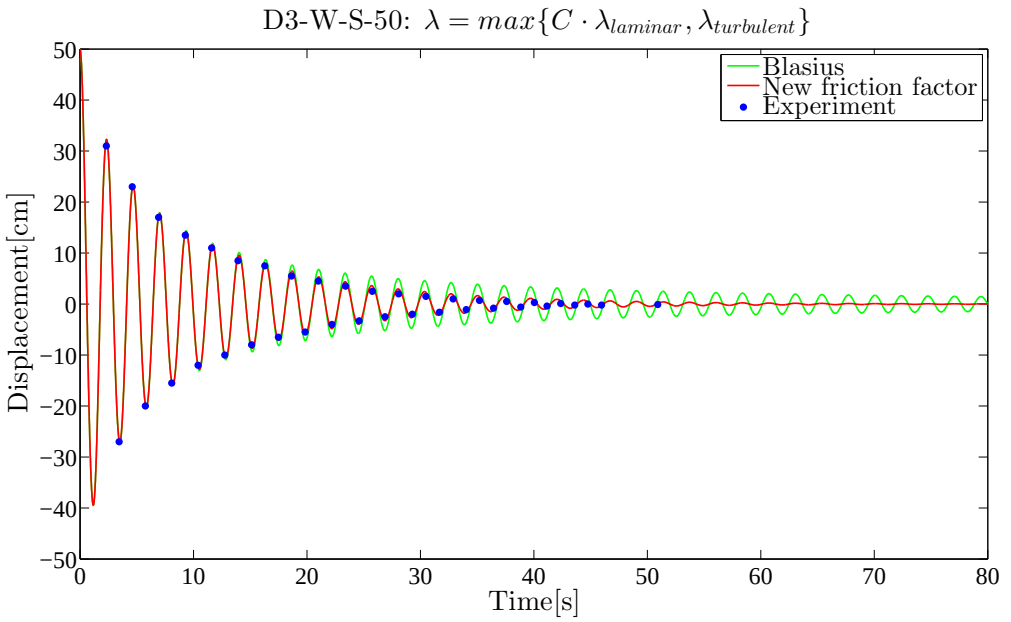

Figure 4.26: The figure shows the same friction models as in Figure 4.24, only with a smaller pipe diameter. The new model very accurately predicts the experimentally observed amplitudes.

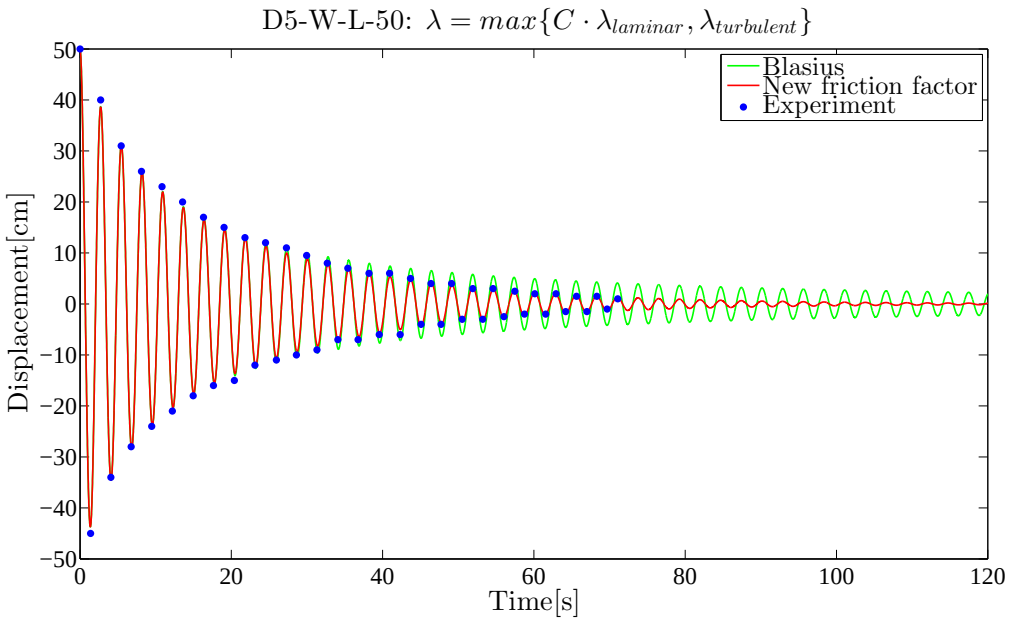

Figure 4.27: The figure shows the same friction models as in Figure 4.24, only with a longer liquid column. The new model very accurately predicts the experimentally observed amplitudes.

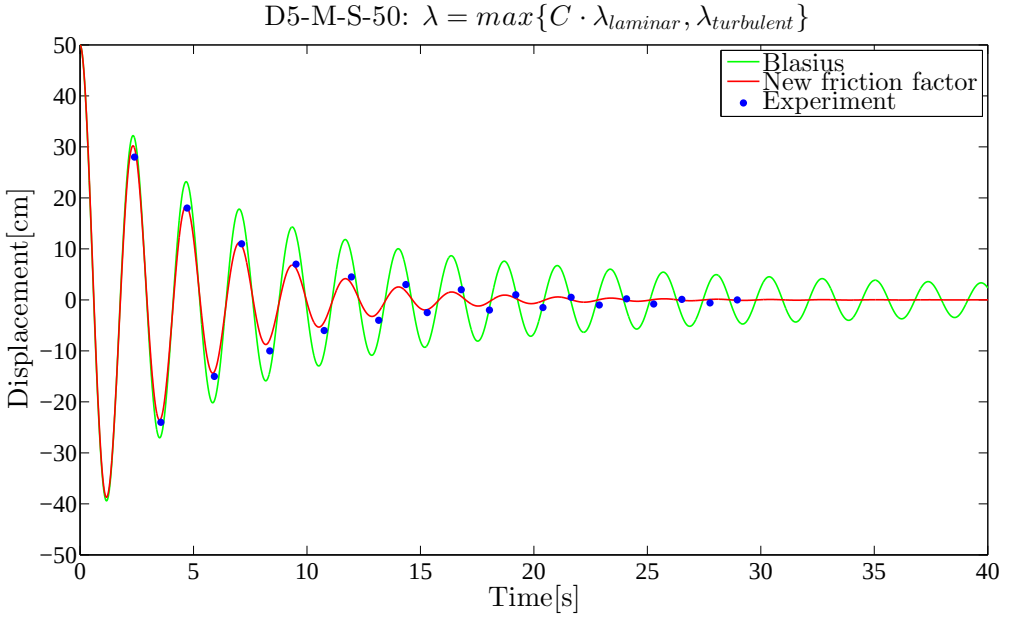

Figure 4.28: The figure shows the same friction models as in Figure 4.24, only with a more viscous liquid. The predicted amplitudes of the new model are satisfying but the period of the oscillations deviates from the experimentally observed. This is the same tendency as previously observed with the Marcol oil.

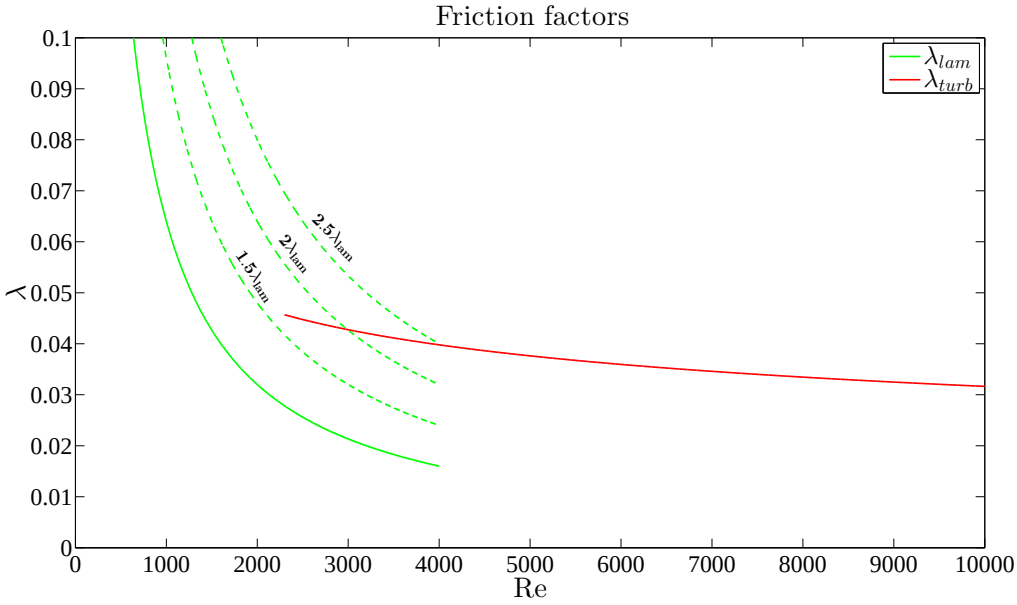

Figure 4.29: Steady laminar and turbulent friction factors plotted as a function of the Reynolds number, where the turbulent friction is represented by the Blasius friction factor. The effect of multiplying the laminar friction by different factors is illustrated by the dotted lines.

The results from the friction expression without acceleration look very promising. This shows that it is indeed possible to make an expression that can accurately predict the experimental results. The success of this method is due to the flexible laminar friction illustrated in Figure 4.29, and the flow parameter dependent coefficient from equation (2.48). Moreover, the oscillations come to a complete stop at approximately the right time. Figures 4.24 - 4.28 show that this holds for variations in both initial amplitudes, pipe diameter, column length and viscosity.

A New U-tube-Specific Acceleration Based Friction Relation

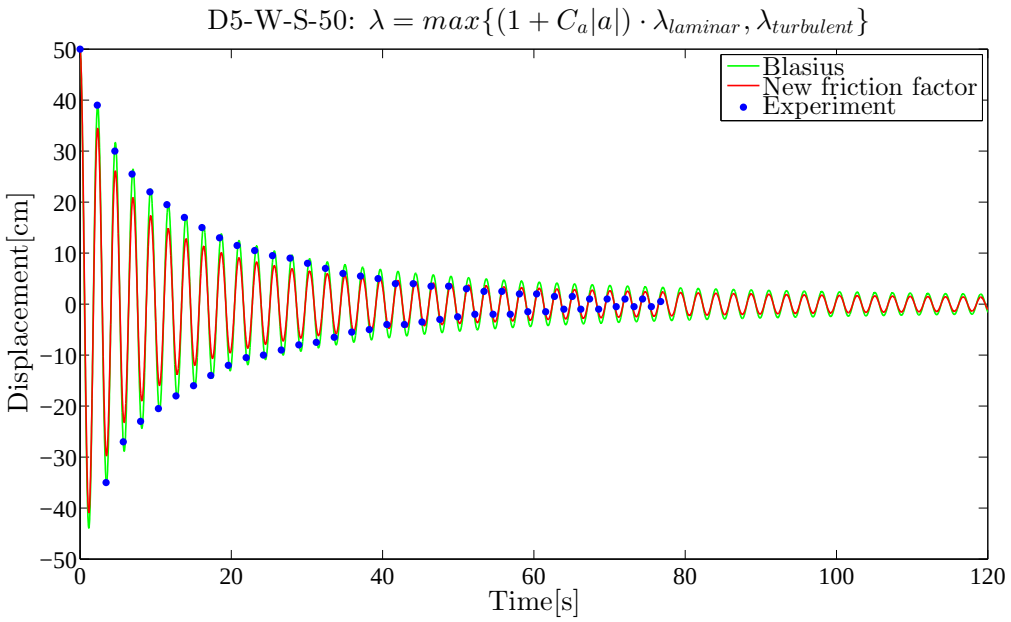

Figure 4.30: The figure shows the results of the proposed acceleration based friction model presented in Section 2.2.3. The friction model resulting from these expressions has a laminar component that increases with the acceleration. The new model is compared to Blasius and the experimental results from [11]. It provides slightly more damping than Blasius for all times but does not make the liquid come to rest.

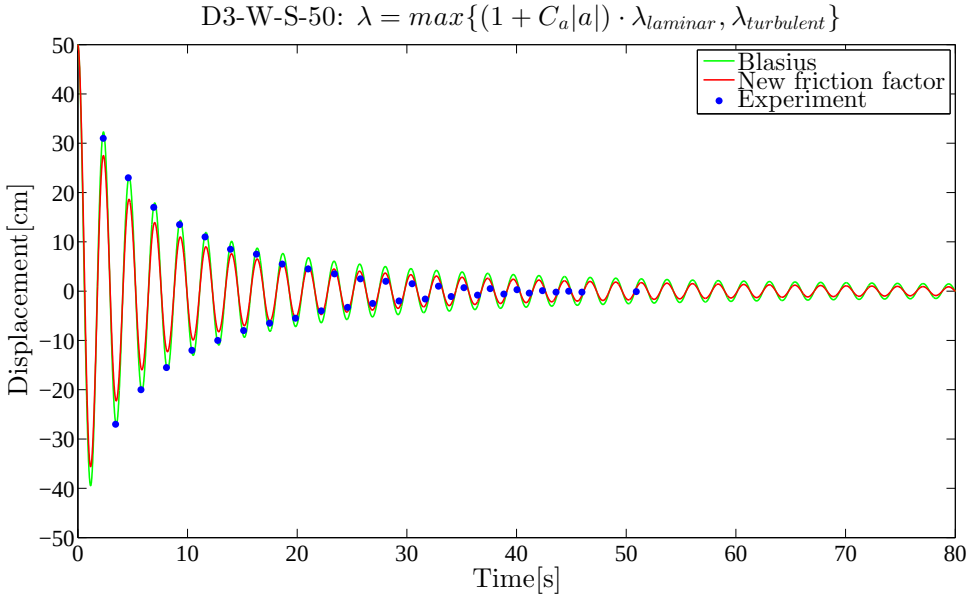

Figure 4.31: The figure shows the same friction models as in Figure 4.30, with a smaller pipe diameter. The results are not in accordance with the experimental results because the friction is not sufficient for small amplitudes.

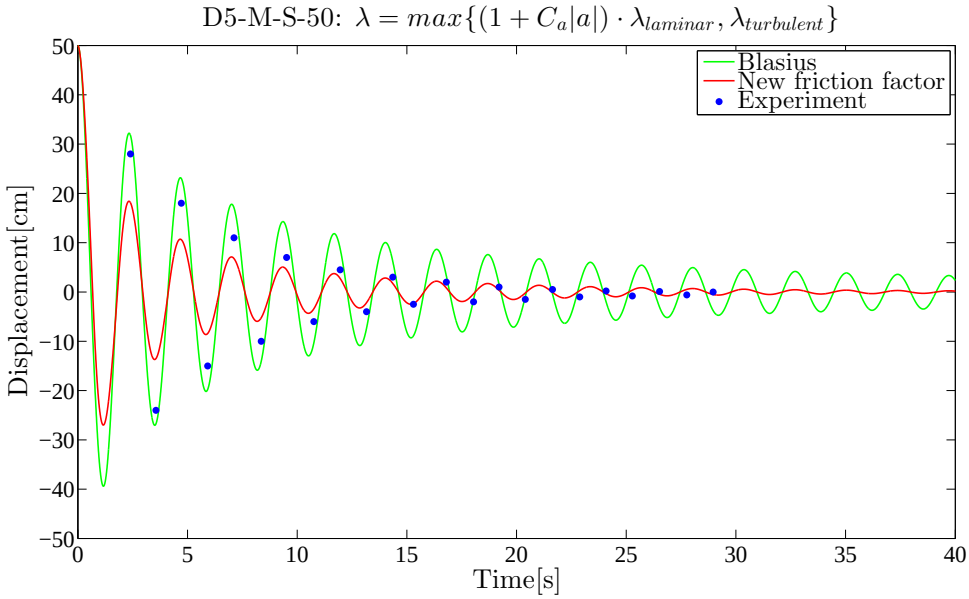

Figure 4.32: The figure shows the same friction models as in Figure 4.30, with a more viscous liquid. The new model yields better results than in Figures 4.30 and 4.31, and comes to rest after about 50 seconds. The predicted period does not comply very well with that of the experiments.

As we can see in Figures 4.30 - 4.32, the acceleration based friction term does not work as intended. Because the average acceleration is decreasing quite rapidly, the additional damping from the coefficient C_a is killed off. The results show more damping than with just Blasius friction, but it is not enough to achieve satisfactory results. The damping is too large for large amplitudes and too small for small amplitudes. The exception is Marcol, where the coefficient C_a seems to be more efficient.

We see that the expression which is not acceleration dependent performs far better than that which has acceleration dependence. The disadvantage of the friction factor without an acceleration dependent term is that it is not valid for other flow cases than the U-tube. It is probably even limited to a U-tube of the same proportions and dimensions that were used in the reference experiments [11]. It is therefore desirable to continue the search for a more general expression; one that will yield regular friction when the flow is steady and additional friction in unsteady flows. This is where the more established unsteady friction relations come into play, as we will see in the next section.

4.4 Unsteady Friction Relations

The results from two different unsteady friction models are presented in this section. Unsteady friction relations are characterized by their acceleration dependence. Earlier discussions have revealed that this is a good idea in theory. However, we have also seen in Section 4.3.3 that the expression needs to be well balanced in order to yield the proper amount of damping.

4.4.1 Frequency-Dependent Friction Models

The simulation results Zarzycki's friction model are presented and discussed in the following subsection. A brief theoretical overview of this method is given in Section 2.3.1. This is the first of three unsteady friction models that are going to be tested in this thesis.

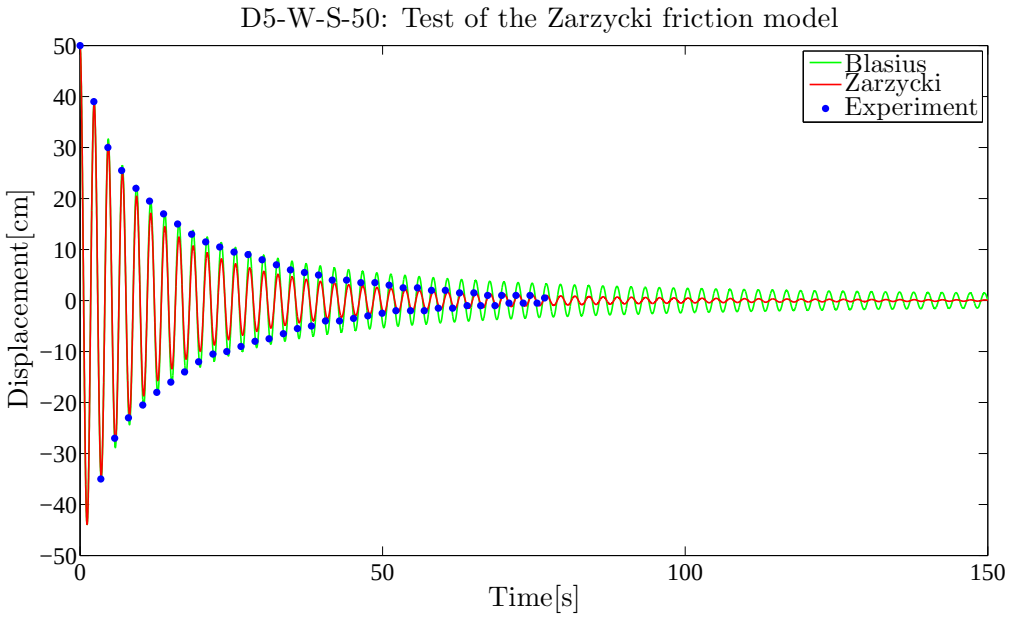

Figure 4.33: The figure shows a comparison of the Blasius friction factor and the friction model presented in equations (2.54) and (2.55). The experimental data are from [11]. The Zarzycki model gives a little too much friction for intermediate times, while it looks promising towards the end of the experimental data range. There is a clear improvement when compared to the steady friction of Blasius.

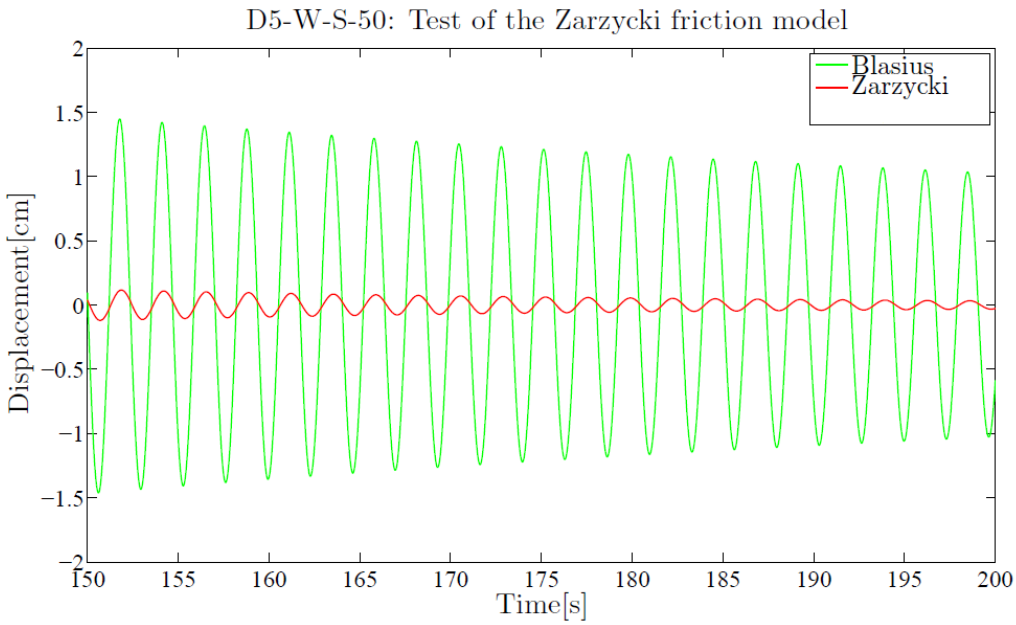

Figure 4.34: A close-up of the last 50 seconds of the result in Figure 4.33 showing that the oscillations have not actually come to rest. Even though the amplitude decreases, this happens way too slowly.

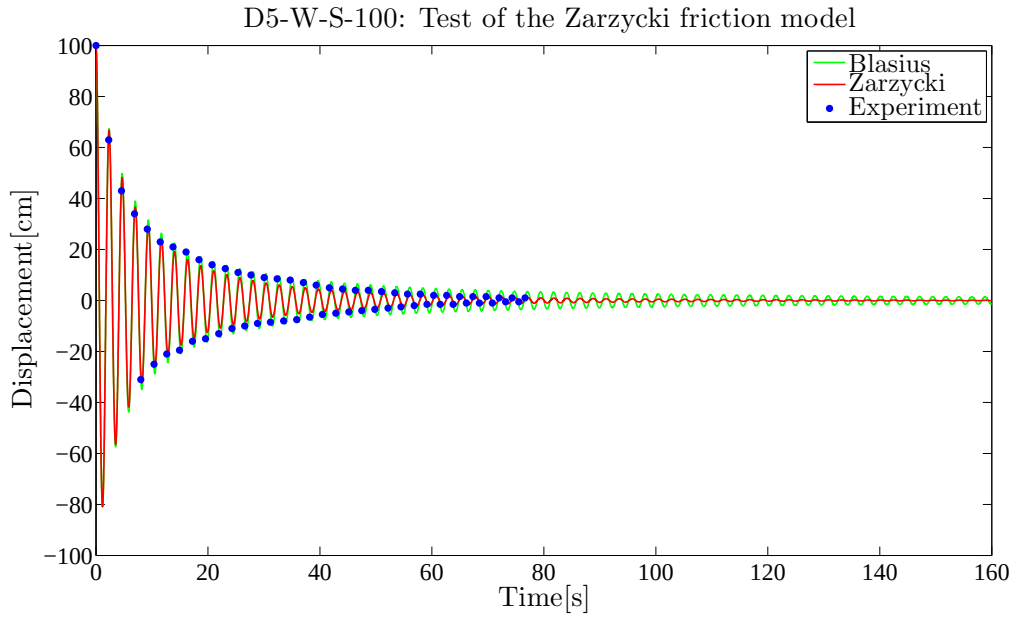

Figure 4.35: The figure shows the same friction models as in Figure 4.33, only with a larger initial amplitude. The amplitude predictions of the Zarzycki model are good, but the liquid does not come to rest fast enough.

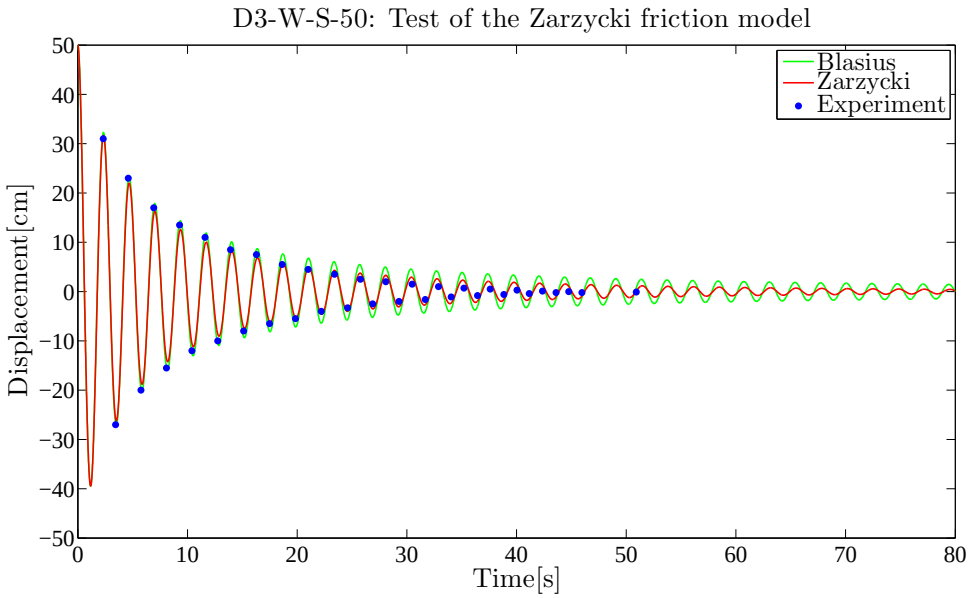

Figure 4.36: The figure shows the same friction models as in Figure 4.33, only with a smaller pipe diameter. Towards the end of the time range of the experiments the Zarzycki model overestimates the amplitude of the oscillations.

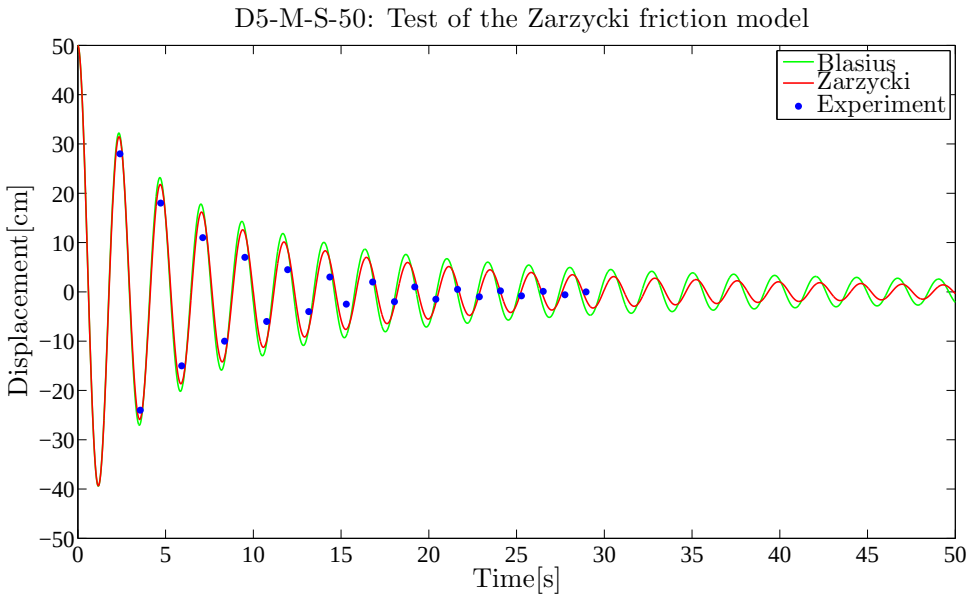

Figure 4.37: The figure shows the same friction models as in Figure 4.33, only with more viscous liquid. The Zarzycki model does not provide much more damping than the Blasius friction relation. The predicted amplitude does not match the experiments. As opposed to all previous models, the period of the Zarzycki model changes a little when the viscosity is high. However, the shift is not enough to match the experimental period.

In Figures 4.35 and 4.33 we see that Zarzycki's method yields promising results when the liquid is water and the pipe diameter is 5cm. The simulated oscillations follow the experimental oscillations very well throughout the entire duration of the experimental measurement. It thus seems like Zarzycki's method is not much affected by the initial amplitude. Nevertheless, it is worth noting that the oscillations do not come to a complete stop in either of the figures. This is illustrated in Figure 4.34. It was reported in [11] that the oscillations stopped after about 146 seconds.

Figure 4.36 shows that the pipe radius has a larger influence on the results. We see that the friction coefficient is too small to provide enough damping as the amplitude decreases. The weighting function in equation (2.55) is in fact strongly dependent on the pipe radius through the dimensionless time parameter, $\hat{t} = \nu t/R^2$. This parameter goes into an exponential function, so that small changes make significant differences. This makes the Zarzycki model yield much less accurate results for the small diameter pipe.

Looking at Figure 4.37, we see that the type of liquid also plays a big role in the performance of the Zarzycki method. The high viscosity of Marcol makes the simulation fail to provide the sufficient amount of damping. The kinematic viscosity, ν, is included in the dimensionless time parameter as well as in the Reynolds number. This is probably where the error occurs. A possible explanation to the discrepancies could be that the coefficients from equation (2.57) were developed with only water in mind. This is likely because Zarzycki's model was developed mainly for water hammer simulations.

4.4.2 Instantaneous Acceleration Based Models (IAB)

The results of the modified Brunone model will be displayed and discussed in this section. Both of the shear decay coefficients discussed in Section 2.3.2 will be used, so that the best choice for U-tube oscillations can be found. They will also be compared to the results of Blasius' friction factor and experimental data.

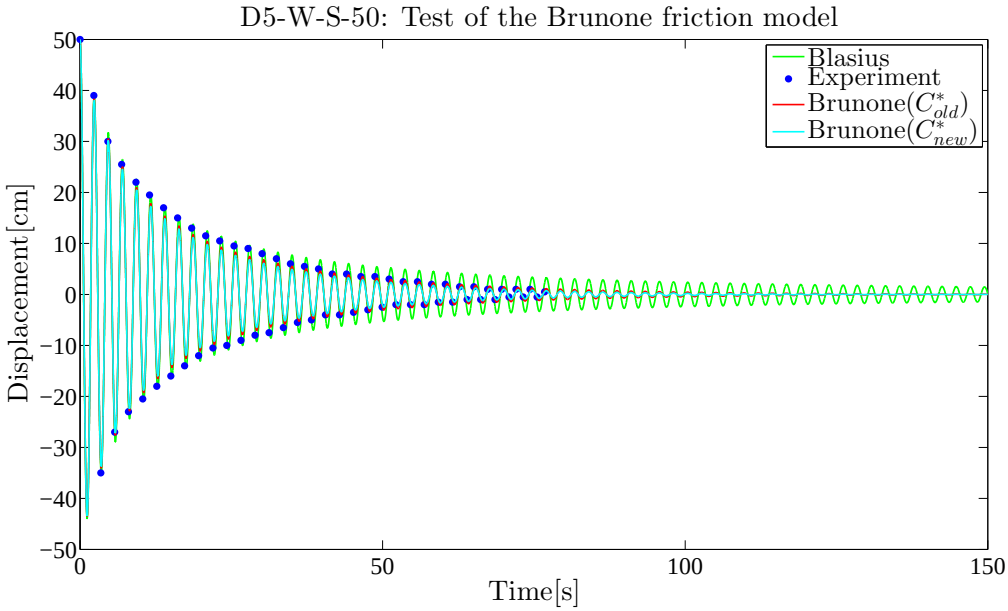

Figure 4.38: The figure shows a comparison of the Blasius friction factor and the friction model presented in equation (2.69). The shear decay coefficients C^*_{old} and C^*_{new} are presented in equations (2.65) and (2.66), respectively. The experimental data are from [11]. In the figure we see that C^*_{new} provides slightly more damping than C^*_{old}. The two Brunone expressions make the simulations match the experiments, and then come to rest at about 140 seconds. The effect of the additional unsteady friction is clearly visible in the difference between Brunone and Blasius.

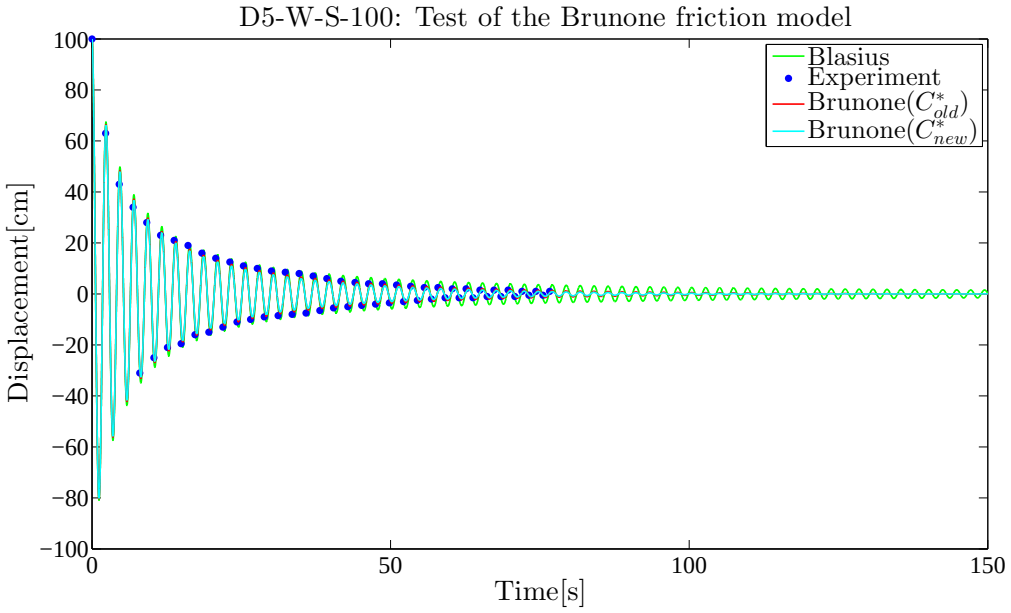

Figure 4.39: The figure shows the same friction relations as in Figure 4.38, only with a larger initial amplitude. C^*_{new} provides slightly more damping than C^*_{old}. The two Brunone expressions make the simulations match the experiments, and then come to rest at about 140 seconds.

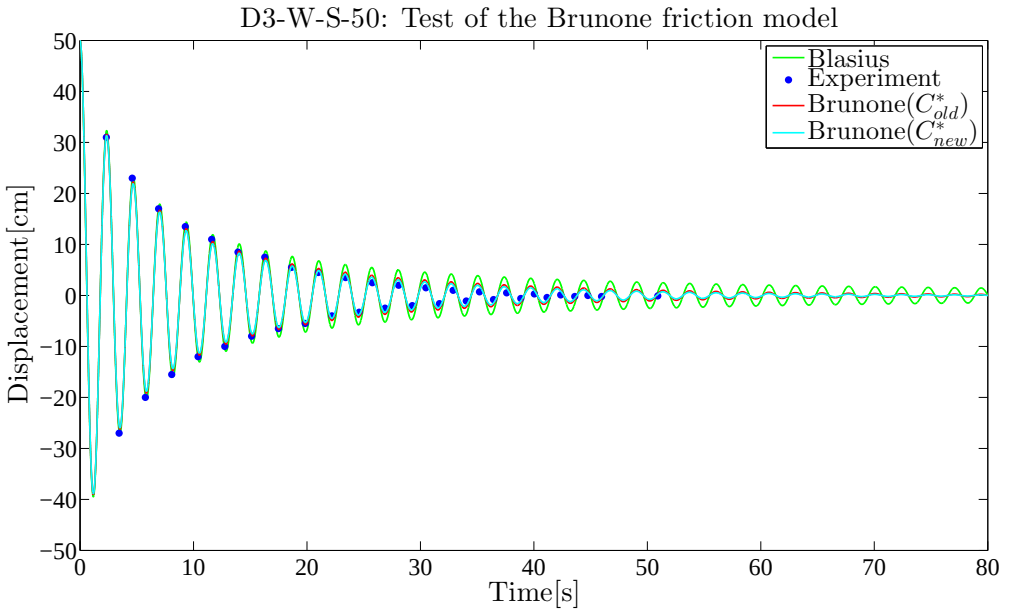

Figure 4.40: The figure shows the same friction relations as in Figure 4.38, only with a smaller pipe diameter. C^*_{new} provides slightly more damping than C^*_{old}. The expressions with an unsteady friction correction follow the oscillations of the experimental data to a large extent.

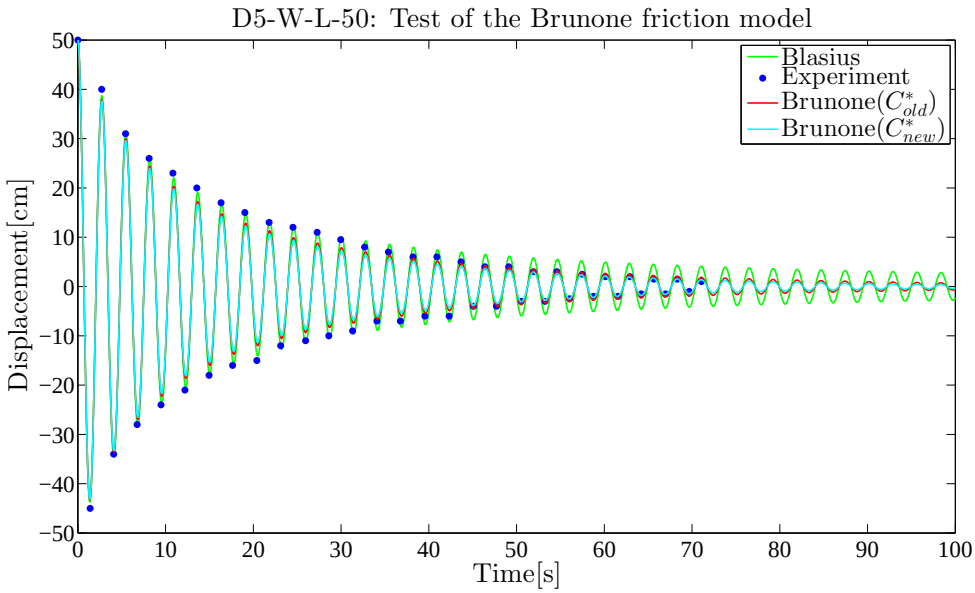

Figure 4.41: The figure shows the same friction relations as in Figure 4.38, only with a longer liquid column. C^*_{new} provides slightly more damping than C^*_{old}. The Blasius friction factor performs slightly better than the expressions with an unsteady friction correction the first 35 seconds. After that, Blasius overshoots the amplitude and the two Brunone expressions perform better.

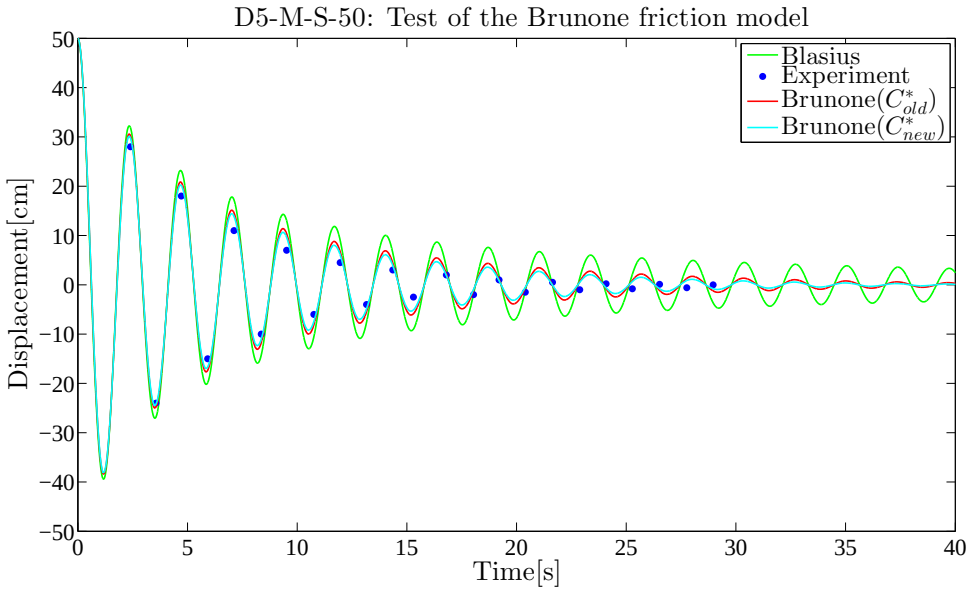

Figure 4.42: The figure shows the same friction relations as in Figure 4.38, only with a more viscous liquid. C^*_{new} provides slightly more damping than C^*_{old}. The unsteady correction of the turbulent friction factor is less effective in this case because the flow gradually enters a regime dominated by laminar flow. The period discrepancy between simulations and experiment becomes quite prominent towards the end of the time range. The Brunone expressions still provide significantly more damping than the steady friction from Blasius.

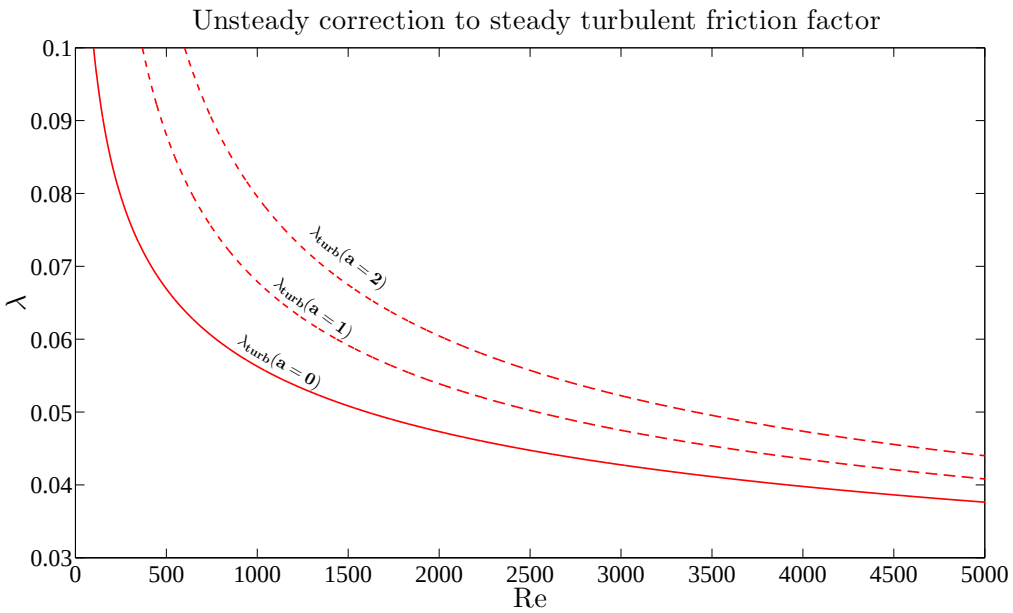

Figure 4.43: The figure shows the turbulent friction relation with unsteady correction from equation (2.69). Three different values have been chosen for the acceleration: 0m/s^2, 1m/s^2 and 2m/s^2. We see that the effect of the acceleration is largest for low Reynolds numbers. The newest shear decay coefficient, C^*_{new}, has been used in this figure. Note that the y-axis does not start at zero.

In Figures 4.38 and 4.39 we see that the friction relation in equation (2.69) works very well for water with the large pipe diameter. These two figures exhibit all the properties that we are looking for; the amplitude predictions are consistent with all the experimental points, the period matches, and the oscillations come to rest at about the right time. By comparing to the result of the Blasius friction factor, we can easily see the improvement the unsteady friction brings to the table.

The predictions from the simulations are still very accurate when the column length is changed in Figure 4.41, both with respect to amplitude and phase. The smaller pipe diameter in Figure 4.40 causes the simulations to slightly over-estimate the amplitude of the oscillations. Moreover, the period is no longer as good a match as before. However, the oscillations come to rest within a reasonable time and the amplitude predictions are still better than we have seen in any of the other models that have been tested.

Figure 4.42 shows the result from the viscous Marcol oil. This time, the simulations are not as accurate as before, both when it comes to the amplitude and the period of the oscillations. This is still the best result that we have seen so far for any friction model. Most of the models that have been tested have been developed for transient water hammer cases, and this is the case for the Brunone model as well. The shear decay coefficients have as far as the writer knows not been tested for viscous oils. It is therefore quite remarkable that the simulations are as good as they are. Even though it is not completely accurate, the Brunone friction model follows the experimental data relatively well, and then comes quickly to rest.

It is quite clear from all of the figures that the newest version of Vardy and Brown's shear decay coefficient provides more friction, which is what they stated in their paper [5]. The additional damping is desirable in almost all of the above test cases because the simulations over-estimate the amplitude more often than they under-estimate it. In Figures 4.38, 4.39 and 4.41 the basic steady friction model of Blasius actually provides a better damping profile than that of Brunone for the first 20-30 seconds. However, the additional damping in Brunone is not severe. The main problem of this entire project has been to provide more damping. The newer version of the shear decay coefficient is therefore considered the best. It is both more theoretically correct and provides slightly more damping.

From the above results, we see that the use of acceleration in the friction coefficient works very well as long as it is used together with the shear decay coefficient. The balance between these two parameters makes the simulations yield results that are much better than those obtained from only using the acceleration in the previously proposed friction relation. This is very good news, as the acceleration is a parameter that we would like to have in the friction expression for two reasons: Firstly, the unsteady contribution becomes zero whenever the liquid is not accelerating. Secondly, we have extra friction at the moment of the turning of the liquid column. This is illustrated in Figure 4.43, where the effect of the unsteady addition to the friction coefficient is illustrated. This is something that we wanted to address earlier, but it was only possible with the contribution from a flow dependent shear decay coefficient such as that in equation (2.66).

4.5 Concluding Solution to U-tube Friction

The results from the concluding friction relations presented in Section 2.4 will be presented and compared to the experimental results from [11]. As these are the final results of the friction study, they will be compared to all of the available experimental data sets. In addition to the usual five cases, three more figures will be displayed and discussed below. The rest of the results are displayed in Appendix 6.2.

Below is an abbreviation of equations (2.70) - (2.72) with the keyword that is going to be used in the legend of the figures below. We remember from the theory section that the friction coefficient with the laminar correction is already regarded as the concluding result.

Friction coefficient with laminar correction: $\lambda = \mathbf{max}\{(\lambda_{\mathbf{laminar}} + \lambda_{\mathbf{unsteady}}), \lambda_{\mathbf{turbulent}}\}$

Friction coefficient with turbulent correction: $\lambda = \mathbf{max}\{\lambda_{\mathbf{laminar}}, (\lambda_{\mathbf{turbulent}} + \lambda_{\mathbf{unsteady}})\}$

Friction coefficient with dual correction: $\lambda = \mathbf{max}\{\lambda_{\mathbf{laminar}}, \lambda_{\mathbf{turbulent}}\} + \lambda_{\mathbf{unsteady}}$

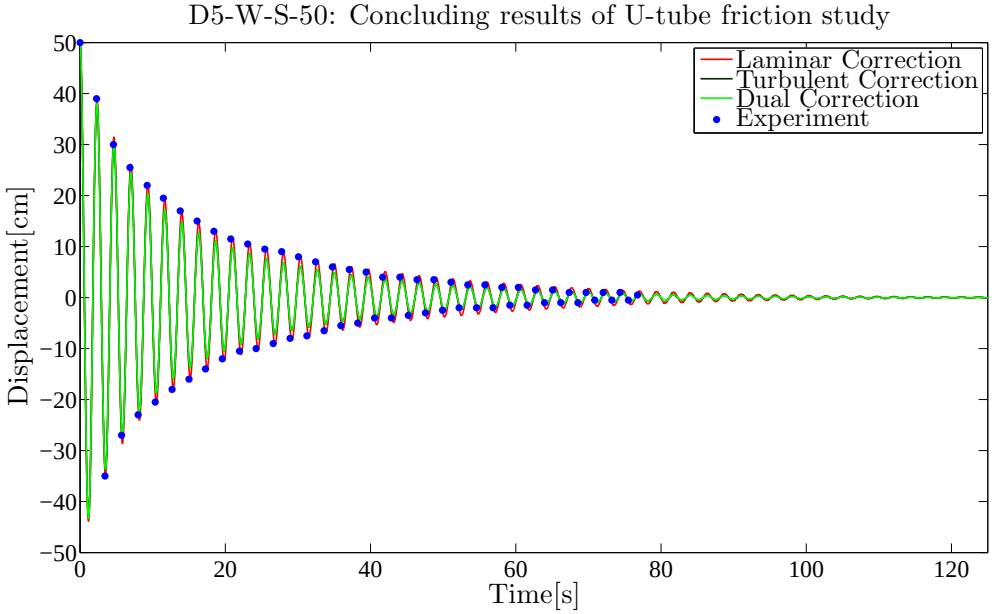

Figure 4.44: The figure shows the result of using the final friction relations in equations (2.70) - (2.72) to simulate liquid oscillations in a U-tube. The experimental data are from [11]. The laminar correction provides slightly less damping in the turbulent regime. It therefore gives slightly larger amplitude up to 120 seconds, where it becomes approximately equal to the other two friction relations. The light and dark green lines follow each other through the entire time span.

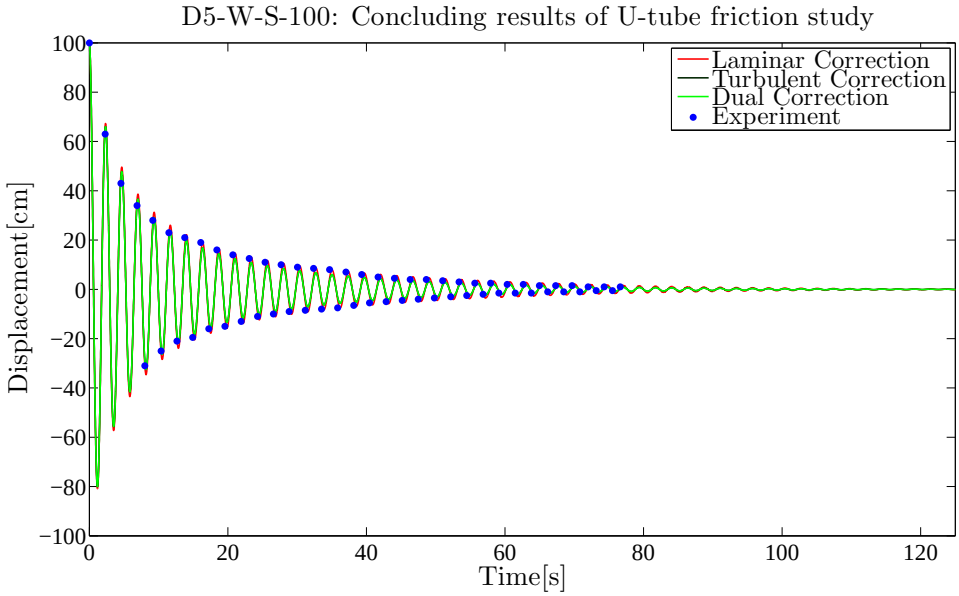

Figure 4.45: The figure shows the same friction models as in Figure 4.44, only with a larger initial amplitude. Like in the previous figure, the laminar correction provides slightly less damping in the turbulent regime. This makes for a little better approximation of the experimental results in the mid-time range. The light and dark green lines are on top of each other during the entire time span.

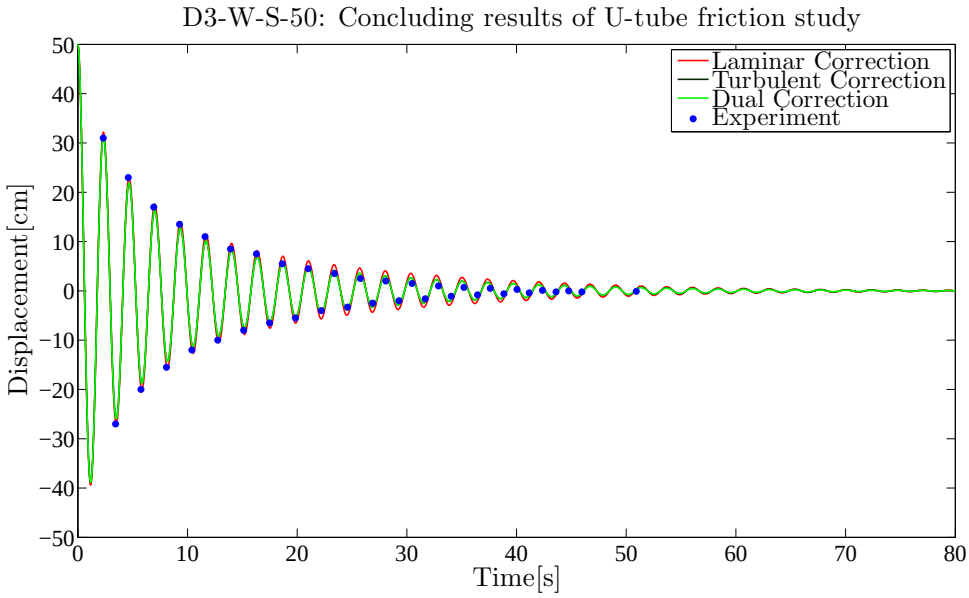

Figure 4.46: The same friction models as in Figure 4.44, only with a smaller pipe diameter. The coefficients with turbulent and dual correction are still completely similar. They are closer to the experimental data points than the laminar correction during the entire time range. After about 70 seconds, all of the expressions give the same amplitude.

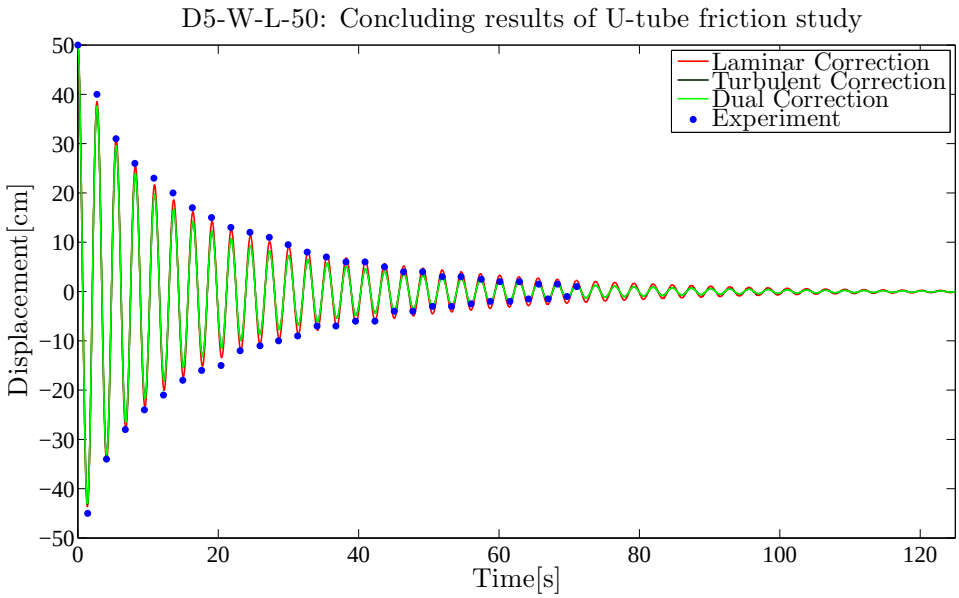

Figure 4.47: The same friction models as in Figure 4.44, only with a longer liquid column. The laminar correction gives less damping in the turbulent regime, which makes it come closer to the experimental data most of the time. The turbulent and dual corrections yield the same results all the time, and they are joined by the laminar correction after about 120 seconds.

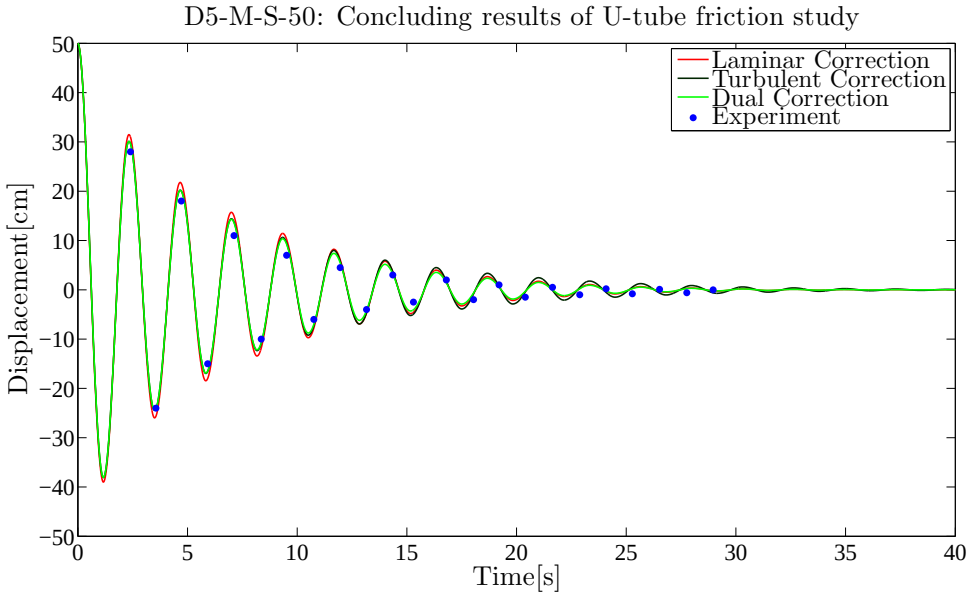

Figure 4.48: The figure shows the same friction models as in Figure 4.44, only with a more viscous liquid. When the velocity is high, the laminar correction overshoots more than the two other expressions. After about 15 seconds, it catches up with the turbulent correction and starts to provide more damping. By 25 seconds, the laminar and dual corrections are the same. The turbulent correction gives the largest amplitudes from 15 seconds and out. All of the friction models are slightly overshooting during the entire time of simulation.

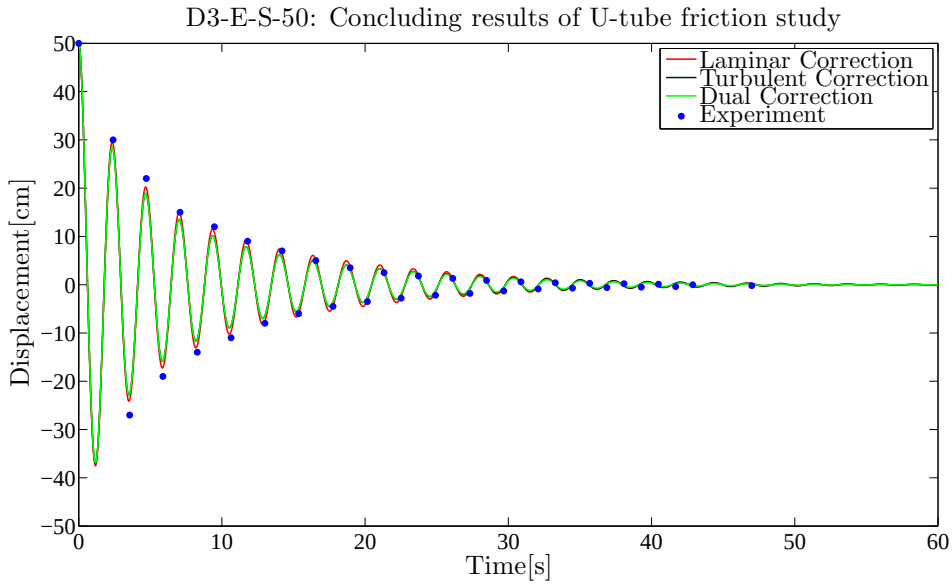

Figure 4.49: The figure shows the same friction models as in Figure 4.44, only with a slightly more viscous liquid and a smaller pipe diameter. The laminar correction gives the largest amplitude up to 30 seconds, where the turbulent correction takes over. The simulations generally perform well compared to the experiments. However, there is a slight period discrepancy that becomes more prominent towards the end.

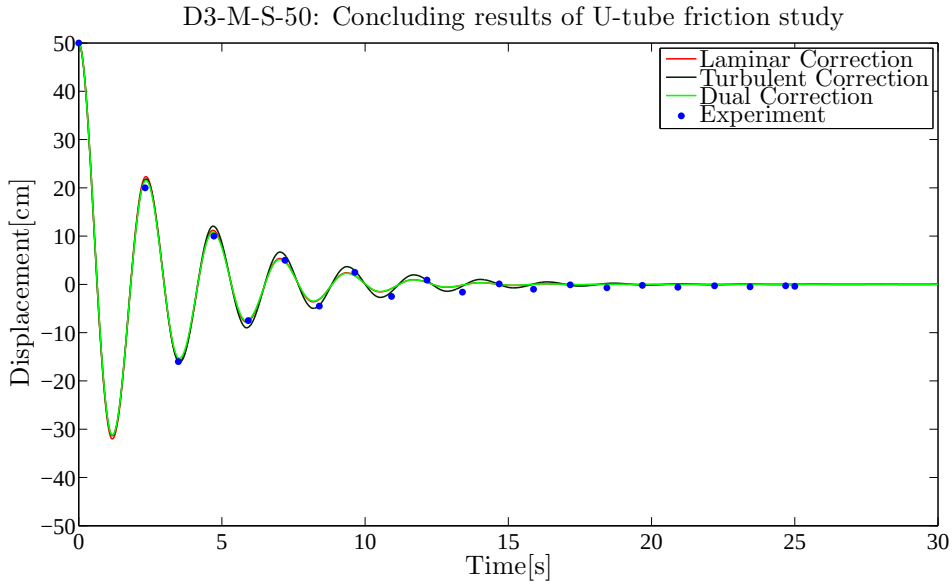

Figure 4.50: The figure shows the same friction models as in Figure 4.44, only with a more viscous liquid and a smaller pipe diameter. This results in a low Reynolds number flow, where the friction coefficient with laminar correction starts out with the largest amplitude and ends up with amplitude equal to that of the dual correction. The friction coefficient with turbulent correction gives the largest amplitude from 5 seconds and out. The simulations come to rest a little before what has been experimentally observed. There is a prominent period discrepancy for all of the expressions.

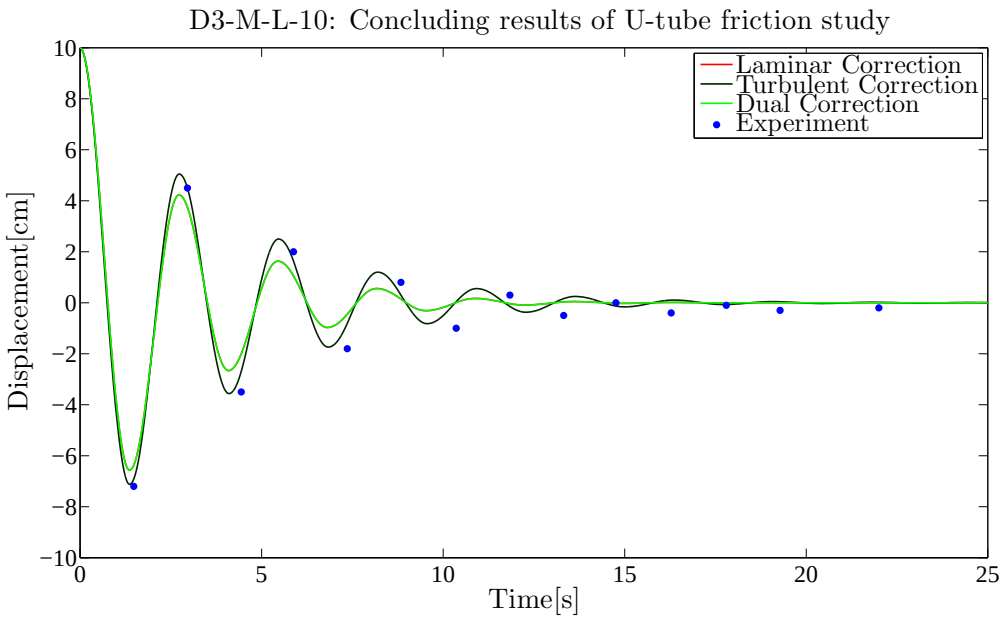

Figure 4.51: The figure shows the same friction models as in Figure 4.44, with a more viscous liquid, a smaller pipe diameter, and a smaller initial amplitude. This results in a flow that is almost completely in the laminar regime. Hence, the turbulent correction provides the least damping, while the two others yield the same results. The laminar and dual corrections come to rest quite long before the experimental data does. There is a period discrepancy that becomes more prominent towards the end.

In general, the simulations with the new friction relations perform very well for all of the tested flow cases. The results are not always perfect compared to the experiments, such as is the case in Figure 4.51. However, the friction relations make the oscillations follow the experimental data points in a satisfying way in the rest of the figures. This means that they are valid for a very wide range of test cases. In addition, the simulated oscillations come to rest at approximately the right time. The combination of versatility and stopping power therefore makes all three relations satisfying solutions to the initial problem of this thesis.

The differences between the performance of the relations in equations (2.70) - (2.72) are visible in all of the figures. The friction relation with the laminar correction gives less damping than the other two in the turbulent regime. When the flow enters the laminar regime, it catches up with the others due to the added friction from the unsteady component. Based on the comparisons, it is hard to say whether or not the lack of additional turbulent damping makes the friction relation better or worse than the other relations.

The relations with turbulent and dual corrections perform very similarly in most of the test cases because we are mostly within the turbulent regime. However, the differences are clearly illustrated in Figure 4.48. In this case, they start out equal because the flow is in the turbulent Reynolds number regime. After 10-15 seconds, the turbulent dominance clearly vanishes. As a result, the amplitude of the relation with a turbulent correction becomes larger than the one with a dual correction. Subsequently, the laminar correction provides more damping and its amplitude approaches that of the dual correction relation.

To sum up, one can say that the dual correction relation will always provide the largest damping. The two other relations will dominate in their respective regimes. There is no final answer as to what relation is the best, it depends on the flow regime.

With these results in mind, we can say that the choice of the relation with the laminar correction as the final result of the friction study is justified. In addition to good performance, it has the advantage of not altering the turbulent friction coefficient. This is because the unsteady correction only is applied to the laminar friction factor. It is therefore more likely that this friction relation will not interfere with established friction coefficients if implemented in more general flow simulation programs.

4.6 Experimental Work on a U-tube with an Inner Diameter Change

The results from the experimental work on the U-tube with an inner diameter change will be presented and discussed in this section. Only the results from the best lighting conditions have been considered, which was the option with the least amount of light, see Figure 4.52.

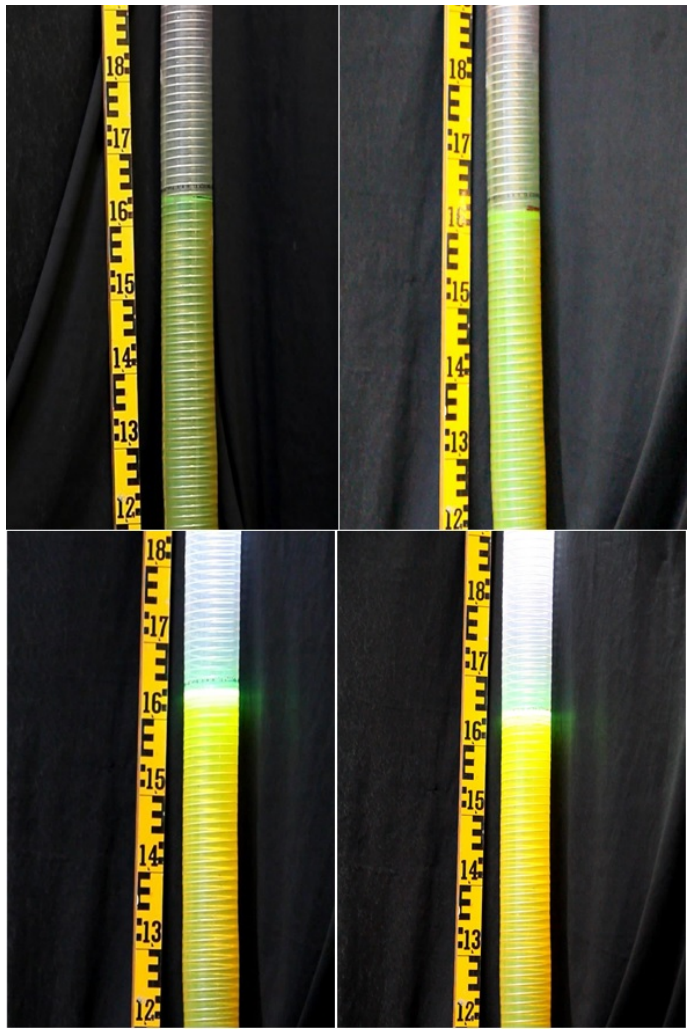

Figure 4.52: The figure shows one picture from each of the light setting configurations used in the experiments. See Table 3.3. Top left: No light in the ceiling or flashlight (C=0,F=0), Top right: Light in the ceiling and flashlight off (C=1,F=0), Bottom left: No light in the ceiling and flashlight on (C=0,F=1), Bottom right: Light in both the ceiling and flashlight (C=1,F=1). The images are extracted from movies used to record the movement of the interface.

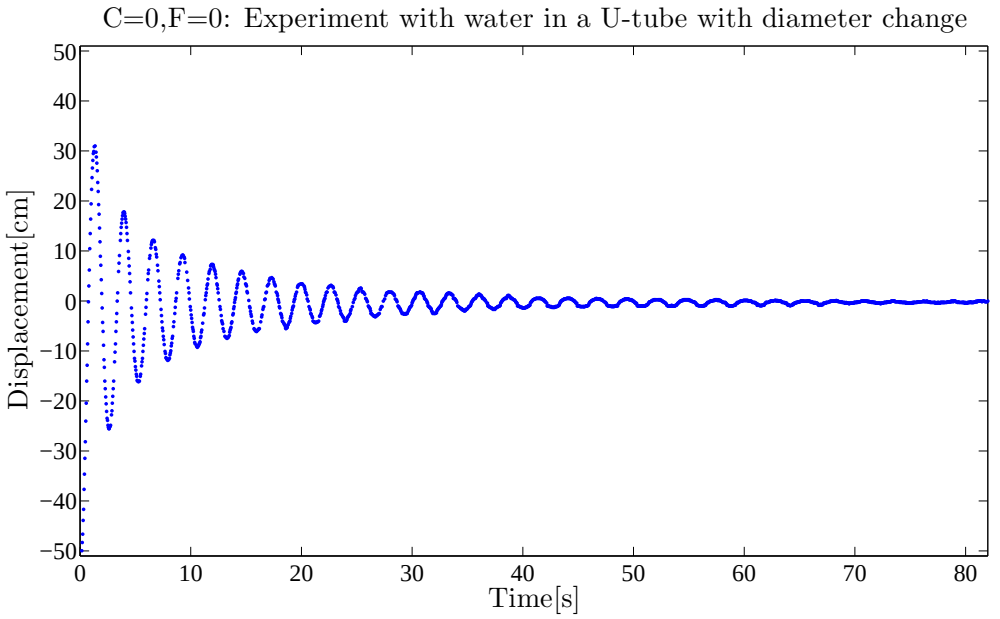

Figure 4.53: The resulting plot from the interface tracking algorithm that was presented in Section 3.2.2. The light conditions were the same as in the top left image in Figure 4.52: no lights in the ceiling and no flashlight. The initial amplitude was 51cm.

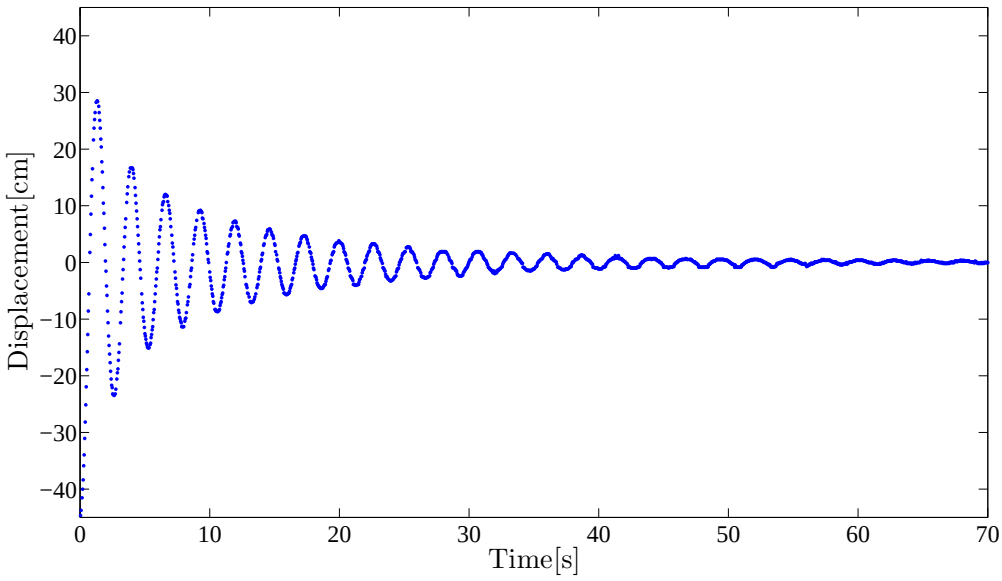

Figure 4.54: The figure shows the results from the interface tracking algorithm in Section 3.2.2, with the same light conditions as in Figure 4.53. The initial amplitude was 45cm.

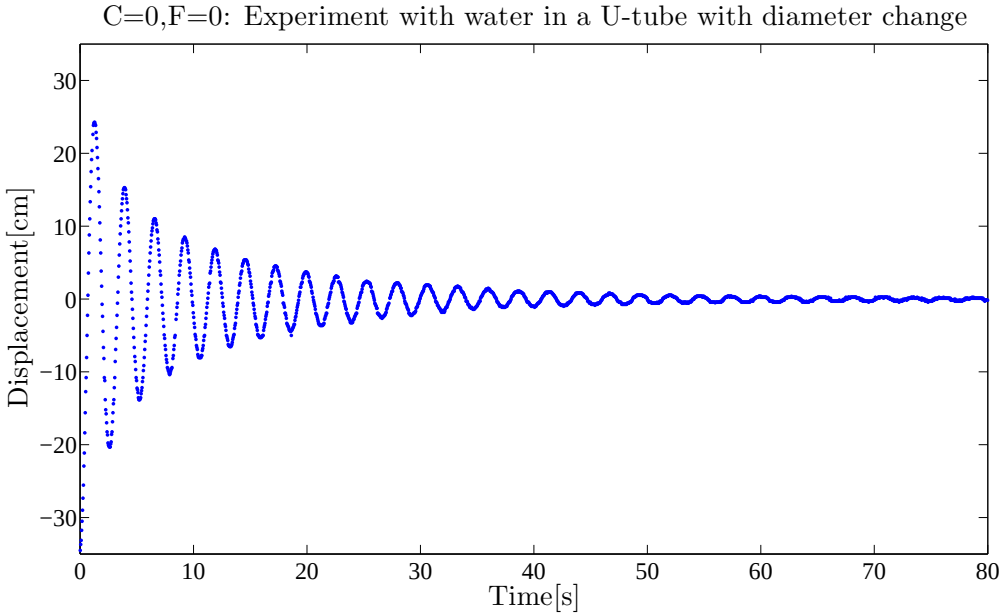

Figure 4.55: A figure showing the results from the interface tracking algorithm in Section 3.2.2, with the same light conditions as in Figure 4.53. The initial amplitude was 35cm.

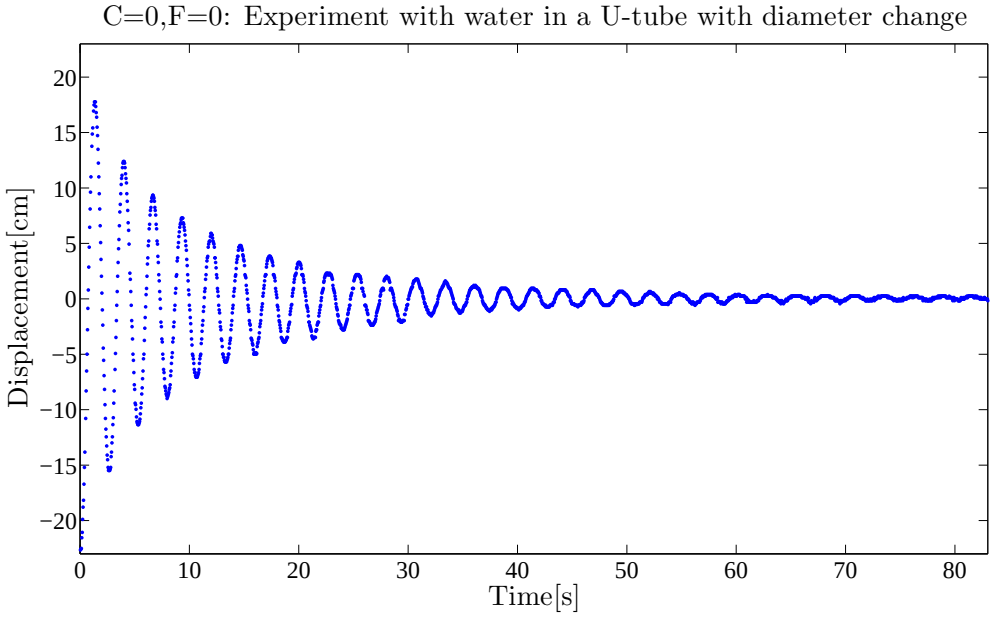

Figure 4.56: A figure showing the results from the interface tracking algorithm in Section 3.2.2, with the same light conditions as in Figure 4.53. The initial amplitude was 23cm.

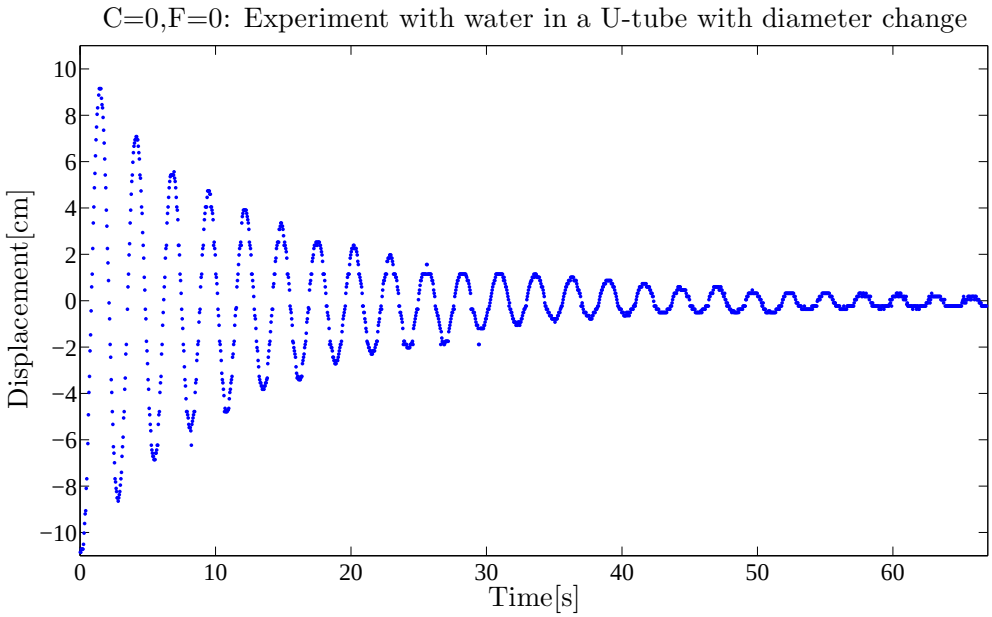

Figure 4.57: A figure showing the results from the interface tracking algorithm in Section 3.2.2, with the same light conditions as in Figure 4.53. The initial amplitude was 11cm. The horizontal gaps in the data originate from the steel wires that were embedded in the tube. The light reflected from the wires was nearly white, which made the interface tracking program skip this particular region.

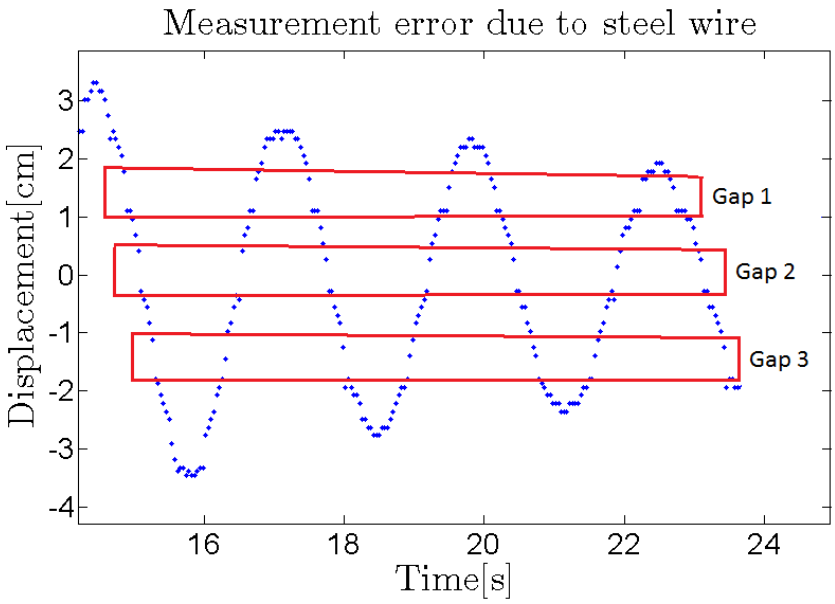

Figure 4.58: The figure shows the region with the most prominent gaps from Figure 4.57. Three gaps have been chosen for the error analysis; they are denoted Gap 1, Gap 2 and Gap 3.

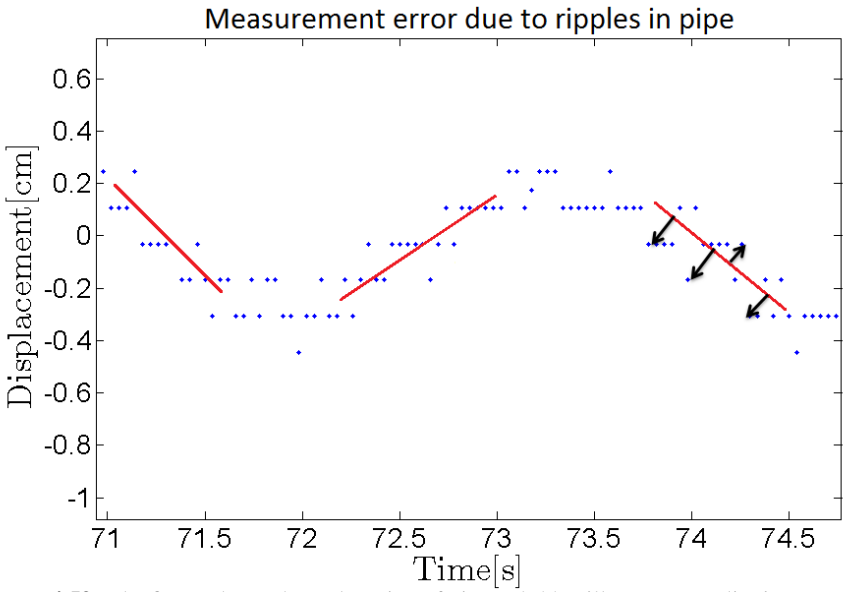

Figure 4.59: The figure shows the end section of Figure 4.55 to illustrate a qualitative error analysis. The red lines that have been drawn in the plot represent the approximate mean value of the data points. The black arrows represent examples of the maximum error distance between the qualitative mean and the data points. The bands of data points are probably caused by ripples in the pipe, as illustrated in Figure 4.60.

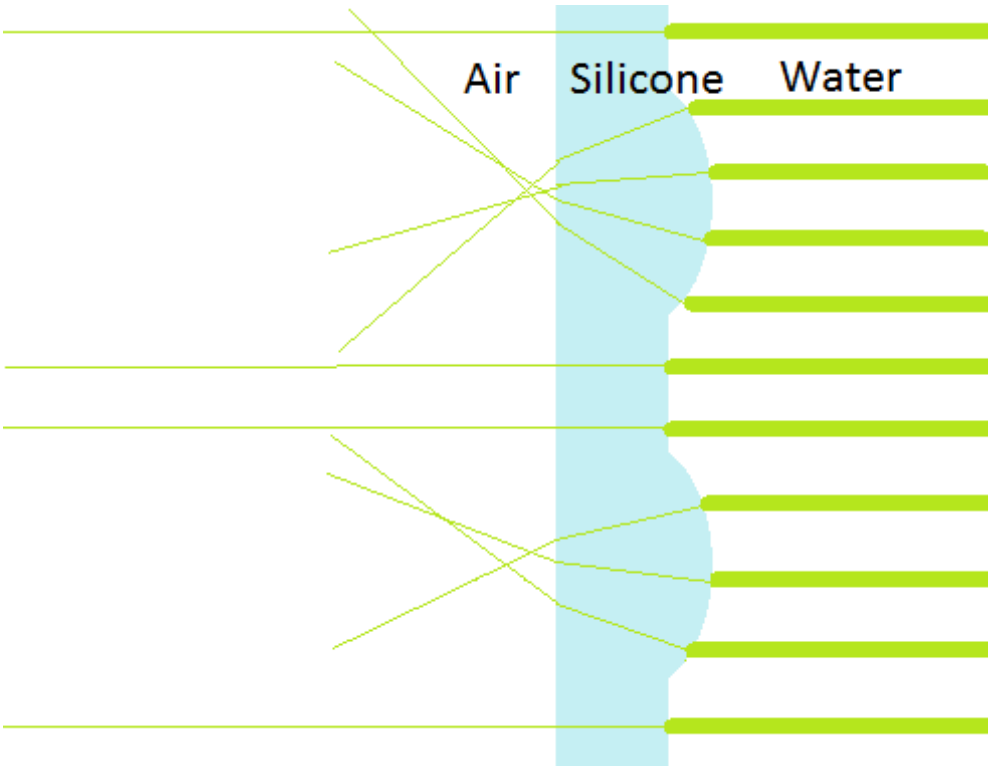

Figure 4.60: The figure shows a qualitative ray tracing analysis of the light coming from the liquid interface in the tube. The silicone pipe wall is colored light blue in the figure; the bumps represent the observed ripples inside the tube. To the left of the wall is air, while there is water to the right. The thick, horizontal, green lines represent different positions of the liquid interface. The thin green lines qualitatively illustrate how the light from each of the positions might travel through the tube wall and the air outside. The bumps act as lenses, deflecting the light from the interface. When the light reaches the interface between the silicone and the air, it is refracted according to Snell's law due to the density difference of the mediums [30]. When the rays are perpendicular to the interfaces, they will keep going in a straight line. It is these rays that are detected by the camera.

4.6.1 Discussion of Interface Tracking and Experimental Conditions

The initial amplitude of the liquid column oscillations presented in Figures 4.53 - 4.57 does not have a sequential interval from one figure to another. The fact that the amplitudes do not have constant intervals between them is due to the experimental procedure. One end of the tube was lowered until the interface in the other leg was at the desired initial amplitude. The weakness of the procedure was that the interface level had to be decided from reading off the ruler depicted in Figure 3.3. Moreover, it proved difficult to achieve an instant seal with the rubber glove in the end that was lowered down. Hence, the interface always moved a little before the end of the tube was completely sealed off.

It turned out to be very difficult to obtain good results from the recordings that were made with the flashlight on. As we see in Figure 4.52, there is a thick line of white light surrounding the interface. In addition, the tube itself is so heavily lit up that it compromises the interface detection even further. This is the reason why these experiments were not used to generate further results. In fact, the light setting with the least light turned out to be the best to work with in the image processing.

Comparing the top images in Figure 4.52 we see the reason why a minimum light yielded the best conditions for the interface tracking algorithm. When the light in the ceiling was turned on, the steel wires were more lit up, as seen from the camera's point of view. The reflected white light from the wires therefore "ruined" more pixels. In addition, the ceiling light left a strip of light at the center of the tube, which also compromised the values of the color components in the pixels.

The type of tube that was used in the experiment caused difficulties for the interface tracking. As we can see from Figure 3.4, the steel wires reflected the ambient white light from the laboratory, regardless of the light setting that was chosen. In the Image Tool table in Figure 3.4, the pixels with the wire in them had the maximum value of 255 for all color components. It was therefore never possible to get a reading of the interface if it was directly behind one of the wires. According to the algorithm, the next pixel row with valid color combinations will therefore be taken as the interface level. This causes the plots in Figures 4.53 - 4.57 to have horizontal bands with no points and horizontal bands with too many points. This is most prominent in Figure 4.57, because the reflections were most intense at the center of the tube, around the equilibrium point.

In all of the result figures, the amplitudes look a little deformed between 40 and 60 seconds. This is because the amplitude of the oscillations by this time has reached about the same level. At this particular point, the interface is covered by the steel wire at both the positive and negative amplitude maximum. Hence, we get many data points that have exactly the same amplitude. This makes the maxima of the displacement curve appear flatter than they actually are. When the amplitudes become small enough to avoid the steel wire, we see that the data points make up a much smoother curve.

In addition to the wires, there were tiny bumps on the surface of the tube, as depicted in Figure 4.60. These bumps were so smooth that they probably did not affect the flow in any significant way. They are, however, believed to have refracted the ambient light in the room in such a way that small measurement errors occurred. A qualitative error analysis of this is shown in Figure 4.59.

Liquid sticking to the inside of the tube also caused slight problems. This was especially a problem after the first period of oscillation, where the tube above the liquid got a strong green color component. The only way of making the program tell the difference between the liquid sticking to the tube and the actual interface was to be very thorough when tuning the color criteria limits in the algorithm. With the appropriate criteria in place, we see from Figures 4.53-4.57 that this problem was completely overcome.

Despite the difficulties caused by the steel wire embedded in the tube, the program returned results that clearly show the continuous position of the liquid interface. This shows that the interface tracking algorithm works very well and that it would have returned even better results if a completely transparent tube was used in the experiments.

4.6.2 Error Analysis for the Experimental Results

Two sources of measurement errors have been located, and they will now be discussed in more detail.

Measurement Error due to Steel Wire
The largest error in the experimental data is due to the steel wires embedded in the tubes. Because they created areas of invalid points for the program, they left gaps in the figures. The largest gaps that we have in any figure can be seen in Figure 4.57. A close-up of the most prominent gaps is shown in Figure 4.58.

By measuring the width of the gaps in Figure 4.58, we can get an estimate of the vertical distance that was omitted by the program because of invalid search criteria. The measurements were done in Matlab, where the coordinates of a given point can be obtained by clicking on it in the figure. The distance of interest is the width between the two points on each side of the gap. The different widths for each gap were then averaged to obtain the average gap width. The results of this analysis are as follows:

Table 4.2: Average gap distances from the error analysis in Figure 4.58

	Average width (cm)
Gap 1	0.51
Gap 2	0.66
Gap 3	0.50

From Table 4.2 we see that the average gap width is quite similar for the three measurements. The reason for the one in the middle being larger could be that the camera was focused at this point. With a stronger light sensitivity in the focus point, the reflected light from the wire will be slightly stronger. This is further backed up by the fact that the two other gaps, located an equal distance from the mid gap, have almost identical average widths.

The conclusions that have been reached imply that the light reflected from the wire resulted in an area of unreadable pixels. If the gaps were not located at the max or min of the curve, it did not cause any problems for the purposes of present work. However, as we can see in some areas of Figure 4.57, the gaps cut the top of the curve. This will in the worst case leave us with an average error of ± 0.66cm in the amplitude measurements.

Measurement Error due to Ripples in the Tube
The second type of error in the experimental data is only visible for low velocities. This error is slightly smaller than the steel wire error. The last segment of Figure 4.55 was chosen for this analysis. The section of interest is displayed in Figure 4.59. We see that the data points are not perfectly lined up, but rather placed at certain horizontal lines. This looks a bit like the previous issue with the steel wire. However, the distance between the gaps is too small. The max and min points of the curve in Figure 4.59 are in fact both in the same gap between two wires.

In order to qualitatively measure the maximum error in Figure 4.59, the distance from the points farthest away from the mean value lines was measured. These distances are illustrated by green arrows in Figure 4.59. 12 measurements like this were done along the curve depicted in the figure, and the results were then averaged. The resulting maximum error was ± 0.15cm. Note that the standard deviation would be less than this, because there are a lot of points that are close to the mean lines as well. However, for our purposes the average maximum error tells us more about the measurements.

There could be two reasons why the data points are all located in distinct bands. They are both due to the structure of the tube. As it turns out, the tube had ripples on the inside. They were periodic, very smooth, and more frequent than the wires. One explanation is that the water sticks to the inside of the tube when the liquid column is moving downwards and accumulates in the troughs of the ripples. However, this does not explain why we have exactly the same pattern when the column is rising. This is therefore not likely to be the explanation.

The other explanation is based on light refraction. It is suspected that the ripples are refracting the light in such a way that the interface can only be detected at certain intervals horizontal intervals. This is illustrated in Figure 4.60. If the ripples create optical blind spots for the camera, this could be an explanation as to why we have no data points within certain bands. The search algorithm chooses the first valid pixel row as the interface. Hence, the actual location of the interface is skipped, and some row below is chosen instead. This means that we will have many data points at the troughs of the ripples, where the light can go relatively undisturbed through the silicone tube wall.

This refraction happens at high velocities as well. However, the liquid is moving so fast that multiple data points are not likely to occur. Zooming in on the turning points at high velocities, we can in fact see the same tendency of accumulation of data points. The frame rate is constant at 25fps, and this explains why we will have many data points at the same level for low velocities.

Two sources of measurement errors were identified in this discussion. The first was caused by steel wires embedded in the tubing, which reflected the ambient light. Because the interface tracking algorithm searched for certain color patterns, the reflections ruined a range of pixel values surrounding the wire. The second source of error was caused by tiny ripples on the surface of the pipe. They are believed to refract the light in such a way that the interface was only detectable within certain intervals. The largest experimental measurement error was determined to be $\pm 0.66cm$. This error was relatively small, and did not cause significant measurement problems in the present work. However, the observed errors have to be sorted out if the results are to be used to e.g measure the continuous velocity of the liquid.

4.6.3 Discussion of the Experimental Results

The question that immediately comes to mind when discussing the oscillations in the U-tube with an inner diameter change is how the diameter transition affects the damping of the liquid. The closest we get to a direct comparison between the present results and the experimental results from Knoop is to look at Figure 3.2 and Figure 4.53. The experiments presented in these figures have approximately the same initial amplitude and they are both performed using with water.

One interesting thing to note, for instance, is how much the amplitude decays during the first oscillation period. The initial amplitude in the constant diameter U-tube experiment was 50cm. During one period it has decreased to approximately 39cm. This corresponds to a 22% decrease in amplitude. Similarly, we find that the corresponding amplitude decrease in Figure 4.53 is about 51%. The damping of the amplitude in the U-tube with a diameter change is thus approximately 2.5 larger than that in the U-tube with a constant diameter.

Extrapolating the amplitude comparison concept from the previous paragraph, we can look at the velocity dependence of the amplitude decay in Figures 4.53-4.57. As it turns out, the velocity plays a very important role when it comes to the damping of the amplitude in these experiments. The amplitude decay percentages during the first period for the different initial amplitudes are as follows: 51cm: 51%, 45cm: 49%, 35cm: 43%, 23cm: 35% and 11cm: 23%.

We can therefore clearly see that the damping is large for the largest amplitudes, which of course implies the largest velocities. This observation can easily be explained from the theory in Section 2.5.2: In equation (2.97) we see that the loss in the coupling is indeed strongly dependent on the velocity of the liquid. The coupling loss term in the equation of motion is proportional to the square of the mean velocity. The regular wall friction comes in addition to this friction contribution.

As with the oscillations in the U-tube with a constant inner diameter, the oscillation amplitude in the diameter change U-tube was quite quickly reduced to a certain level. By the time the liquid has oscillated for about 50 seconds, the amplitude seems to be at the same level in all the figures, regardless of the initial amplitude. It then took quite a long period of time before the liquid came to rest. None of the figures shows this exact moment, but it was observed that it happened around 120 seconds.

4.7 Computational Results for a U-tube with an Inner Diameter Change

The computational results from the work on the U-tube with an inner diameter change will be displayed and discussed in this section. Hence, we will see how well the diameter change simulations do, compared to the experimental results that were presented and discussed in the previous section. Due to the change in the inner diameter, the computational challenges are greater than with the constant diameter U-tube. Even though we have a good friction relation in equation (2.70) from the earlier work, the friction mechanisms in the coupling are expected to dominate the damping.

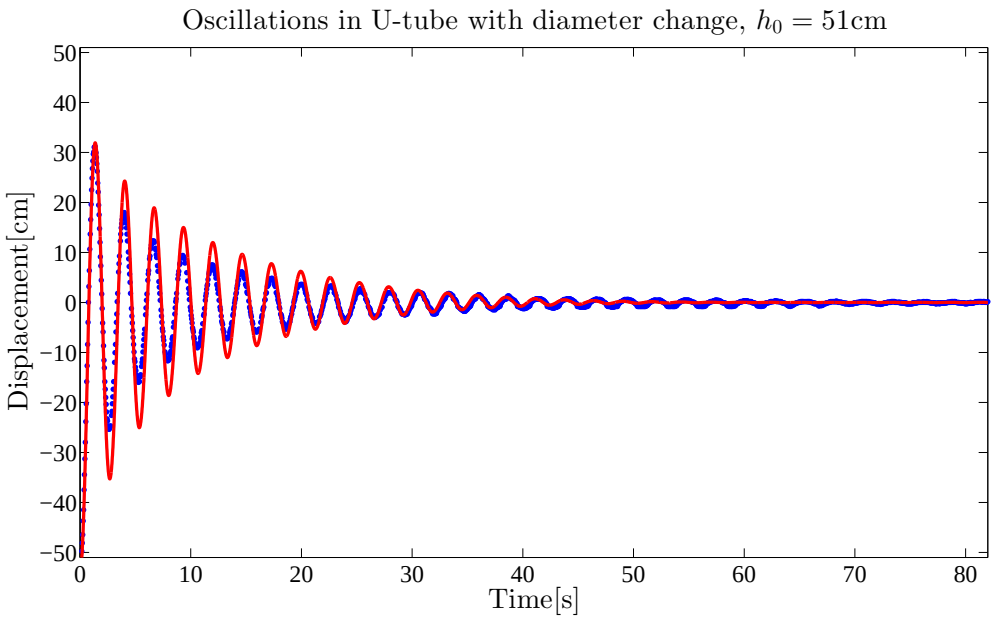

Figure 4.61: The figure shows a simulation of the flow in a U-tube with an inner diameter change, using the error feedback scheme from equations (2.102) and (2.105). The friction coefficient with the laminar correction from equation (2.70) was used to account for the wall friction. The experimental data from the Section 4.6 has been included for comparison. The simulations clearly over-estimate the amplitude of the oscillations during the first 25 seconds. After that, there is good compliance up to 40 seconds, but then the simulations are too quickly damped. It should be noted that the simulations have not come completely to rest after 90 seconds. This happens at about 140 seconds.

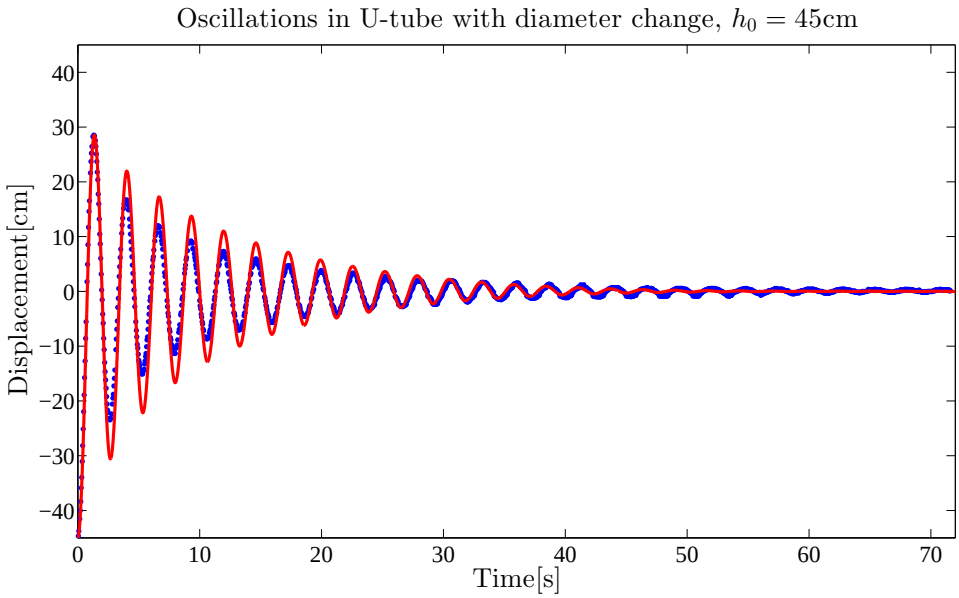

Figure 4.62: The figure shows the same simulation model as in Figure 4.61, only with a smaller initial amplitude. The results are also the same as in Figure 4.61. The amplitude is first over-estimated and then under-estimated, when compared to the experimental data. As with the previous case, the simulations have not come completely to rest after 90 seconds.

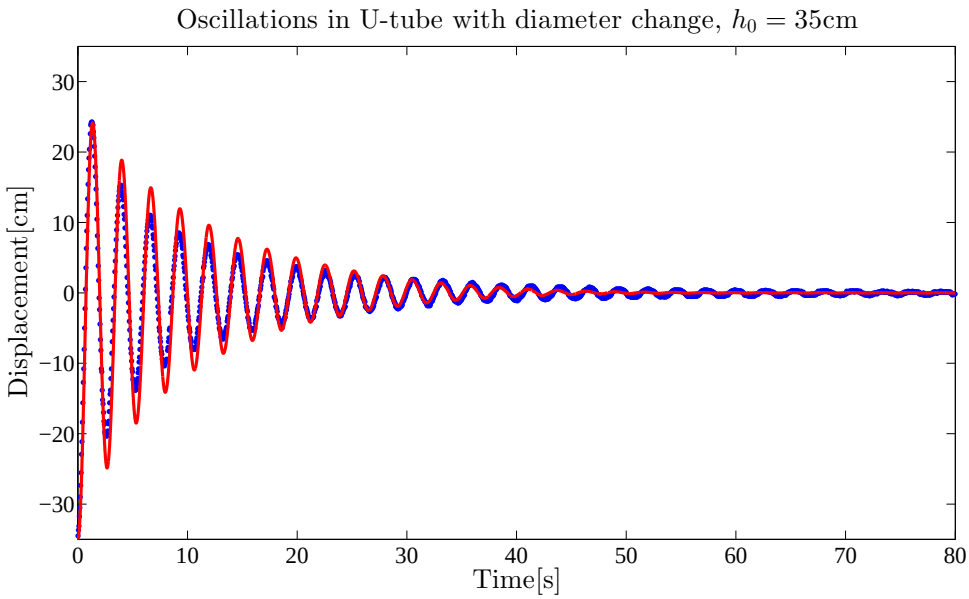

Figure 4.63: The figure shows the same simulation model as in Figure 4.61, only with a smaller initial amplitude. The results are also the same as in Figure 4.61. The amplitude is first over-estimated and then under-estimated, when compared to the experimental data. As with the previous cases, the simulations have not come completely to rest after 90 seconds.

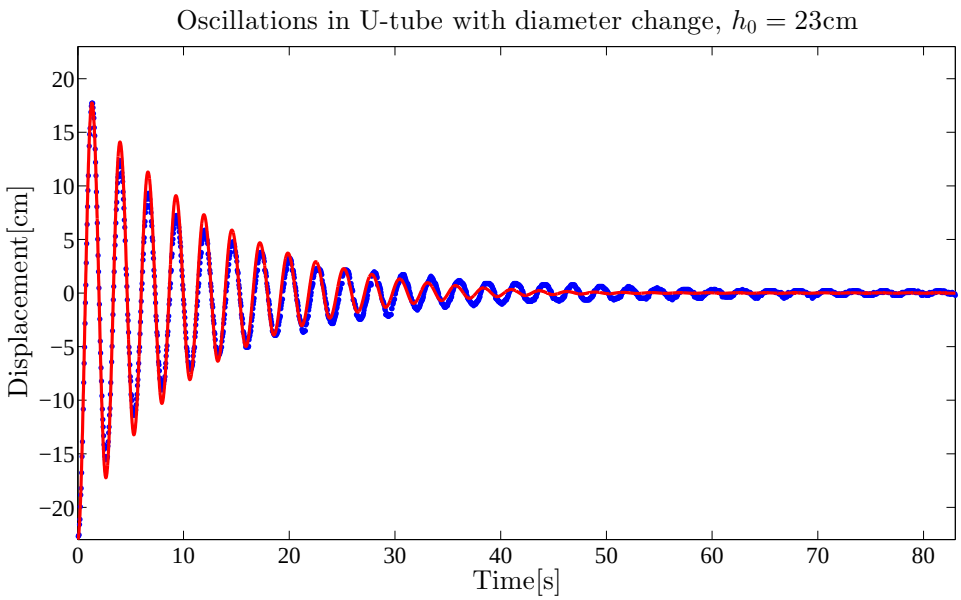

Figure 4.64: The figure shows the same simulation model as in Figure 4.61, only with a smaller initial amplitude. The simulated amplitude is much closer to the experimental amplitude during the first 25 seconds than in the previous figures. However, as with the previous cases, the simulation is too quickly damped. The simulations have not come completely to rest after 90 seconds.

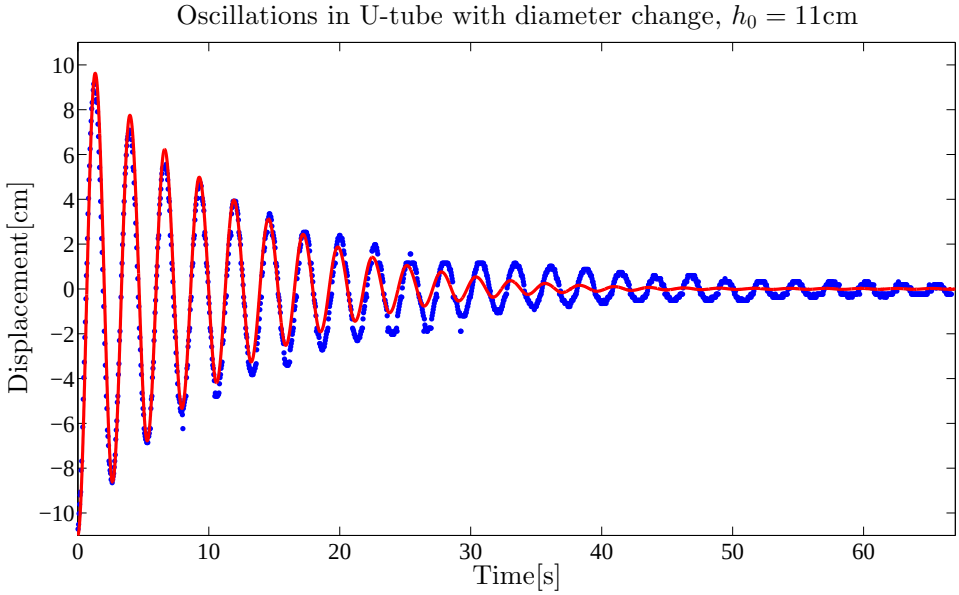

Figure 4.65: The figure shows the same simulation model as in Figure 4.61, only with a smaller initial amplitude. The simulated amplitude is very close to the experimentally observed during the first 15 seconds. However, as with the previous cases, the simulation is too quickly damped. This happens even earlier than with the previous cases. The simulations have not come completely to rest after 90 seconds.

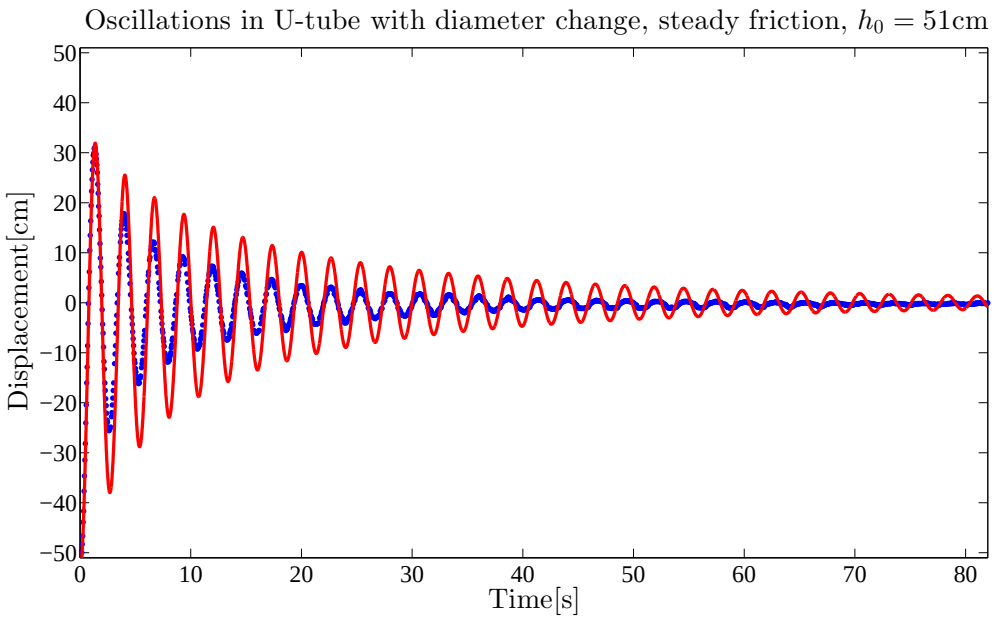

Figure 4.66: The figure shows the same simulation model as in Figure 4.61, only with the acceleration set to zero in the friction relation from equation (2.70). This is thus a comparison of a steady simulation and the same experimental data as in Figure 4.61. The simulated amplitude is over-estimated during the entire time range and shows no signs of coming to rest within reasonable time.

From Figures 4.61 - 4.63, we see that the the simulations clearly over-estimate the amplitude when the velocity is relatively high. There could be several reasons for this, one of them being that the wall friction term from equation (2.70) gives too little damping. Another reason could be that the friction relation for the coupling is not correct. The assumption of an abrupt transition between the two diameters may not be entirely correct.

In Figures 4.64 and 4.65 the results from the simulations are closer to the experimental results during the first part of the time range. This is probably because the flow is more in the laminar regime, so that the friction relation from equation (2.70) gives more damping. This greatly improves the accuracy of the simulations in the beginning. However, it also makes the simulations come even faster to rest.

This is maybe the most apparent problem with all of the simulations of the diameter change U-tube. While the experimental results show that the water column in the U-tube is still slightly oscillating after 80 seconds, the simulations reach very low amplitude around 40 to 50 seconds. The reason for this is probably that a friction relation for an abrupt diameter change was used. This was clearly an assumption that was not entirely valid in this case. A comparison of Figures 4.61 and 4.66 shows that the unsteady correction in the wall shear stress term is essential for making the oscillations come to rest at all.

Hence, we can conclude by saying that the simulation of a U-tube with an inner diameter change is more complicated than that of the constant diameter U-tube. This is due to the turbulent wakes that form at the coupling between the two tubes of different diameters. The simulation results are quite good with respect to amplitude prediction during the first period of time. However, after a while the simulated amplitude will erroneously be heavily reduced. This is probably because it was assumed that the friction loss in the coupling was modeled by an abrupt diameter change relation. The friction relation that was developed in the first part of this thesis definitely improves the results by making the oscillations come to rest.

4.8 Advised Further Research

The simulated results from the concluding friction relation in Section 2.4 are very accurate compared to the available experimental data. However, these data were all obtained from the same experimental setup. The pipe material and the geometry of the rig were not changed during the course of the experiments. Further research should therefore include experiments on a U-tube of e.g. a different size. The new friction model should then be used to simulate liquid oscillations in a U-tube with the new test parameters. This would either expand the validity range or demonstrate weaknesses of the model.

Another option is to do experiments with different liquids than previously used. One of the most recurrent observations in this work was that the variation of liquid density and viscosity caused problems for the friction relations. The new friction relation should therefore be tested for as many liquids as possible.

Further work could also involve implementing the new friction relation from Section 2.4 into a larger flow simulation program. A shut-down case could then be constructed and run, in order to see if there will be significant improvements.

As for the U-tube with an inner diameter change, more experimental and computational research is needed. The simulations conducted in the present work did not show satisfying accordance with experiments. Further work should therefore be focused on finding a better representation of the friction loss in the diameter coupling between the pipes.

Finally, the interface tracking algorithm could be tested in experiments with another pipe material. If the results should prove to be sufficiently accurate, the position measurements could be used to plot the continuous velocity of the liquid. Such data were not possible to obtain in the present experimental work because of the structure of the pipe surface.

5 Conclusion

An unsteady friction relation for oscillating flow in a U-tube was obtained by looking at existing models and applying appropriate modifications. By comparison to previously published experimental data, it was demonstrated that simulations of oscillating flow in a U-tube with a constant inner diameter had a very high accuracy. Most importantly, the new friction relation makes the simulated oscillations come to rest at approximately the right time. The results from the new friction relation have been shown to comply with experimental data from three liquids with different viscosities and densities.

Experiments were conducted on a U-tube with an inner diameter change in the bend. Comparisons to the constant inner diameter U-tube showed that the diameter change caused significantly more damping of the oscillations. This was especially prominent at high velocities.

An interface tracking program was developed in order to continuously track the movement of the liquid interface in the U-tube. The program yielded good results with respect to accuracy and stability. However, the type of tube used in the experiment made it difficult to obtain perfect results.

Computer simulations were also conducted for the U-tube with an inner diameter change. Using the new friction relation from the present work, the amplitude of the oscillations was too quickly reduced. Subsequently, the simulations did not match the experiments as well as with the U-tube with a constant inner diameter. The reason for this was probably that the use of an abrupt diameter change friction relation was not entirely justified.

Bibliography

[1] A. Handal, S. Sangesland,
U-tubing in Mudlift Systems,
NTNU, Trondheim, 2010

[2] A. Bergant, A. R. Simpson, J. Vitkovsky,
Developments in unsteady pipe flow friction modeling,
Journal of Hydraulic Research, 2001

[3] M. O. D. Sellevold,
Demping av U-røyrsvingningar i vasskraftverk,
NTNU, Trondheim, 2013

[4] O. Bratland,
Pipe Flow 1, Single-Phase Flow Assurance,
Unpublished online book at www.drbratland.com, 2009

[5] A. E. Vardy, J. M. B. Brown,
Transient turbulent friction in smooth pipe flows,
Journal of sound and vibration, 2003

[6] B. Brunone, B. W. Karney, M. Mecarelli, M. Ferrante,
Velocity profiles and unsteady pipe friction in transient flow,
Journal of water resources planning and management, 2000

[7] F. M. White,
Fluid Mechanics, sixth edition,
McGraw-Hill, New York, 2008

[8] F. M. White,
Viscous Fluid Flow, third edition,
McGraw-Hill, New York, 2006

[9] D. J. Tritton,
Physical Fluid Dynamics,
Van Nostrand Reinhold, United Kingdom, 1977

[10] H. Schlichting, (translated by J. Kestin),
Boundary-Layer Theory, seventh edition,
McGraw-Hill, New York, 1979

[11] S. Knoop,
Friction in transient multiphase pipe flow,
NTNU, Trondheim, 2004

[12] K. Sudo, M. Sumida, H. Hibara,
Experimental investigation on turbulent flow in a circular-sectioned 90-degree bend,
Experiments in Fluids 25, 1998

[13] R. D. Blevins,
Applied Fluid Dynamics Handbook,
Krieger Publishing Company, Malabar, Florida, 1992

[14] A. Ogawa et al.,
Damped oscillation of liquid column in vertical U-tube for Newtonian and non-Newtonian liquids,
Journal of Thermal Science, 2007

[15] D. A. P. Jaysinghe, M. Letelier, H. J. Leutheusser,
Frequency-dependent Friction in Oscillatory Laminar Pipe Flow,
International Journal of Mechanical Sciences, 1974

[16] H. H. Safwat, J. v.d. Polder,
Friction-frequency dependence for oscillatory flows in circular pipe,
Journal of Hydraulic Research, 1973

[17] H. P. reddy, W. F. Silva-Araya, M. H. Chaudhry,
Estimation of decay coefficients for unsteady friction for instantaneous, acceleration based models,
Journal of hydraulic engineering, 2012

[18] J. P. Vitkovsky, A. Bergant, A. R. Simpson, M. F. Lambert,
Systematic evaluation of one-dimensional unsteady friction models for simple pipelines,
Journal of Hydraulic Research, 2006

[19] W. Zielke,
Frequency-Dependent Friction in Transient Flow,
Journal of basic engineering, 1968

[20] Z. Zarzycki, S. Kudma, K. Urbanowicz,
Improved Method for Simulating Transients of Turbulent Pipe Flow,
Journal of theoretical and applied mechanics, 2011

[21] A. E. Vardy, J. M. B. Brown,
On turbulent, unsteady, smooth-pipe flow,
International Conference on Pressure Surges and Fluid Transients, 1996

[22] A. Adamkowski, M. Lewandowski,
Experimental Examination of Unsteady Friction Models for Transient Pipe Flow Simulation,
Journal of Fluids Engineering, 2006

[23] A. E. Vardy, J. M. B. Brown,
Transient turbulent friction in fully rough pipe flows,
Journal of sound and vibration, 2004

[24] Z. Zarzycki,
Hydraulic Resistance in Unsteady Liquid Flow in Closed Conduits,
Research Reports of Tech. Univ. of Szczecin, 1994

[25] J. W. Daily, W. L. Hankey, R. W. Olive, J. M. Jordaan Jr.,
Resistance coefficients for accelerated and decelerated flows through smooth tubes and orifices,
The American Society of Mechanical Engineers, 1956

[26] B. Brunone, U. M. Golia, M. Greco,
Modeling of Fast Transients by Numerical Methods,
Proc. International Conference on Hydraulic Transients with Water Column Separation, 1991

[27] B. Brunone, U. M. Golia, M. Greco,
Some remarks on the Momentum Equation for Fast Transients,
Proc. International Conference on Hydraulic Transients with Water Column Separation, 1991

[28] T. R. Bewley,
Numerical Renaissance, advance copy,
Renaissance Press, La Jolla, 2012

[29] K. I. M. Flatrker,
Hydrodynamic Oscillations of Non-Newtonian fluids in a U-tube,
University of Stavanger, Stavanger 2013

[30] F. L. Pedrotti S. J., L. M. Pedrotti, L. S. Pedrotti,
Introduction to Optics, Third edition,
Pearson Addison Wesley, Boston, 2007

[31] E. J. Hickin,
River Geomorphology,
Wiley, New York, 1995

6 Appendix

6.1 Turbulent Velocity Profile Integration

The full integration of the logarithmic velocity profile from Section 2.1.6 will now be shown.

By integrating the velocity profile over the cross-section of the pipe, we obtain the average velocity. This average velocity will be dependent on the wall shear stress τ. The shear stress is in turn dependent on the friction factor that we aim to find.

The log law from equation (2.31) can be integrated across the cross-section of the pipe to find the spatially averaged velocity, U^+:

$$U^+ = \frac{1}{\pi R^2} \int_0^R u^+ 2\pi r dr \tag{6.1}$$

Since wall distance y is used as a variable in the log law, it is convenient to change the integration variable from radial distance r to wall distance y. Now we will integrate from the wall towards the center of the pipe. The change of variable implies that r is replaced by $(R - y)$.

We also note that (2.26) is not valid close to the wall, where we should have used equation (2.28). The lower limit of the integral is therefore set to be a very small distance from the wall, θ.

$$
\begin{aligned}
U^+ &= \frac{2}{\pi R^2} \int_{y=R}^{-y=\theta} u^+ 2\pi \left(R - y\right) d\left(-y\right) \\
&= \frac{4}{R^2} \int_{\theta}^{R} u^+ \left(R - y\right) dy
\end{aligned} \tag{6.2}
$$

The center reference point, y_c in equation (2.31) is the same as saying that we are a distance R from the wall. We thus set $y_c = R$ in the following equations. We then insert (2.31) into (6.2) and get:

$$
\begin{aligned}
U^+ &= \frac{4}{R^2} \int_{\theta}^{R} \left[u_c^+ + A \ln \frac{y}{R}\right] (R - y) dy \\
&= \frac{4}{R^2} \int_{\theta}^{R} \left[u_c^+ + A \ln(y) - A \ln(R)\right] (R - y) dy
\end{aligned} \tag{6.3}
$$

To make the integration a little easier on the eye, we split the integral into two parts: One containing the constant and linear terms, the other containing the logarithmic terms. The integral over the constant and linear terms becomes:

$$
\begin{aligned}
I_1 &= \frac{4}{R^2} \int_{\theta}^{R} (u_c^+ - A \ln(R))(R - y) dy \\
&= \frac{4}{R^2} \left[Ry(u_c^+ - A \ln(R)) - \frac{1}{2} y^2 (u_c^+ - A \ln(R)) \right]_{\theta}^{R}
\end{aligned} \tag{6.4}
$$

In order to evaluate the second part of the integral, we need the following integration rules:

$$
\int \ln(y) dy = y \ln(y) - y \tag{6.5}
$$

$$
\int y \ln(y) dy = \frac{1}{2} y^2 \ln(y) - \frac{1}{4} y^2 \tag{6.6}
$$

Applying the rules in equation (6.6) to the rest of the integral from equation (6.3), we get:

$$
I_2 = \frac{4}{R^2} \int_{\theta}^{R} (R - y) A \ln(y) dy \tag{6.7}
$$

$$
= \frac{4}{R^2} \left[RAy(\ln(y) - 1) + Ay^2 (\frac{1}{2} \ln(y) - \frac{1}{4}) \right]_{\theta}^{R} \tag{6.8}
$$

When substituting the lower limit θ for y into equation (6.4) and (6.8), we end up with terms that are proportional to both θ and $\delta y \ln(y)$. We now let $\theta \to 0$. By using the following limit rule,

$$\lim_{\delta y \to 0} \delta y \ln(\delta y) = 0 \tag{6.9}$$

we see that all of the terms containing θ disappear, and we are left with the two integrals evaluated at the upper limit. This yields the final result of the integration:

$$U^+ = \frac{4}{R^2}\left[\frac{1}{4}R^2 u_c^+ - \frac{3}{8}AR^2\right] \tag{6.10}$$

$$\Rightarrow U^+ = u_c^+ - \frac{3}{2}A \tag{6.11}$$

6.2 Concluding Friction Relation Compared to All Available Experimental Data

This appendix contains simulation results from the concluding solution to the work on pipe friction relations. The experimental data to which the simulations are compared are all from the work of Simone Knoop [11]. The results that were displayed in Section 4.5 are excluded from this appendix.

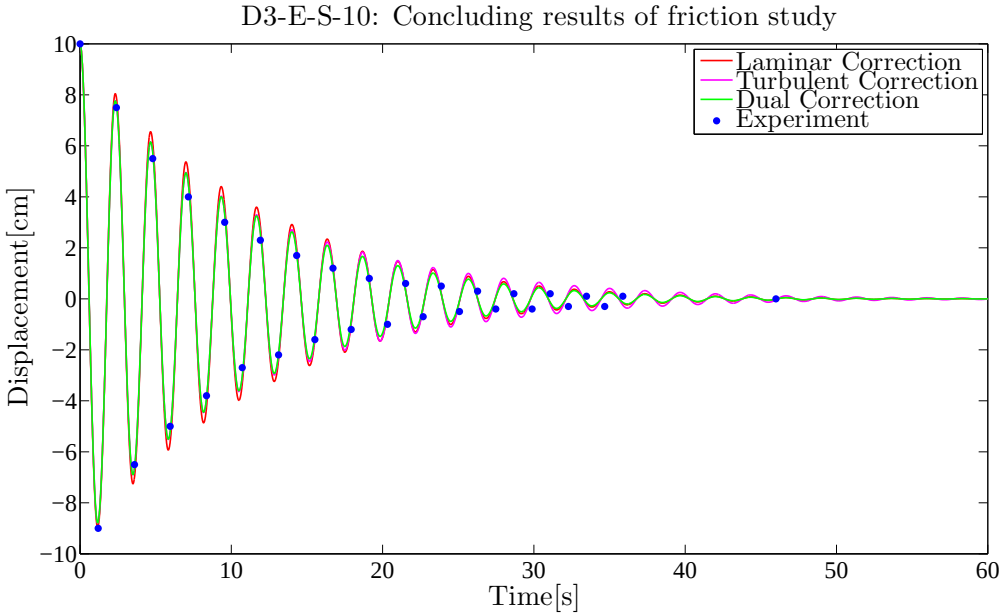

Figure 6.1: The figure shows a comparison of experimental data [11], and the three different versions of the concluding friction relation from Section 2.4.

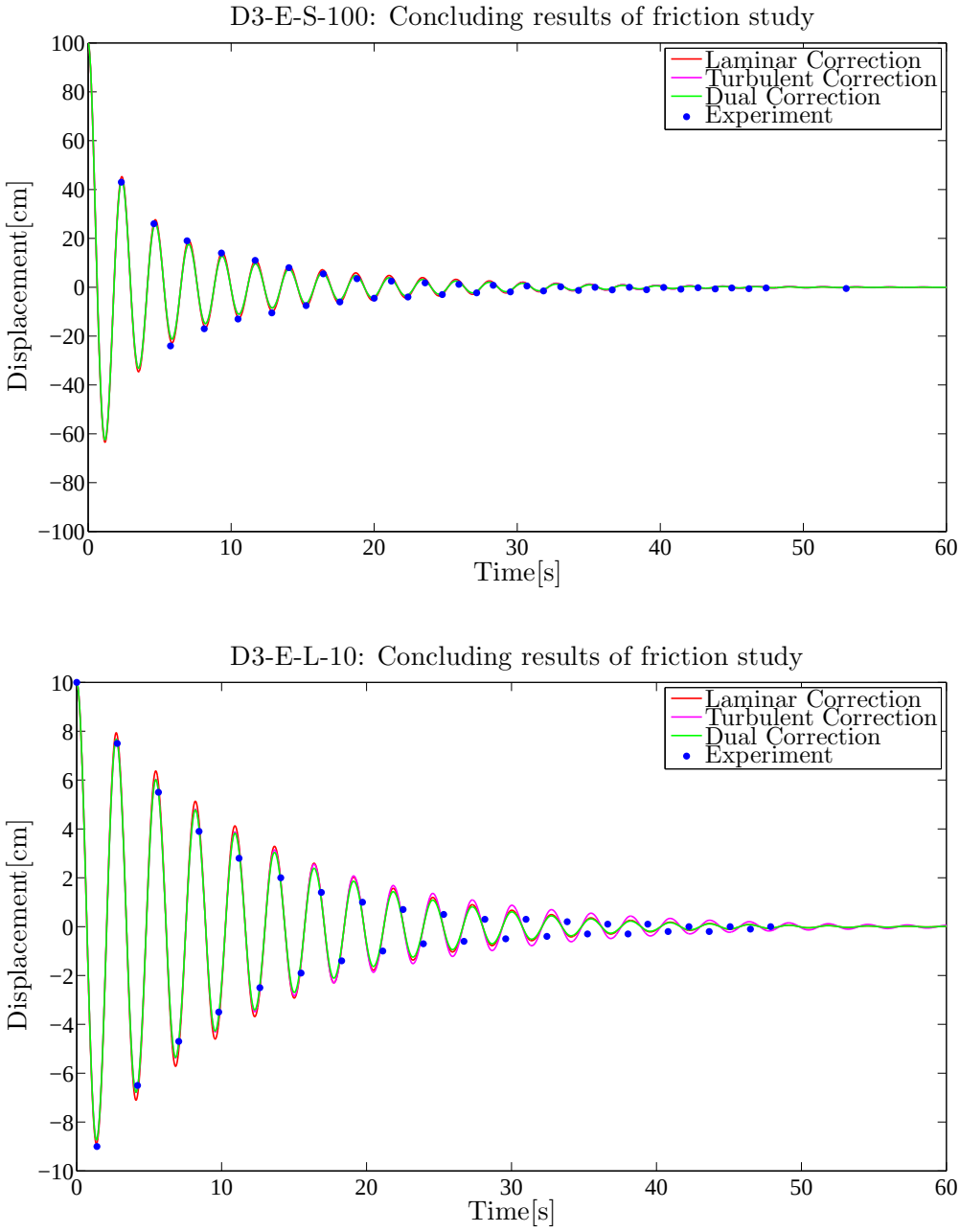

Figure 6.2: The figure shows a comparison of experimental data [11], and the three different versions of the concluding friction relation from Section 2.4.

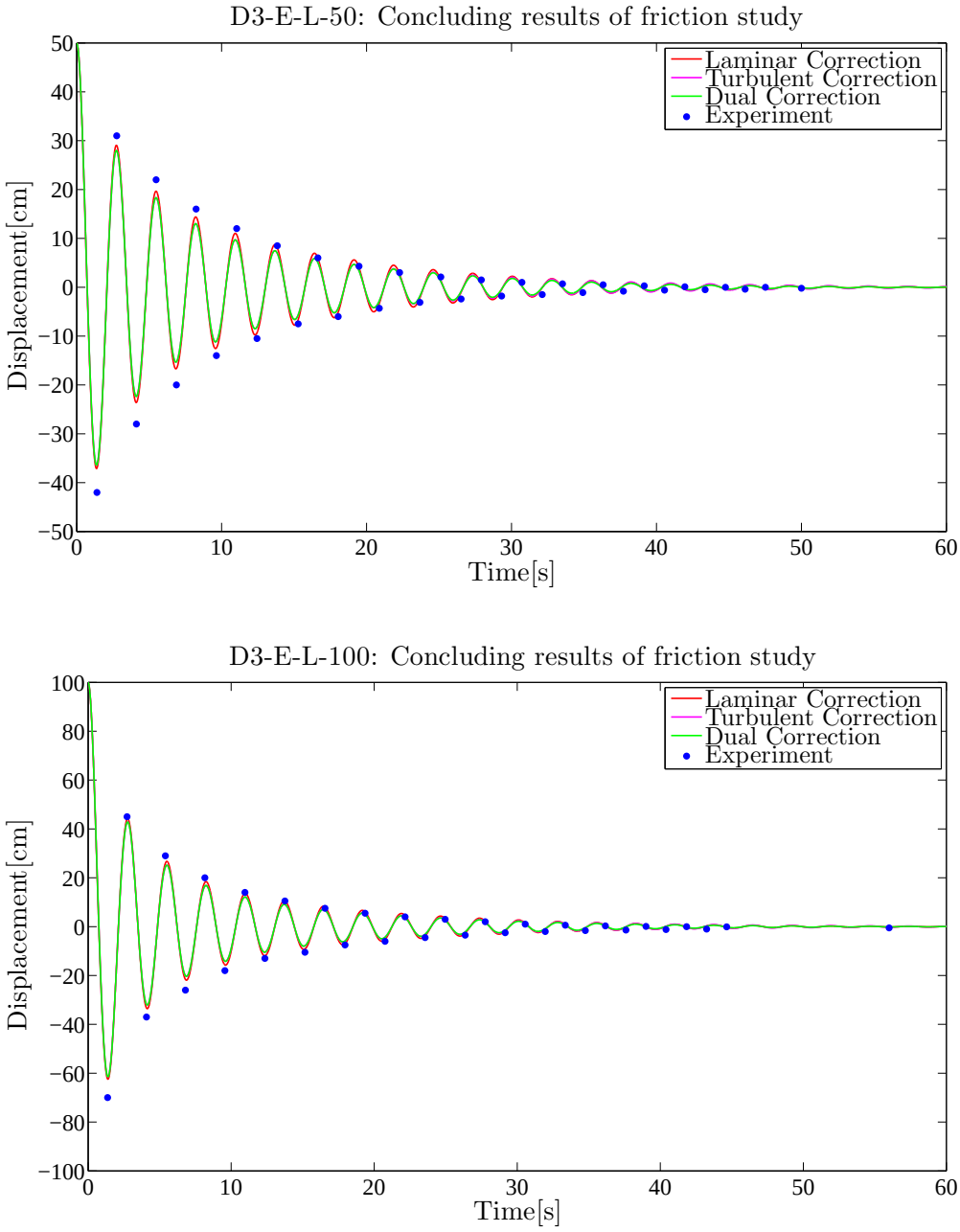

Figure 6.3: The figure shows a comparison of experimental data [11], and the three different versions of the concluding friction relation from Section 2.4.

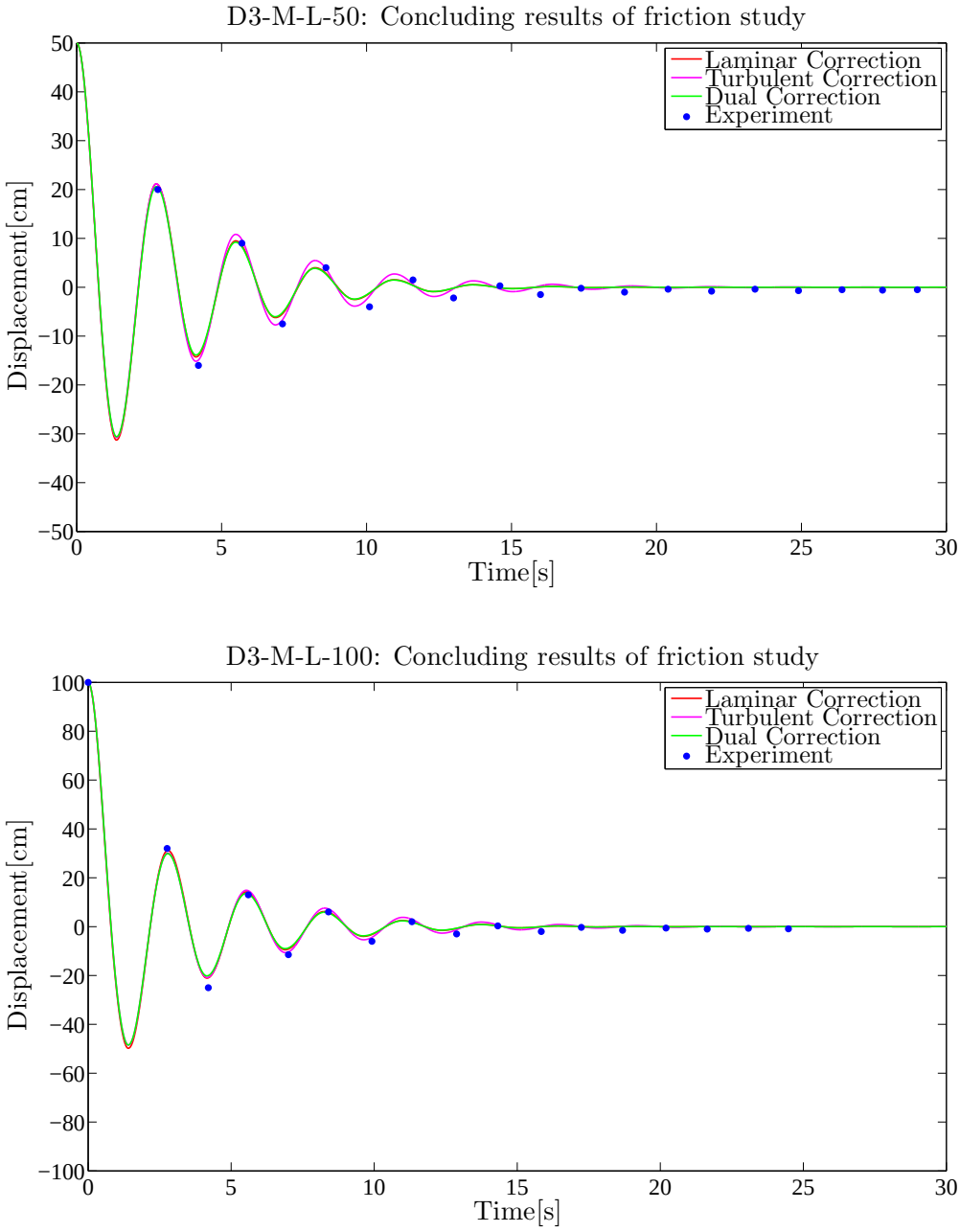

Figure 6.4: The figure shows a comparison of experimental data [11], and the three different versions of the concluding friction relation from Section 2.4.

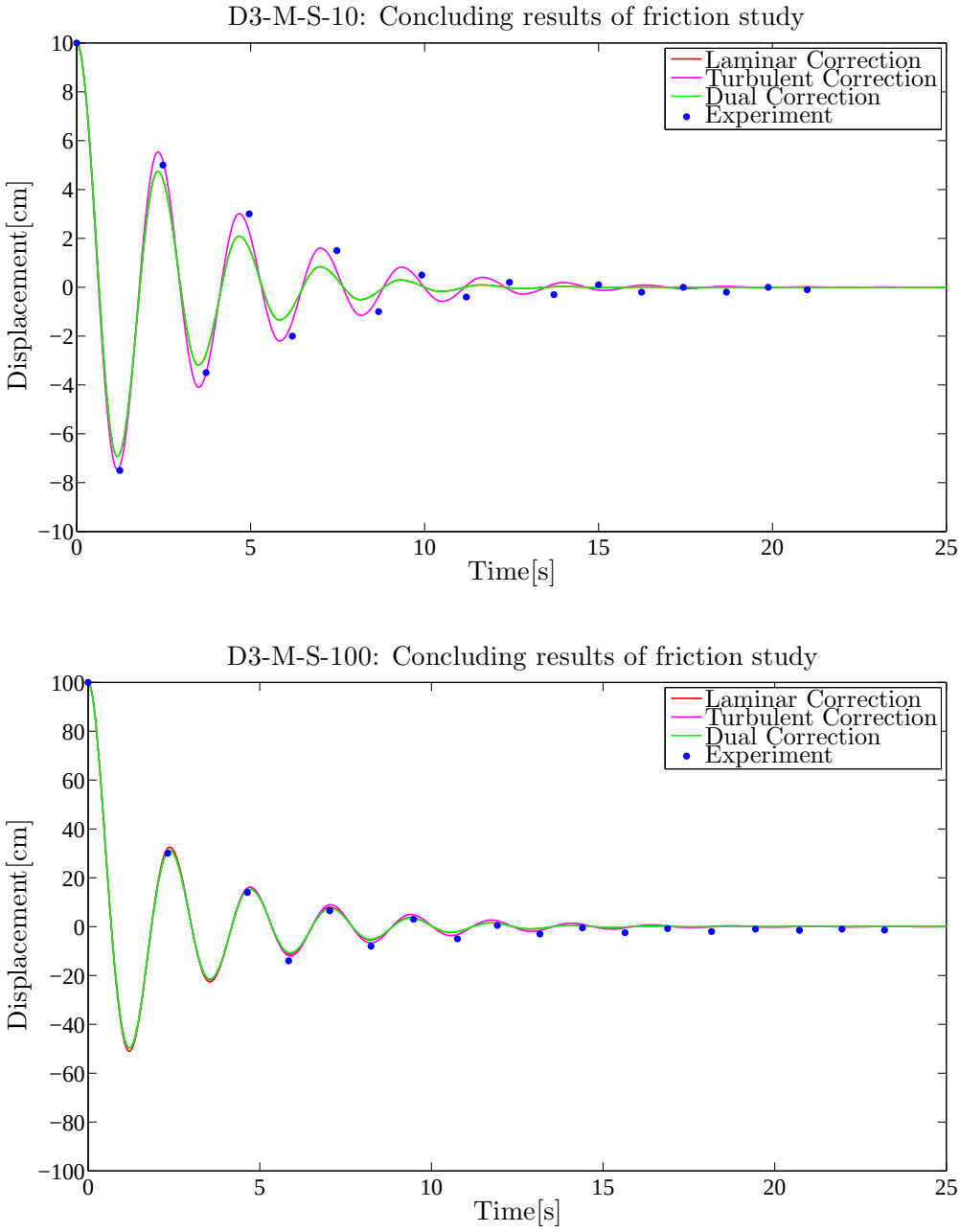

Figure 6.5: The figure shows a comparison of experimental data [11], and the three different versions of the concluding friction relation from Section 2.4.

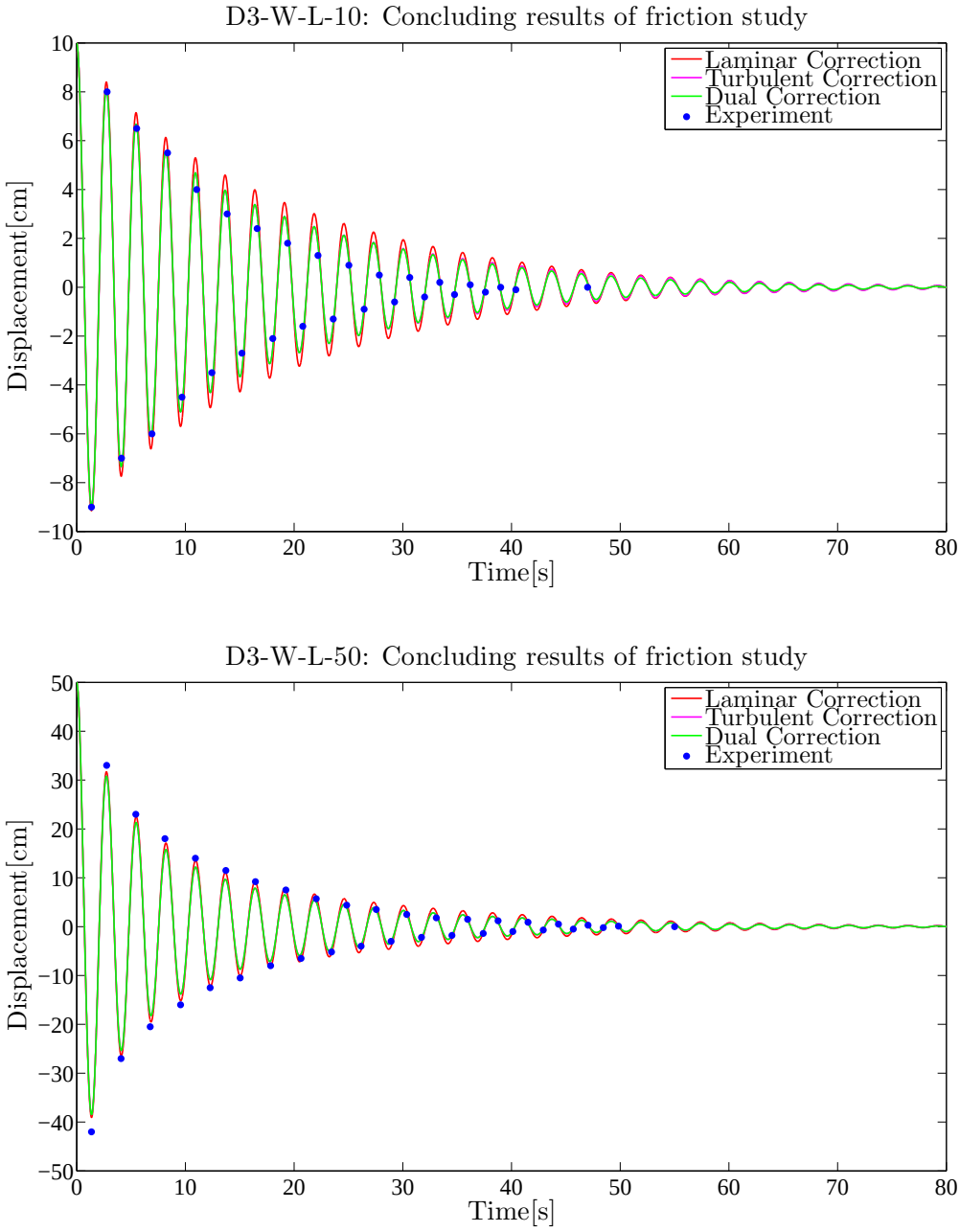

Figure 6.6: The figure shows a comparison of experimental data [11], and the three different versions of the concluding friction relation from Section 2.4.

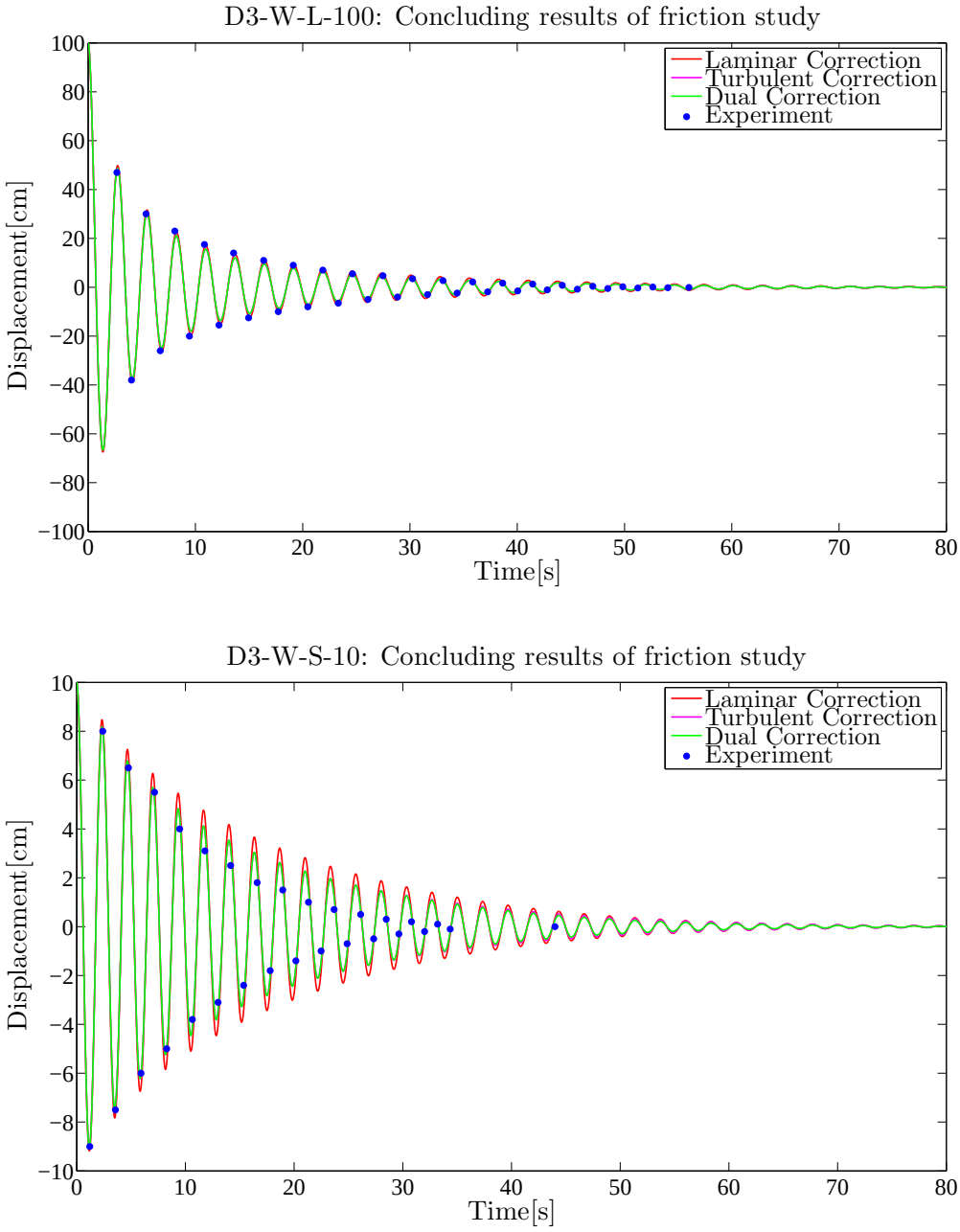

Figure 6.7: The figure shows a comparison of experimental data [11], and the three different versions of the concluding friction relation from Section 2.4.

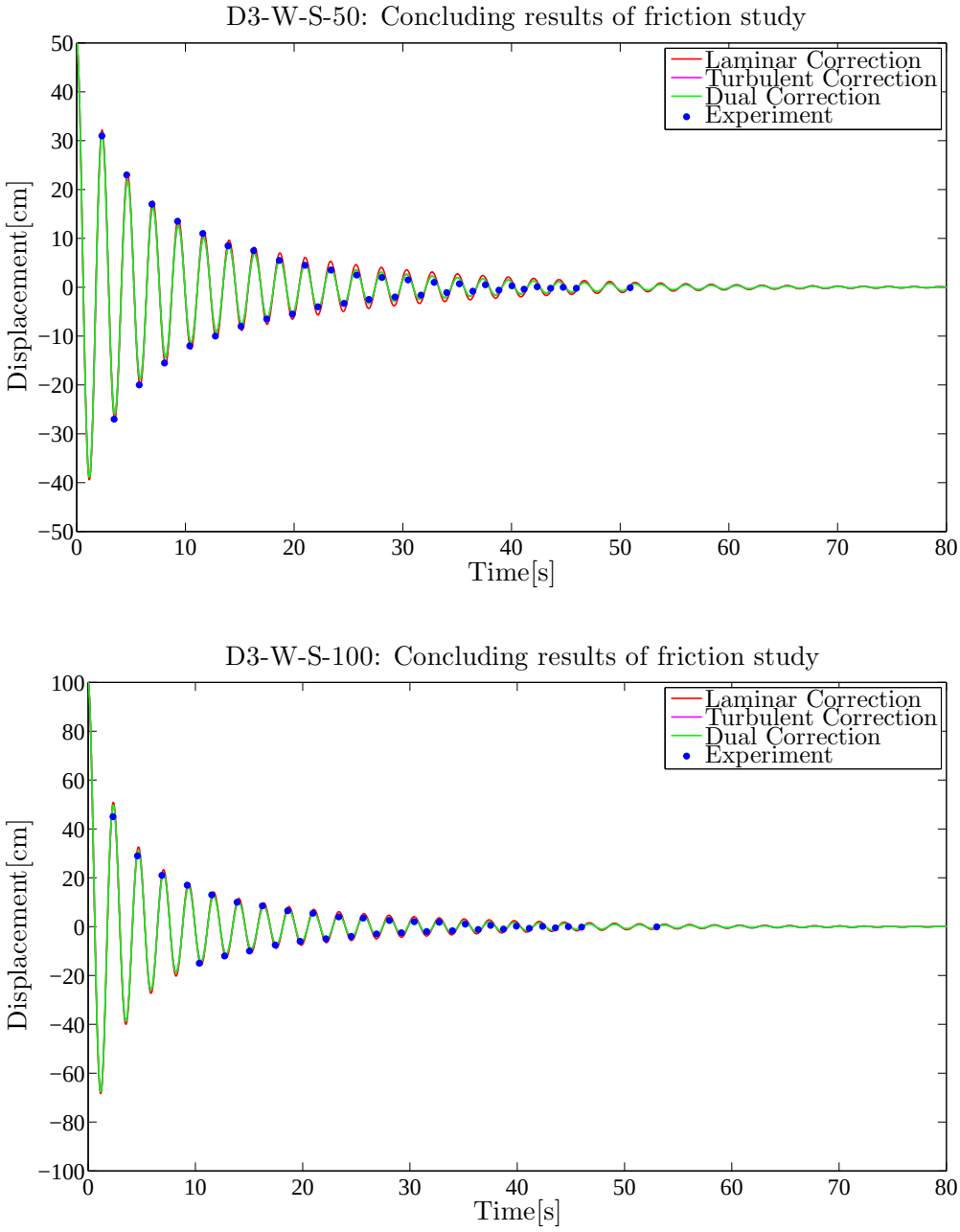

Figure 6.8: The figure shows a comparison of experimental data [11], and the three different versions of the concluding friction relation from Section 2.4.

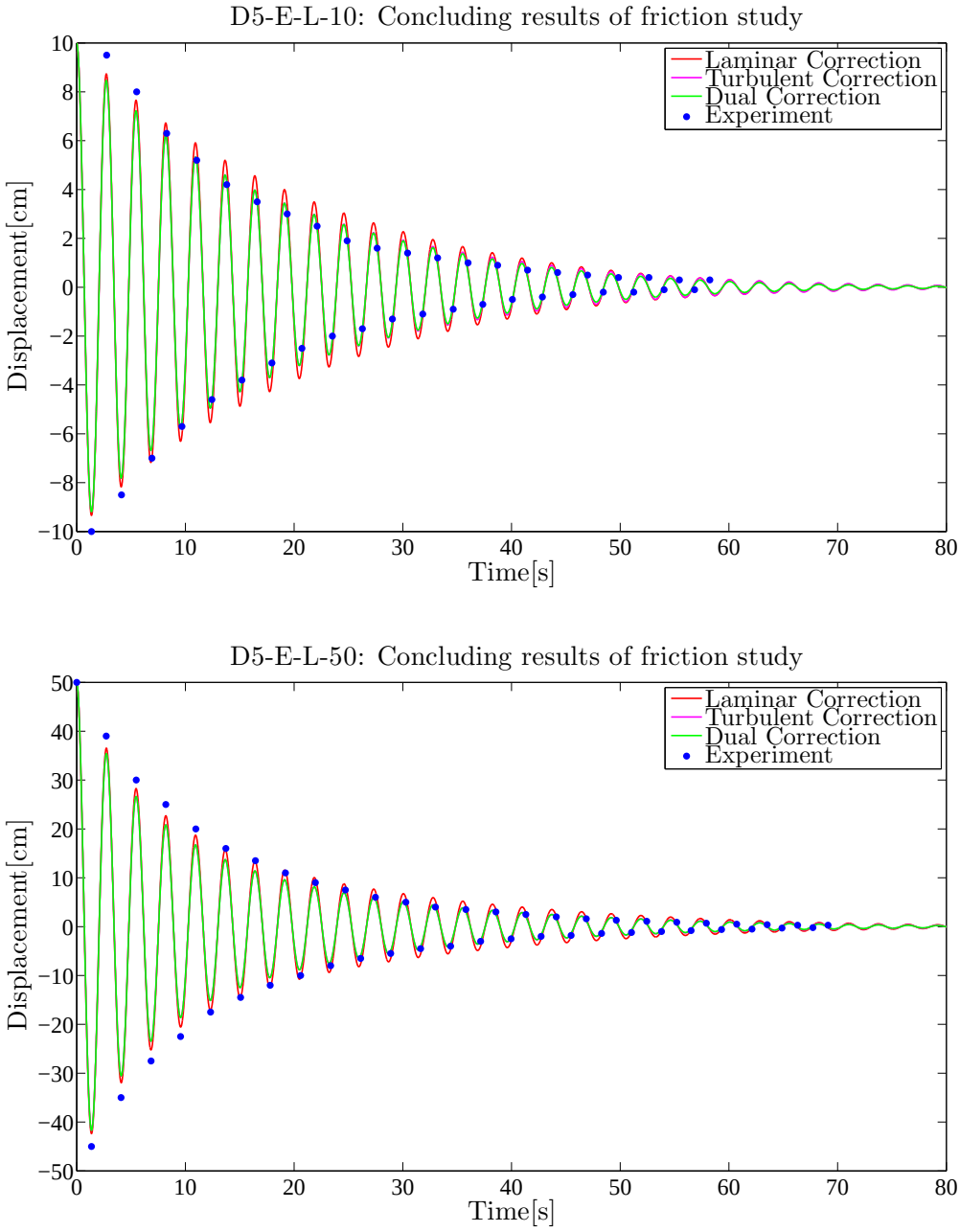

Figure 6.9: The figure shows a comparison of experimental data [11], and the three different versions of the concluding friction relation from Section 2.4.

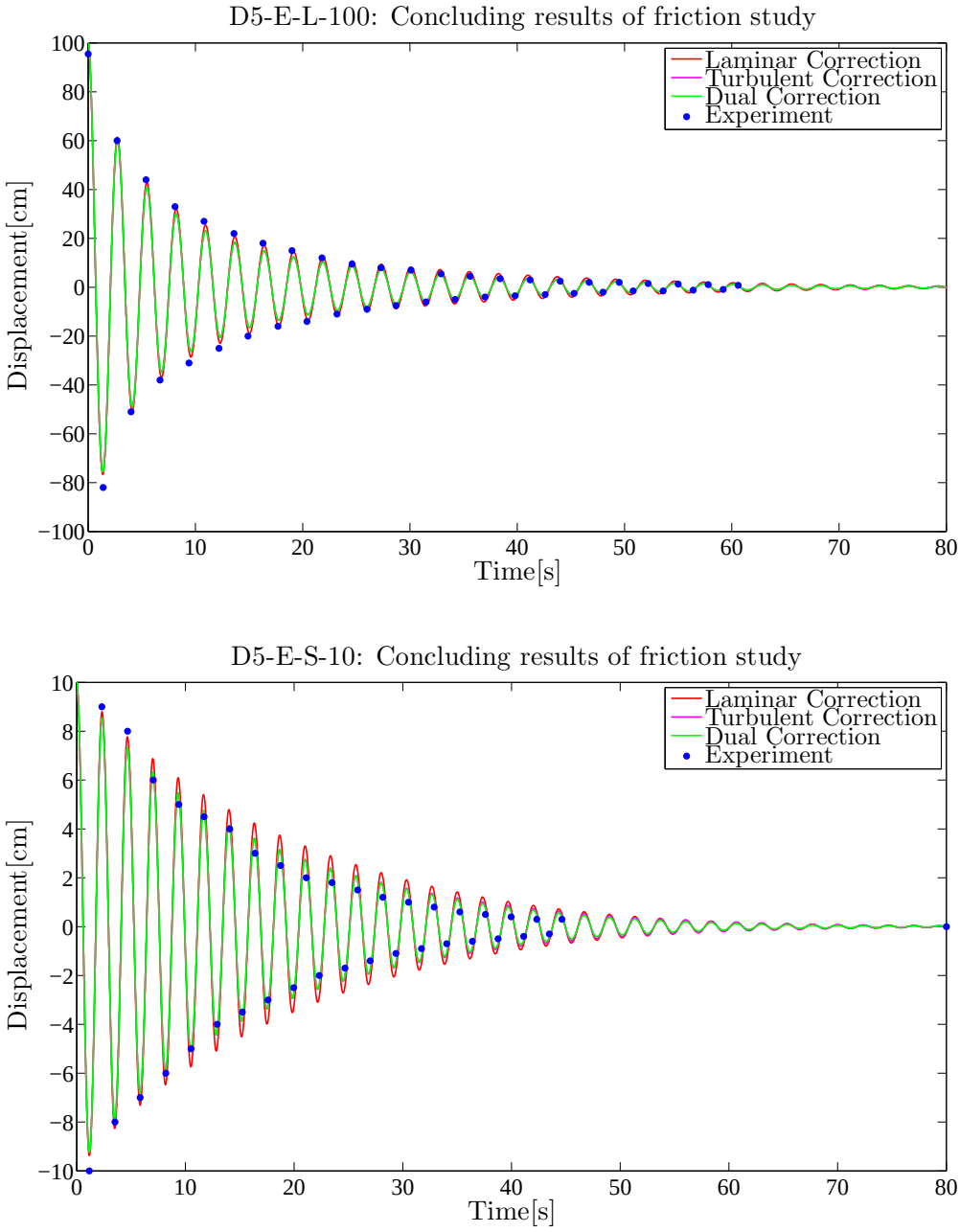

Figure 6.10: The figure shows a comparison of experimental data [11], and the three different versions of the concluding friction relation from Section 2.4.

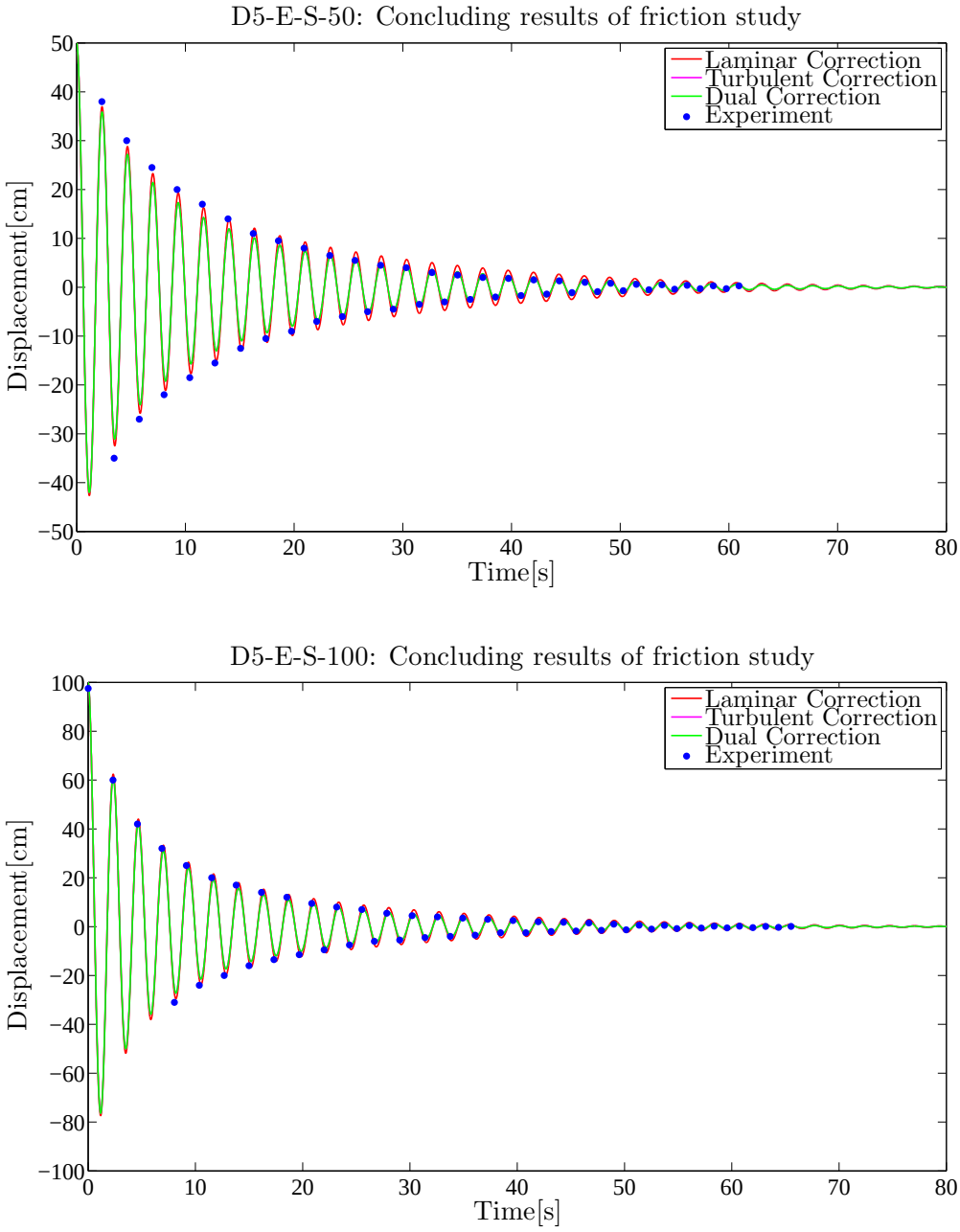

Figure 6.11: The figure shows a comparison of experimental data [11], and the three different versions of the concluding friction relation from Section 2.4.

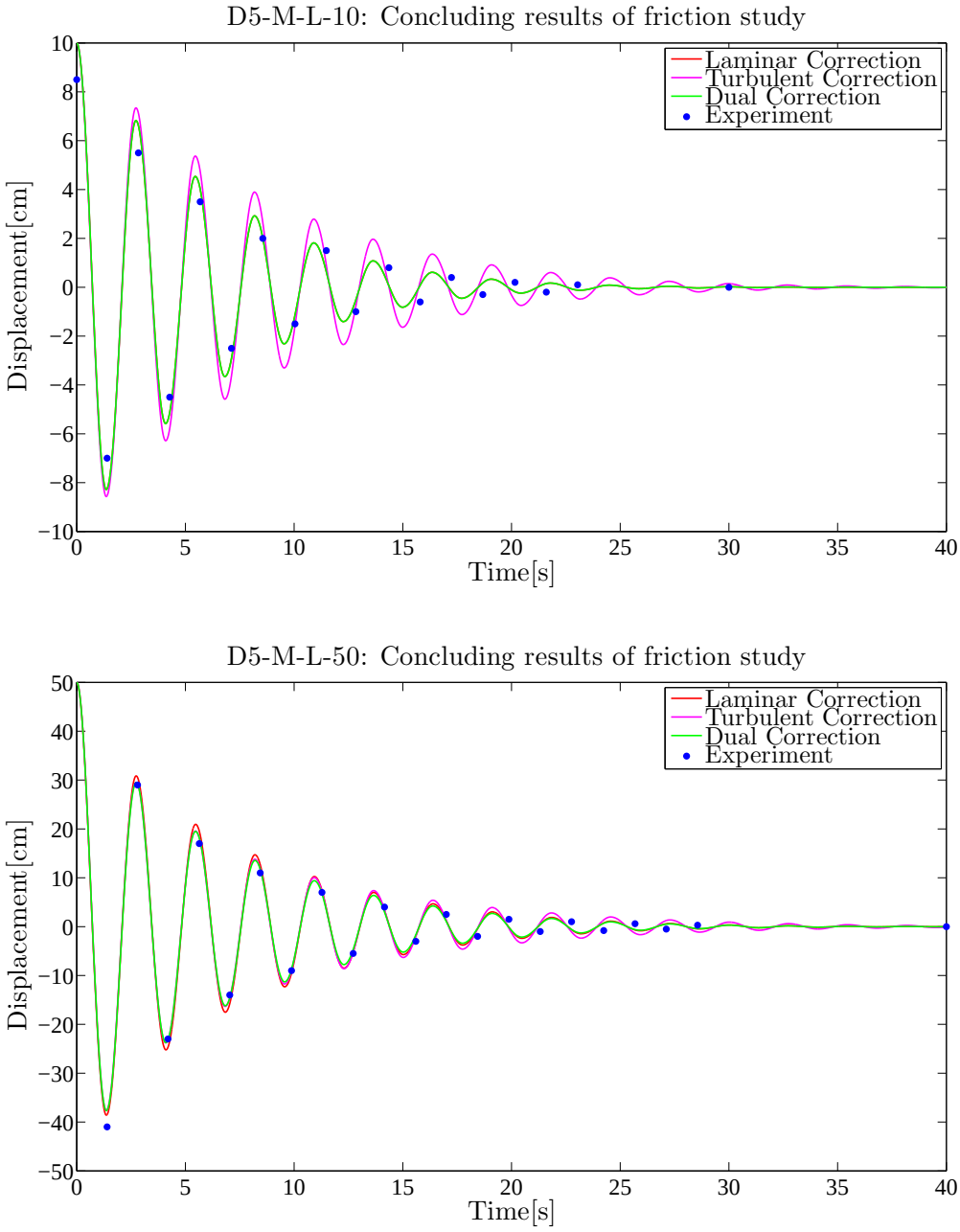

Figure 6.12: The figure shows a comparison of experimental data [11], and the three different versions of the concluding friction relation from Section 2.4.

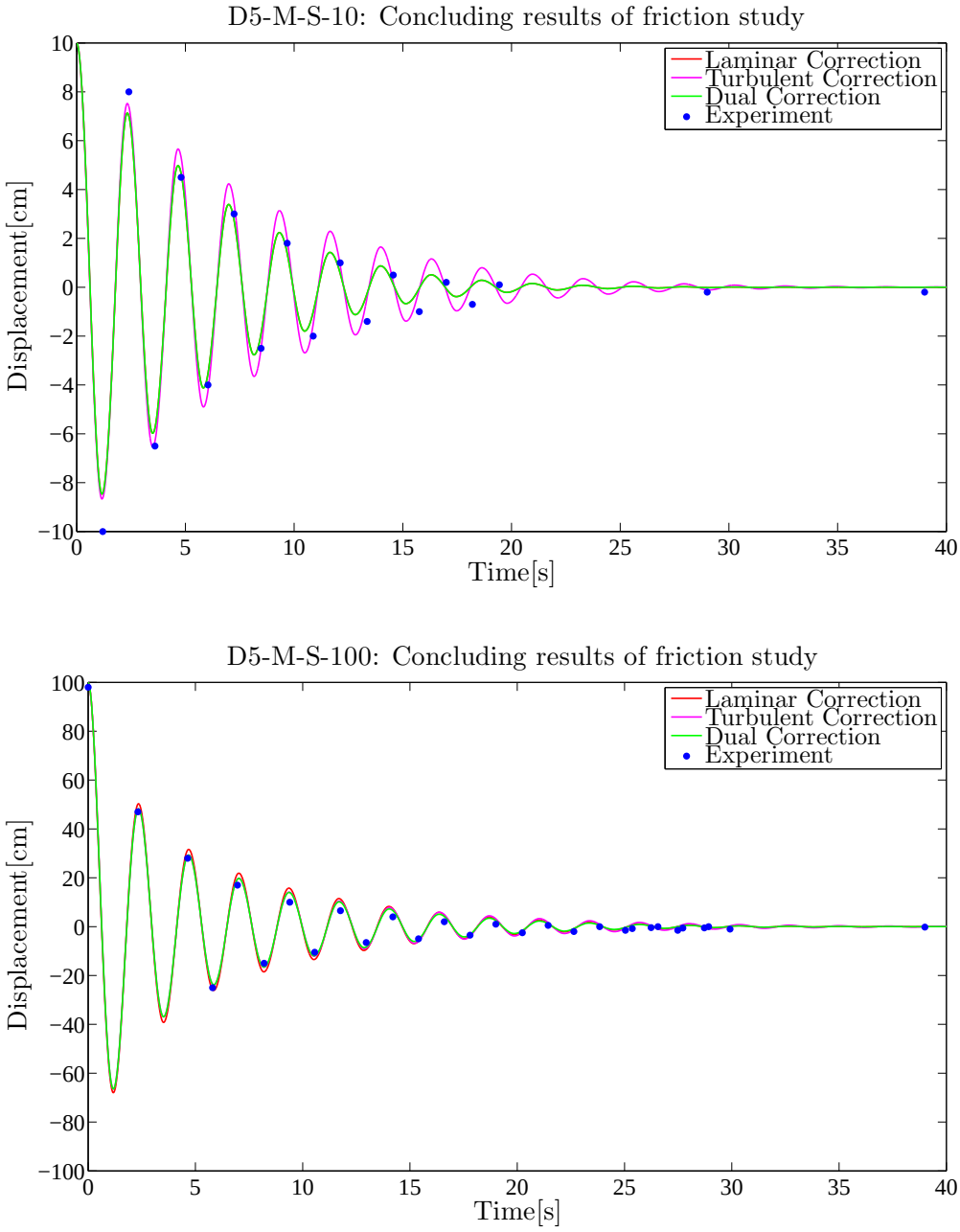

Figure 6.13: The figure shows a comparison of experimental data [11], and the three different versions of the concluding friction relation from Section 2.4.

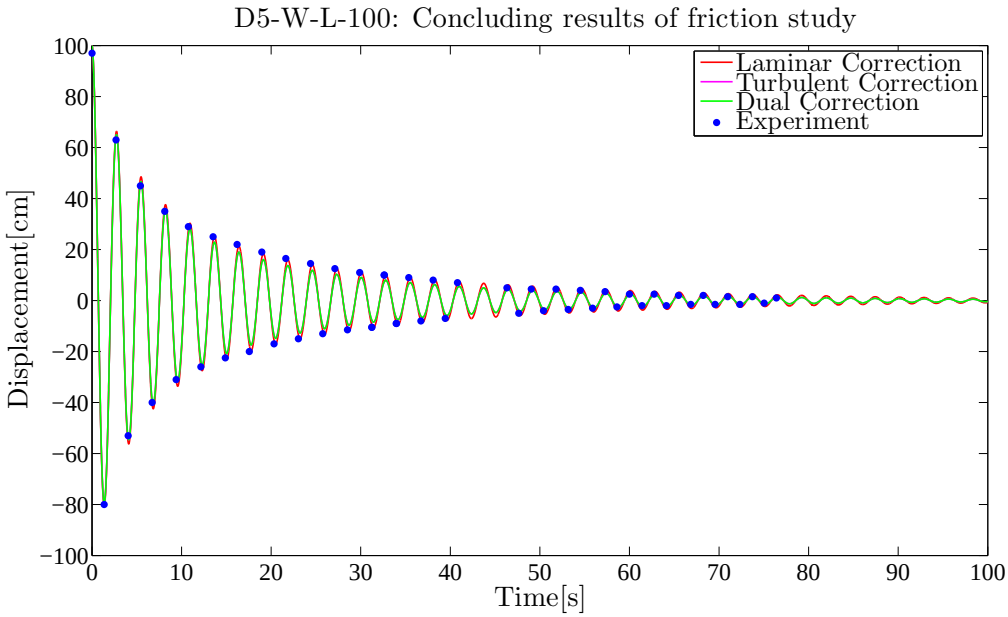

Figure 6.14: The figure shows a comparison of experimental data [11], and the three different versions of the concluding friction relation from Section 2.4.